

## MUTUAL DECOUPLING FOR MASSIVE MIMO ARRAYS

Luo, Shengyuan

*DOI (link to publication from Publisher):*  
[10.54337/aau621653152](https://doi.org/10.54337/aau621653152)

*Publication date:*  
2023

*Document Version*  
Publisher's PDF, also known as Version of record

[Link to publication from Aalborg University](#)

*Citation for published version (APA):*  
Luo, S. (2023). *MUTUAL DECOUPLING FOR MASSIVE MIMO ARRAYS*. Aalborg Universitetsforlag.  
<https://doi.org/10.54337/aau621653152>

### General rights

Copyright and moral rights for the publications made accessible in the public portal are retained by the authors and/or other copyright owners and it is a condition of accessing publications that users recognise and abide by the legal requirements associated with these rights.

- Users may download and print one copy of any publication from the public portal for the purpose of private study or research.
- You may not further distribute the material or use it for any profit-making activity or commercial gain
- You may freely distribute the URL identifying the publication in the public portal -

### Take down policy

If you believe that this document breaches copyright please contact us at [vbn@aub.aau.dk](mailto:vbn@aub.aau.dk) providing details, and we will remove access to the work immediately and investigate your claim.



# **MUTUAL DECOUPLING FOR MASSIVE MIMO ARRAYS**

**BY  
SHENGYUAN LUO**

DISSERTATION SUBMITTED 2023



**AALBORG UNIVERSITY**  
DENMARK





AALBORG UNIVERSITY  
DEPARTMENT OF ELECTRONIC SYSTEMS,  
ANTENNAS, PROPAGATION, AND MILLIMETER-WAVE SYSTEMS  
SECTION

PH.D. THESIS

MUTUAL DECOUPLING FOR MASSIVE MIMO  
ARRAYS

SHENGYUAN LUO

AALBORG, 2023

Dissertation submitted: September 2023

PhD supervisor:: Prof. Gert Frølund Pedersen  
Department of Electronic Systems  
Aalborg University

PhD. Co-supervisor: Assoc. Prof. Shuai Zhang  
Department of Electronic Systems  
Aalborg University

PhD committee: Associate Professor Shahab Heshmati-Alamdari (chair)  
Aalborg University, Denmark

Associate Professor Luyu Zhao  
Xidian University, China

Senior Lecturer Qi Luo  
University of Hertfordshire, United Kingdom

PhD Series: Technical Faculty of IT and Design, Aalborg University

Department: Department of Electronic Systems

ISSN (online): 2446-1628  
ISBN (online): 978-87-7573-638-6

Published by:  
Aalborg University Press  
Kroghstræde 3  
DK – 9220 Aalborg Ø  
Phone: +45 99407140  
aauf@forlag.aau.dk  
forlag.aau.dk

© Copyright: Shengyuan Luo

Printed in Denmark by Stibo Complete, 2023

# Contents

Abstract .....	v
Preface .....	xi
Thesis Details .....	xiii
Part I .....	1
Introductory Chapters .....	1
<b>1. Introduction .....</b>	<b>3</b>
<b>1.1 Motivations .....</b>	<b>3</b>
<b>1.2 Aims of the thesis .....</b>	<b>8</b>
<b>2. General knowledge and discussions .....</b>	<b>10</b>
<b>2.1. Massive MIMO microstrip antenna array .....</b>	<b>10</b>
<b>2.2 Characteristic parameters of the microstrip antenna .....</b>	<b>12</b>
<b>2.3 Mutual coupling between array elements .....</b>	<b>13</b>
<b>2.4 N-element linear array .....</b>	<b>15</b>
<b>3. Contributions .....</b>	<b>16</b>
<b>3.1 Motivation .....</b>	<b>17</b>
<b>3.2.1 Ppaer A .....</b>	<b>18</b>
<b>3.2.2 Paper B .....</b>	<b>19</b>
<b>3.2.3 Paper C .....</b>	<b>19</b>
<b>3.2.4 Paper D .....</b>	<b>20</b>
<b>4. Conclusion .....</b>	<b>21</b>
<b>References .....</b>	<b>23</b>
Part II Papers .....	30
Paper A .....	32
Paper B .....	58

Paper C .....	82
Paper D .....	98

# Abstract

With the development of 5G and 6G, the improvement of the communication quantity and the transmission speed causes a sharp surge in the channel capacity and spectral efficiency. It brings one inevitable issue: the mutual coupling between the massive MIMO array elements can not be neglected when large numbers of array elements are deployed within an integrated system. Especially the mm-wave massive MIMO arrays attract much more attention because of the priority of wide working band, ultra-high transmission speed, and smaller antenna size.

For the massive MIMO arrays, on one hand, mutual couplings exist between the array elements within limited space in horizontal, vertical, and diagonal directions. On the other hand, the low isolation between array elements are composed of surface wave coupling and space wave coupling, where the space wave coupling plays the determined role for the arrays with an inter-elements distance of half wavelength. Three wideband and dual-polarized patch arrays with an inter-element distance of half wavelength are proposed by utilizing the non-resonant metasurface (NRMS), triple-layer metasurface (TMS), and decoupling cavity to reduce the space wave coupling. For the non-resonant metasurface, it can be seen as a media that has negative dielectric constant and positive permittivity along the parallel direction of the NRMS that can be fully employed to suppress the interference among array elements. For the array with TMS, the reflected space waves can be decomposed into two parts, which are canceled perfectly. Where, the first part comes from the bottom surface, while another is reflected from top two-layer surface. The proposed decoupling cavity (DC) is made by engraving a cavity on it. The DC has low insertion loss in the normal and tangential directions of the arrays, respectively. When the DCs are placed on the top surface of the massive MIMO arrays, the propagation of the space wave coupling component along the tangential direction of the arrays can be suppressed effectively.

Furthermore, a Near-field shrinking dielectric superstrate (NFSDS) is proposed for the massive MIMO mm-wave arrays, which can be mounted seamlessly above the mm-wave arrays to shrink the near field of the array elements to reduce the space wave coupling. Finally, a wideband and dual-polarized mm-wave array with increased beamwidth is designed.



# Resume

With the development of 5G and 6G, the improvement of the communication quantity and the transmission speed causes a sharp surge in the channel capacity and spectral efficiency. It brings one inevitable issue: the mutual coupling between the massive MIMO array elements can not be neglected when large numbers of array elements are deployed within an integrated system. Especially the mm-wave massive MIMO arrays attract much more attention because of the priority of wide working band, ultra-high transmission speed, and smaller antenna size.

For the massive MIMO arrays, on one hand, mutual couplings exist between the array elements within limited space in horizontal, vertical, and diagonal directions. On the other hand, the low isolation between array elements are composed of surface wave coupling and space wave coupling, where the space wave coupling plays the determined role for the arrays with an inter-elements distance of half wavelength. Three wideband and dual-polarized patch arrays with an inter-element distance of half wavelength are proposed by utilizing the non-resonant metasurface (NRMS), triple-layer metasurface (TMS), and decoupling cavity to reduce the space wave coupling. For the non-resonant metasurface, it can be seen as a media that has negative dielectric constant and positive permittivity along the parallel direction of the NRMS that can be fully employed to suppress the interference among array elements. For the array with TMS, the reflected space waves can be decomposed into two parts, which are canceled perfectly. Where, the first part comes from the bottom surface, while another is reflected from top two-layer surface. The proposed decoupling cavity (DC) is made by engraving a cavity on it. The DC has low insertion loss in the normal and tangential directions of the arrays, respectively. When the DCs are placed on the top surface of the massive MIMO arrays, the propagation of the space wave coupling component along the tangential direction of the arrays can be suppressed effectively.

Furthermore, a Near-field shrinking dielectric superstrate (NFSDS) is proposed for the massive MIMO mm-wave arrays, which can be mounted seamlessly above the mm-wave arrays to shrink the near field of the array elements to reduce the space wave coupling. Finally, a wideband and dual-polarized mm-wave array with increased beamwidth is designed.





With the development of 5G and 6G, the improvement of the communication quantity and the transmission speed causes a sharp surge in the channel capacity and spectral efficiency. It brings one inevitable issue: the mutual coupling between the massive MIMO array elements can not be neglected when large numbers of array elements are deployed within an integrated system. Especially the mm-wave massive MIMO arrays attract much more attention because of the priority of wide working band, ultra-high transmission speed, and smaller antenna size.

For the massive MIMO arrays, on one hand, mutual couplings exist between the array elements within limited space in horizontal, vertical, and diagonal directions. On the other hand, the low isolation between array elements are composed of surface wave coupling and space wave coupling, where the space wave coupling plays the determined role for the arrays with an inter-elements distance of half wavelength. Three wideband and dual-polarized patch arrays with an inter-element distance of half wavelength are proposed by utilizing the non-resonant metasurface (NRMS), triple-layer metasurface (TMS), and decoupling cavity to reduce the space wave coupling. For the non-resonant metasurface, it can be seen as a media that has negative dielectric constant and positive permittivity along the parallel direction of the NRMS that can be fully employed to suppress the interference among array elements. For the array with TMS, the reflected space waves can be decomposed into two parts, which are canceled perfectly. Where, the first part comes from the bottom surface, while another is reflected from top two-layer surface. The proposed decoupling cavity (DC) is made by engraving a cavity on it. The DC has low insertion loss in the normal and tangential directions of the arrays, respectively. When the DCs are placed on the top surface of the massive MIMO arrays, the propagation of the space wave coupling component along the tangential direction of the arrays can be suppressed effectively.

Furthermore, a Near-field shrinking dielectric superstrate (NFSDS) is proposed for the massive MIMO mm-wave arrays, which can be mounted seamlessly above the mm-wave arrays to shrink the near field of the array elements to reduce the space wave coupling. Finally, a wideband and dual-polarized mm-wave array with increased beamwidth is designed.



# Preface

First, I want to thank China Scholarship Council for funding me to pursue my Ph.D. degree. Then I want to thank my supervisor Prof. Gert Frølund Pedersen and co-supervisor Shuai Zhang, who gave me a chance to study at Aalborg University in Denmark. My deep appreciation goes to my co-supervisor, Associate Prof. Shuai Zhang, who proposed critical and constructive comments and guidelines during my PhD period. Thanks very much to my supervisors.

I am very grateful to Dr. Zhinong Ying from Sony Research Center, Lund, Sweden, for his great assistant during my study abroad. Professor Ying gave me some help with the corporation project, presentation skills, and some guidelines for my career plan.

In addition, I want to thank engineers: Ben Krøyer, Kim Olesen, and Kristian Bank. They helped me buy the components, fabricate the prototype, and measure the antennas.

I want to thank my friends Peng Mei, Yiming Zhang, and Guangwei Yang for their help during my research process and writing the paper. Many thanks are also given to my other friends at Aalborg University in Denmark in entertainment and research.

Most importantly, I am grateful to my wife, Mingyue Wang, who gave me some encouragement during my hard time and shared my happiness after I got some ideal results and my paper was accepted. My family members also gave me a lot of help.

Shengyuan Luo  
Aalborg University, March, 2023



# Thesis Details

Thesis Title: Mutual decoupling for massive MIMO arrays  
Ph.D. Candidate: Shengyuan Luo  
Supervisors: Prof. Gert Frølund Pedersen - Aalborg University  
Assoc. Prof. Shuai Zhang - Aalborg University

This thesis is submitted as part of the requirements for the degree of Doctor of Philosophy (Ph.D.) from Aalborg University, Denmark. The thesis is compiled as a collection of papers, resulting in a short introduction, and the main part of the thesis is scientific papers published in peer-reviewed journals. The work presented in the thesis is the result of three years and six months of research, in the period September 2019 – March 2023, as a Ph.D. fellow in the Section of Antennas, Propagation, and Millimeter-Wave Systems, Department of Electronic Systems, Aalborg University, Denmark.

The Ph.D. stipend (nr. 8-17073) has been funded as a part of the RANGE project.

The main body of this thesis consists of the following papers:

- A. **S. Luo**, Y. Zhang, P. Mei, G. F. Pedersen, and S. Zhang, “Decoupling of Dual-Polarized Antenna Arrays Using Non-Resonant Metasurface,” *Sensors* 2023, 23, 3914. DOI: 10.3390/s23010152.
- B. **S. Luo**, Y. Zhang, G. F. Pedersen, and S. Zhang, “Mutual Decoupling for Massive MIMO Antenna Arrays by Using Triple-Layer Meta-Surface,” *IEEE Open Journal of Antennas and Propagation*, Vol. 3, pp. 1079-1089, 2022.
- C. **S. Luo**, G. F. Pedersen, and S. Zhang, “Massive MIMO Array Design with High Isolation by Using Decoupling Cavity,” *IEEE Trans. on circ. and syst. II: expr. brie.*, Early Access.
- D. **S. Luo**, Y. Zhang, P. Mei, G. F. Pedersen, and S. Zhang, “Isolation Enhancement for Millimeter-Wave Array Antennas Using Near-Field Shrinking Dielectric Superstrate,” *IEEE Open Journal of Antennas and Propagation*, submitted.

According to the Ministerial Order no. 1039 of August 27, 2013, regarding the Ph.D. Degree § 12, article 4, statements from each co-author about the Ph.D. student's contribution to the above-listed papers have been provided to the Ph.D. school for approval prior to the submission of this thesis. These co-author statements have also been presented to the Ph.D. committee and included as a part of their assessment.

In addition to the above-listed papers as the main content of this thesis, the following papers were also authored and co-authored during the Ph.D. studies. Since these papers are not a part of the main body of this thesis, they have not been included in the print. The reader is therefore kindly referred to the respective publishing channels as listed hereafter.

**Conferences:**

1. **S. Luo**, G. F. Pedersen, and S. Zhang, "Mutual Decoupling for Wideband and Dual-polarized Dipole Antenna Array by Using A Compact Decoupling Walls," *16th European Conference on Antennas and Propagation*. (EuCAP 2022), 1-3.

# Part I

## Introductory Chapters





# 1. Introduction

## 1.1 Motivations

In the future, 5G communication systems will serve more family applications besides cellphones and wearable devices, such as smart homes, augmented reality, virtual reality, mobile cloud offices, telemedicine, autonomous traffic driving, smart farm, and automated industry, which are shown in Fig. 1.1 [1] - [5]. These new applications have higher requirements for the communication system. To meet the performance requirements of various new applications in the future for wireless communication systems, numerous 5G technologies have been proposed, such as mobile femtocell [6], spatial modulation [7], full duplex [8], cognitive radio network [9], millimetre wave (mm-wave) [10], massive MIMO [11], etc. Here, the massive MIMO is the key technic of 5G, which can greatly improve spectrum efficiency, transmission reliability, energy efficiency, etc. [12] - [14]. The massive MIMO is also the basis for the application of millimetre-wave communication.

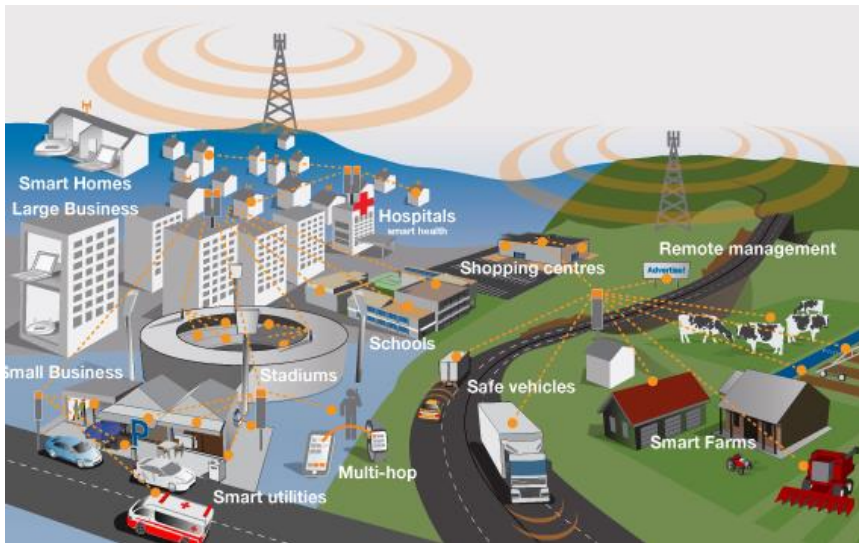


Fig. 1.1. The applications scenarios of millimeter-wave

MIMO (Multiple Input Multiple Output) technologies are referred to as deploying multiple transmission antennas in transmitter and receiver. The signals can be transmitted and accepted independently to improve antenna

gain and reduce interference between different transmission passes. MIMO techniques are utilized to direct the antenna beam to the users. But as we entered the 5G time, the explosive growth users were connected to the 5G network, which caused the 5G further development and enriched the MIMO concept by adding massive antennas in the communication devices. Hence, the concept of massive MIMO came into being. Fig. 1.2 gives a typical  $4 \times 4$  MIMO configuration and a  $64 \times 64$  MIMO configuration.

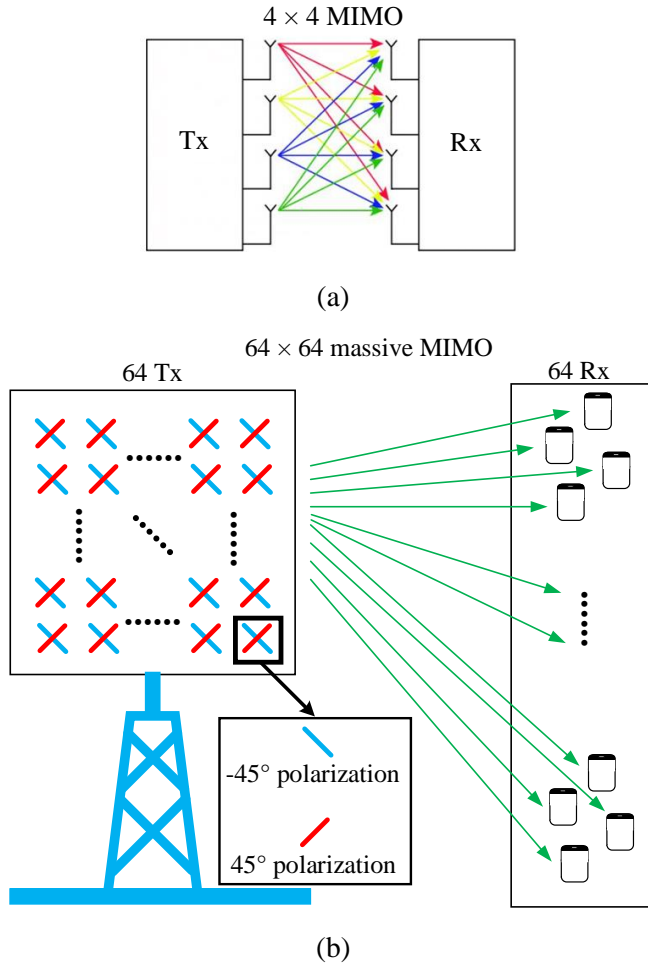


Fig. 1.2. The configurations of  $4 \times 4$  MIMO and  $64 \times 64$  massive MIMO, (a)  $4 \times 4$  MIMO configuration, (b)  $64 \times 64$  massive MIMO configuration.

Compared to MIMO, the massive MIMO typically implements much more than eight antennas in the base station or mobile terminal, which enhances the

transmission rate, capacity, and spectrum utilization of the systems [15] - [19]. Furthermore, the wide band and dual-polarized antenna that has become a trend of current base station antenna research and design. Additionally, At present, there are already many innovative wideband and dual-polarized antennas, including microstrip antenna [20] - [24], patch antennas [25] - [29], electric dipole antennas [30] - [39], magneto-electric dipole antennas [40] - [46], and slot antennas [47] - [51]:

- **Microstrip antenna:** The typical microstrip antenna consists of a metal ground and radiation patch placed on different sides of the substrate. The gap at the edge of the antenna leading the electromagnetic wave leaking so that the electromagnetic wave can be radiated into space. The microstrip antenna has the features of small size, light weight, low profile, easy to conform and integrate, low cost, and suitable for mass production. Adjusting the feeding point can obtain a linear polarized, circular polarized, and dual-polarized microstrip antenna. However, due to the resonant response of the microstrip having a defect of a narrow working band, thence a wideband microstrip antenna can be carried by cascading multiple radiation patches. The strip line, coaxial connector, electromagnetic coupling, and aperture coupling feed methods can feed the microstrip antenna.
- **Patch antenna:** Typical wideband patch antenna has a ground plane and a substrate to support patch. Some slot lines or patterns are etched on the patch to change electric current direction and introduce more closed resonant modes to extend the working band. For the dual-polarized antenna, a bridge structure is typically adopted.
- **Electric dipole antenna:** The electric dipole antenna works with a broader bandwidth than the microstrip antenna and patch antenna. The length of the dipole around half wavelength. The dipole is placed above the ground at a distance of  $\frac{1}{4}\lambda$  to form directional radiation. The cross-polarized antenna has a very low cross-polarization level, making it a promising and widely used candidate in massive MIMO communication systems. To enable it to integrate with mobile devices or other equipment requiring miniaturization, the dipoles of the antenna are bent to decrease its size.
- **Magneto-electric dipole antenna:** The magneto-electric dipole antenna has a pair of electric dipole antennas placed parallel along the ground plane, and a pair of magnetic dipole antennas are vertically

placed and connected with the ground plane and electric dipole. The electric dipole antenna has an “8” shaped radiation pattern in E-plane, while the magnetic dipole antenna has an “o” shaped one in H-plane. When the crossed magnetic dipole antenna and electric dipole antenna are excited with the same amplitude and phase, a “heart” shaped combined radiation pattern will be carried. The magneto-electric dipole antenna features a simple structure, easy broadband, and a wide beam angle, which is very suitable for mobile communication. The ME antennas are normally fed by the cross-arranged “T” shaped feeding probe deployed between the magnetic dipole pair.

- **Slot antenna:** The slot antenna is carried by etching one or more slots on the metal plate, causing electromagnetic wave radiation, where the electric length of the slots determines the radiation patterns and working band. The traditional slot antenna has a narrow band. Therefore, multiple slots can be engraved to generate more closed resonant modes so that the working band of the slot antenna can be broadened. But it is difficult to etch the crossed slot to obtain cross-polarization.

The patch antenna has superiorities of wide bandwidth and low cross-polarized level, yet it is still a challenge to construct complicated slot patterns to form multiple closed resonant modes to broaden the bandwidth. Typically, the feeding structure of the patch antenna passes through the ground plane, which needs a complex fabrication technology. In addition, drilling the holes will destroy the integrity of the ground plane, increasing some difficulty of applying patch antenna for mm-wave applications. Although the electric dipole antenna has a priority of wideband, an air gap exists between the electric dipole antenna and the ground. In addition, the mm-wave antenna performance is very sensitive to the air gap because the mm-wave antenna has a strict requirement on the accuracy of air gap dimensions. Therefore, a small change in the air gap will significantly change the antenna performance. The unique wide beam characteristic of the magneto-electric dipole antenna has attracted much attention from researchers, but a fatal defect of relatively large size and the complex feeding structure makes it difficult to be extended into the mm-wave application. In terms of the slot antenna, it is typically used in the linear-polarized application rather than a dual-polarized massive MIMO antenna array. Based on the analysis of the pros and cons of the referred structure, the microstrip antenna is adopted as the basic element of the wideband and dual-polarized massive MIMO array owing to its features of simple structure, easy to arrange large-scale.

As humans enter into 5G time, the users have exponential growth, inspiring the increment of communication capacity and the transmission rate. Consequently, many antennas are deployed in the communication equipment. At the same time, according to the trend of miniaturisation and compaction, the larger-scale antennas will be integrated with a massive MIMO array that has limited space. Therefore, the physical inter-element distance of the array will be greatly compressed, causing strong electromagnetic interference between array elements, which is called coupling of the massive MIMO array. In the end, the radiation efficiency and channel capacity of the massive MIMO system will be seriously decreased. *Hyok J. Song etc.* presented a comparison between the measured mutual coupling effect on the ergodic channel capacity of a  $2 \times 2$  MIMO system in a reverberation chamber and a suburban outdoor environment [52]. The test results provide insight into the difference in the channel capacity that the mutual coupling between antennas caused a reduction in total embedded radiation efficiency and an increase in correlation, causing a decrease in MIMO capacity. Additionally, the symbol error rate, active voltage standing wave ratio (VSWR), spectral efficiency, bit error rate, adaptive antenna gain, and out-of-band (OOB) emission suppression etc. Furthermore, the beam scanning of the array theoretically has a wide scanning angle base on a hypothesis that the array elements can work independently. But, for the actual application, the mutual coupling between the array elements always exists that can not be neglected. Therefore, if the isolation of the massive MIMO array is enhanced, theoretically, the beam scanning capacity will be enhanced in some certain. *Ai Hu Song* proposed a dual-polarized Ku-band and single-polarized Ka-band shared-aperture phased array in [53]. Some metal strips are loaded above the ground of the Ku-band antenna to eliminate the mutual coupling between the Ka-band antenna and the vertical polarized Ku-polarized antenna. Consequently, the VSWR of the array has been reduced to lower than 3.2 in the beam-scanning coverage in E-plane and H-plane, and the scanning blind spots are eliminated as well, which is helpful to the broadening of the beam scanning. *Md. Afaque Azam* is considered a hybrid architecture for uplink data decoding with the mutual coupling of the base station (BS) [54]. The system performance in terms of spectral efficiency (SE) and bit error rate (BER) is analyzed. The results presented that the system performs better than the one in an actual base station in the absence of the mutual coupling effect. *Q. Yuan, Q* investigated the performance of the adaptive array when the presence of mutual coupling is considered [55]. It presented that mutual coupling degraded the adaptive antenna gain rather than the iterative convergence of the adaptive algorithm. *C. M. Schmid* analyzed

how the mutual coupling and the calibration affect the beam pattern and then proposed a method of worst-case boundaries and statistical analysis of the beam pattern deviation [56].

From the industry viewpoint, when the coupling of the array is reduced to lower than -24 dB, the deterioration of the previously mentioned antenna performance will be significantly alleviated, even though the coupling of the array can not be fully eliminated. Thus, decoupling means should be adopted during the designing process of a massive MIMO array so that the independence of the array elements has a significant increment. Consequently, the beam scanning angle will be increased as well.

## **1.2 Aims of the thesis**

The antenna is a transmit and receive device of wireless communication systems that can transmit and receive magnetoelectric waves. Furthermore, the massive MIMO antenna array is a key part of the massive MIMO systems. This thesis aims to design a massive MIMO array composed of microstrip antennas. To increase the spectral efficiency and system capacity, the array element used in the massive MIMO array must possess wideband and dual-polarization characteristics. During the investigation of the decoupling methods for the massive MIMO array, three  $4 \times 4$  wideband and dual-polarized arrays are used as the reference arrays, which work in the sub 6 GHz band. The decoupling concepts of single-layer non-uniform metasurface, triple-layer metasurface, and decoupling cavity will be studied to reduce the coupling to lower than 24 dB, to satisfy the industry requirement. In terms of the mm-wave massive MIMO base station array, it needs to have a working band of 24.5 GHz to 29.5 GHz, a beam scanning capacity of  $\pm 60^\circ$  in horizontal direction and  $\pm 30^\circ$  in vertical direction, respectively. Meanwhile, the coupling of the massive MIMO mm-wave array has to be reduced to lower than -23 dB.

### **Decoupling for massive MIMO array by using single-layer metasurface**

The wideband and dual-polarization are the basic characteristics of massive MIMO arrays. This thesis adopts the stacked microstrip antennas as the array elements. In addition, the metasurface unit with negative dielectric constant and positive permittivity is a promising candidate to suppress the propagation of space wave coupling. To break out the constraint of the narrow band, caused by the resonant response, a non-resonant metasurface (NRMS) is proposed to broaden the working band with negative permeability.

Theoretically, when a NRMS unit is not sensitive to the incident angles of the space wave coupling, it is a promising candidate for the isolation enhancement of the massive MIMO array, which includes complicated coupling paths.

### **Decoupling for massive MIMO array by using triple-layer metasurface**

Triple-layer metasurface is different from the reflective metasurface or single-negative metasurface. The coupling waves of the array can be divided into two parts, which have different propagation paths. One part comes from the bottom metasurface. Another part is reflected from the top two-layer metasurface. The reflection waves from the bottom metasurface and the top two-layer metasurface have the same amplitude and opposite phase so that these two parts can be cancelled by each other. Furthermore, the metasurface elements work in a non-resonant response band, therefore, it performs stable transmission and reflection characteristics in wideband, which makes it a good candidate for the wideband and dual-polarization array.

### **Massive MIMO array design with high isolation by using decoupling cavity**

All the metasurfaces have a common feature in that the metasurface has to be suspended above the array with a distance, which makes it accrues a puzzle to install and fix it as the simulation model without any tolerance. Therefore, it provides a new train of thought when the decoupling structure is directly mounted above the massive MIMO array without any air gap. When a decoupling cavity with a low insertion transmission in the normal direction and a high insertion loss in the tangential direction of the array is deployed above the array, the tangential part of the space wave coupling can not propagation, while the normal component of the space wave coupling can propagation normally. Here, the high transmission performance of the decoupling structure is caused by the air cavity, while the high insertion characteristic results from the filling medium around the cavity. In the end, the space wave coupling of the array can be suppressed theoretically. Additionally, the broadband response of the low dielectric constant of the decoupling cavity makes it suitable for the isolation enhancement for wideband and dual-polarized arrays.

### **Massive MIMO millimeter-wave array antennas with high isolation**

Considering the pros and cons of the metasurface suspended above the array and the decoupling cavity previously mentioned, it concludes that the seamlessly mounted superstrate is a good method to solve the issue that the metasurface is sensitive to the size change of the air gap between metasurface

and massive MIMO array. When the waves propagate in the superstrate the equivalent wavelength will shorten, and the near field will shrink significantly so that the coupled energy between array elements will weaken when the inter-element distance keeps unchanged. But, when a superstrate with high permittivity is loaded, it will excite strong surface wave coupling theoretically. Thus, the superstrate with proper permittivity can maximize the difference between space wave coupling reduction and the surface wave coupling increment. By directly loading the superstrate with optimized permittivity above the massive MIMO mm-wave array without any air gap makes it an effective and simple method for mm-wave applications.

## 2. General knowledge and discussions

In this chapter, some general knowledge and some discussions are presented to understand the theory and methods in the papers.

### 2.1. Massive MIMO microstrip antenna array

This section introduces the classic configuration and the Characteristic parameters of the massive MIMO microstrip antenna.

Massive MIMO microstrip antenna array is the most important type. Two layers stacked antenna is constructed to generate two closed resonant frequencies to broaden the bandwidth of the antenna. The top antenna is supported by a PP (polypropylene) board with a dielectric constant of 2.2. Two feeding ports are placed in the horizontal and vertical directions to generate dual-polarization electromagnetic waves. On the one hand, when the stacked wideband and dual-polarized antenna has a great impedance matching, the coupling between cross-polarized feeding ports is very high. Therefore, some slots along the diagonal direction are etched to improve the isolation between cross-polarization feeding ports. Here, the inter-element distance is half wavelength. On the other hand, when the positions of feeding ports are adjusted to obtain high isolation between cross-polarization feeding ports, the impedance of the antenna will be not so good, thence an impedance stub is embedded into the substrate of the bottom antenna and connected to the inner conductor of the coaxial feeding cable, which means the substrate of the bottom antenna composed of two-layer substrates so that the impedance stubs can be printed between in. Fig. 2.1 presents a typical  $4 \times 4$  wideband and dual-polarized massive MIMO microstrip antenna array, where the coupling between cross-polarization feeding ports is reduced by etching the cross-



distribute slots. Fig.2.2 presents the picture of the wideband and dual-polarized microstrip antenna with impedance stubs.

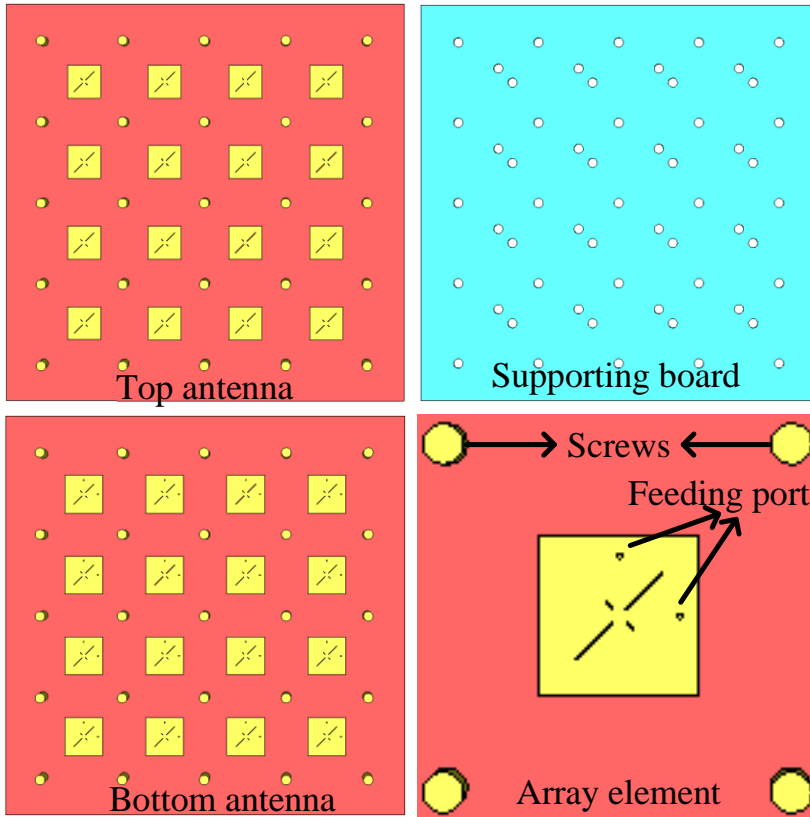


Fig. 2.1. Typical  $4 \times 4$  wideband and dual-polarized massive MIMO microstrip antenna array.

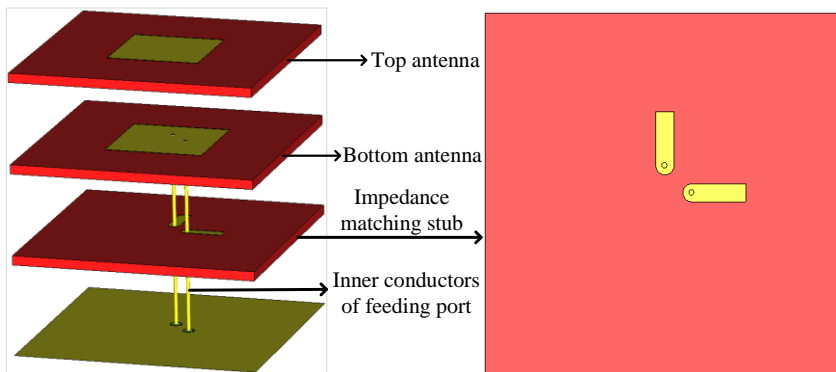


Fig. 2.2. Typical  $4 \times 4$  wideband and dual-polarized massive MIMO microstrip antenna array.

The wideband and dual-polarized antenna with impedance matching stubs shown in previous figurations has a complicated structure and fabrication process. Therefore, it is hard to be applied in mm-wave applications. For the mm-wave massive MIMO microstrip antenna arrays, the differential feed structures are adopted to feed the antenna and reduce the cross-polarization level. This kind of feeding structure can be placed on the backside of the antenna and directly connected to the connectors.

## 2.2 Characteristic parameters of the microstrip antenna

In this section, the characteristic parameters referred to the microstrip antenna are given [57]. Fig.2.3 shows the classical microstrip antenna model. The radiated power from the edge of the patch can be divided into space and surface wave, where the surface wave works in dominant  $TM_{01}$  mode. The surface wave spreads out in the horizontal direction. Therefore, the microstrip antenna coupling can be divided into space and surface wave coupling.



Fig. 2.3. Classical microstrip antenna model.

$$S_{21}^{total} = S_{21}^{space} + S_{21}^{surface} \quad (2.1)$$

Fig.2.4 gives the geometry of the microstrip antenna in cylindrical coordination, where  $r$  represents the distance from the center of antenna to a certain point in the propagation direction of the space wave. The normalized radiation pattern is given by:

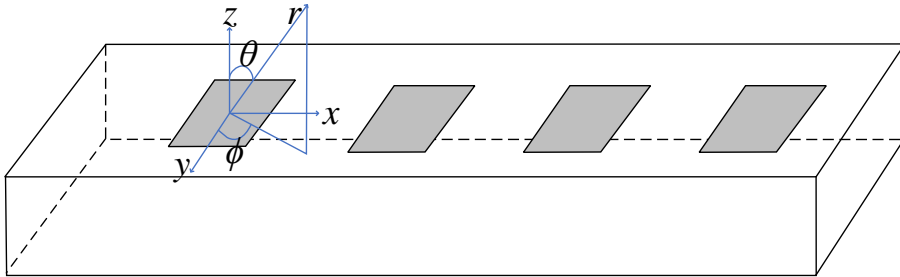


Fig. 2.4. Geometry of the microstrip antenna in cylindrical coordination.

$$E_{\theta} = \frac{\sin\left(\frac{k l \sin\theta \sin\phi}{2}\right)}{\frac{k l \sin\theta \sin\phi}{2}} \cos\left(\frac{k l \sin\theta \cos\phi}{2}\right) \cos\phi \quad (2.2)$$

$$E_{\phi} = \frac{\sin\left(\frac{k l \sin\theta \sin\phi}{2}\right)}{\frac{k l \sin\theta \sin\phi}{2}} \cos\left(\frac{k l \sin\theta \cos\phi}{2}\right) \cos\theta \sin\phi \quad (2.3)$$

Here, the  $k$  denotes the free space wavenumber.

$$k = 2\pi/\lambda \quad (2.4)$$

The radiation pattern function can be calculated by:

$$f(\theta, \phi) = \sqrt{E_{\theta}^2 + E_{\phi}^2} \quad (2.5)$$

$$f(\theta, \phi) = \frac{\sin\left(\frac{k l \sin\theta \sin\phi}{2}\right)}{\frac{k l \sin\theta \sin\phi}{2}} \cos\left(\frac{k l \sin\theta \cos\phi}{2}\right) \sqrt{(\cos\phi)^2 + (\cos\theta \sin\phi)^2} \quad (2.6)$$

## 2.3 Mutual coupling between array elements

As presented in Fig.2.3, the wave is divided into space and surface waves. Consequently, the coupling can also be divided into space wave and surface wave coupling. This section investigates the surface wave and space wave coupling by combining the grounded dielectric slab waveguide model shown in Fig.2.4 [58]. When the surface wave propagates along the +x direction, it has a phase constant of  $\beta_x$ . The surface wave bounces between the dielectric interface and the ground and moves in the x-direction.

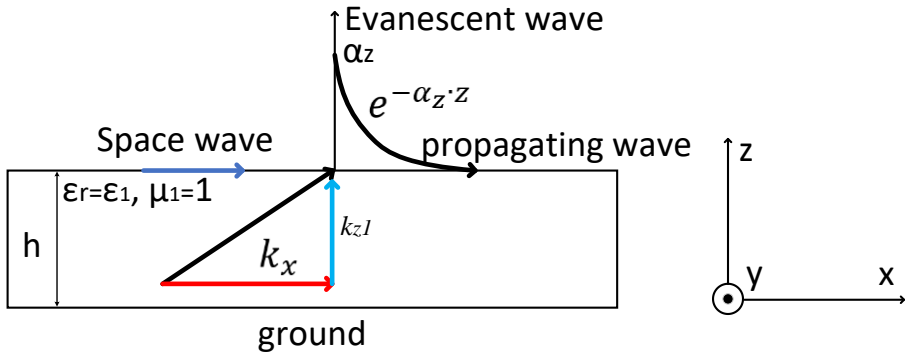


Fig. 2.4. The grounded dielectric slab waveguide model.

$$\alpha_z^2 = k_0^2 - \beta_x^2 \quad (2.7)$$

$$\alpha_z = \sqrt{k_{z0}^2 - \beta_x^2} \quad (2.8)$$

Here, the  $k_0$  denotes the free space wavenumber. The  $\alpha_z$  is the attenuation constant when  $z > h$ .

Equation (2.8) demonstrates that the surface wave exponentially decays when it has a distance from the dielectric interface. When the surface wave propagates in the dielectric slab, it has a phase constant of  $k_{z1}$  and  $k_x$  in  $z$  and  $x$  directions, respectively. Here,  $h \geq z \geq 0$ .

$$k_1 = \sqrt{k_x^2 + k_{z1}^2} = \sqrt{(\epsilon_r - 1)k_0^2} \quad (2.9)$$

$k_1$  is the phase constant in the dielectric slab.

For the surface wave coupling, the coupling impedance  $Z_{21}^{Sur}$  can be calculated according to equation (2.10) [59], [60]:

$$Z_{21}^{Sur} = -\frac{1}{I_{Sur}^2} \iint_S (E_{S1} \times H_{S2} - E_{S2} \times H_{S1}) \cdot \hat{n} dS \quad (2.10)$$

Where the  $S$  presents a closed space with a radius of  $d/2$  and a height of  $h$  with the origin point at the center of antenna. Considering the dominant mode of surface wave is  $TM_{01}$  mode. Thus, the vertical electric field of the excited patch is expressed as following equation (2.11) and (2.12):

$$E_z = -jAk_x^2 \frac{H_1^{(2)}(k_x x)}{\omega \mu_1 \epsilon_0 \epsilon_1} \cos(k_{z1} z), h \geq z \geq 0 \quad (2.11)$$

$$E_z = -jBk_x^2 \frac{H_1^{(2)}(k_x x)}{\omega \mu_2 \epsilon_0 \epsilon_2} \cos(k_{z1} z), z > h \quad (2.12)$$

$\epsilon_0$  is the permittivity of air.

The field component of the surface wave can be calculated as the power flow:

$$P_s = 0.5 P E_{s1} \times H_{s1}^* = I_{Sur}^2 \cdot G_{Sur} \quad (2.13)$$

For the space wave coupling, it also has the dominant  $TM_{01}$  mode. The E-field of the space wave can be written as follows [61]:

$$E_\theta = -j \frac{\exp(-jk_0 r)}{2\lambda r} 8V_0 \exp(j \frac{k_0 l}{2} \cos\phi \sin\theta) \exp(j \frac{k_0 l}{2} \sin\phi \sin\theta) \sin(\frac{k_0 l}{2} \cos\phi \sin\theta) \times \cos(\frac{k_0 l}{2} \sin\phi \sin\theta) k_0 \sin\phi \cos\phi \sin\theta \left( \frac{1}{k_0^2 \cos^2 \phi \sin^2 \theta} - \frac{1}{k_0^2 \sin^2 \phi \sin^2 \theta - \pi^2 / l^2} \right)$$

(2.14)

$$E_{\phi} = -j \frac{\exp(-jk_0 r)}{2\lambda r} 8V_0 \exp(j \frac{k_0 l}{2} \cos\phi \sin\theta) \exp(j \frac{k_0 l}{2} \sin\phi \sin\theta) \sin(\frac{k_0 l}{2} \cos\phi \sin\theta) \times \cos(\frac{k_0 l}{2} \sin\phi \sin\theta) k_0 \sin\theta \cos\theta (\frac{1}{k_0^2 \sin^2 \theta} - \frac{1}{k_0^2 \sin^2 \phi \sin^2 \theta - \pi^2 / l^2})$$

(2.15)

Here,  $d = r \sin\theta$ .

The above equation demonstrates that the propagation distance  $r$  determines the E-field strength. When  $r$  equals the distance between array elements, and  $\theta$  equals  $90^\circ$ , the maximum E-field on the passive patch can be obtained. When  $r$  equals 0, the maximum E-field on the active patch can be got too. When it has a pure superstrate above the antenna substrate, the  $k_0$  is replaced by  $k_2$ .

$$k_2 = (\varepsilon_2 - 1)k_0 \quad (2.16)$$

The coupling denotes that the S21 is the ratio of the maximum magnitude of the E-field on the passive antenna to the active antenna [62].

$$S_{21} = \frac{\max(E\text{-field}) \text{ on passive patch}}{\max(E\text{-field}) \text{ on active patch}} \quad (2.17)$$

Combining the previous analysis, the ratio of surface wave energy to total energy can be calculated as:

$$C = \frac{\varepsilon_1 k_x^3 [2k_{z1} h + \sin(2k_{z1} h)]}{\varepsilon_1 k_x^3 [2k_{z1} h + \sin(2k_{z1} h) + 2k_{z1}^3 \sin^2(k_{z1} h)]} \quad (2.18)$$

The above equation means that the thickness of the substrate determines the surface wave ratio [63], [64].

Therefore, when the array has an inter-element distance of half-wavelength, the space wave coupling is dominant. Consequently, the main work of decoupling is how to reduce the space wave coupling component of massive MIMO arrays. In the works of my thesis, four decoupling methods were proposed and verified. Four corresponding prototypes were fabricated to verify the feasibility of the proposed decoupling method.

## 2.4 N-element linear array

Fig 2.5 gives the geometry of the uniform magnitude and distance N-element linear array. the distance between array elements is  $d$ . When the array elements have the same amplitude but a phase difference of  $\beta$ .

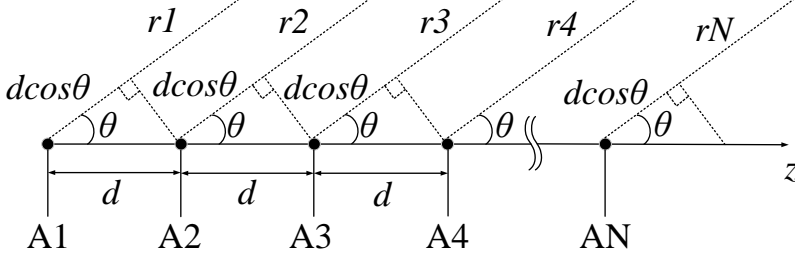


Fig. 2.5. The grounded dielectric slab waveguide model.

The array factor ( $AF$ ) of an N-element linear array is given as follows [64]:

$$AF = \sum_{n=1}^N e^{j(n-1)(kdcos\theta + \beta)} = \sum_{n=1}^N e^{j(n-1)\psi} \quad (2.19)$$

$$\psi = kdcos\theta + \beta \quad (2.20)$$

$$AF = \frac{1 - e^{jN\psi}}{1 - e^{j\psi}} \approx \frac{\sin(\frac{N}{2}\psi)}{\frac{\psi}{2}} \quad (2.21)$$

Normally, we define the beam scanning capacity as the largest angle when the realized gain of the array has a drop of 3 dBi.

### 3. Contributions

This section presents the main contributions of this thesis together with brief summaries of the motivation, content, and conclusions of the papers.

This Ph.D. project involved the following objectives:

1. Dual-polarization and wideband massive MIMO array design by using single-layer non-resonant metasurface.
2. Mutual decoupling for Massive mimo antenna arrays by using triple-layer meta-surface.
3. Isolation enhancement for dual-polarization and wideband massive MIMO array design with decoupling cavity.
4. Decoupling for millimeter-wave array antennas using near-field shrinking dielectric superstrate.

Owing to the dominant coupling type is space wave coupling when the distance between array elements is relatively large. Therefore, the contributions of my thesis concentrate on developing decoupling methods for dual-polarization and wideband massive MIMO arrays. The main contributions of this thesis can be listed below:

1. A decoupling method of non-resonant metasurface (NRMS) is realized by etching square air cavities on the metasurface. The NRMS has a stable negative dielectric constant and positive permittivity along the parallel direction of the NRMS so that the coupling of the massive MIMO array can be reduced. (Paper A)
2. By using a triple-layer metasurface (TMS), the space wave coupling can be divided into two parts, which have the same amplitude and opposite phase, thereby the two kinds of space wave couplings can be cancelled with each other. Thus, the coupling of massive MIMO arrays can be reduced effectively. (Paper B)
3. The decoupling cavities (DC) have low insertion loss in the vertical direction and a high insertion loss in the horizontal direction of the arrays, respectively. When the DCs are seamlessly placed above the massive MIMO array, the propagation of the space wave component in the horizontal direction is suppressed, which causes the coupling of the array can be reduced. (Paper C)
4. A decoupling concept of near-field shrinking dielectric superstrate (NFSDS) is developed for wideband and dual-polarized massive MIMO mm-wave arrays. By loading the NFSDS the near-field of the array elements can be shrunk, and the coupling of the mm-wave array can be reduced. (Paper D)

### **3.1 Motivation**

The massive MIMO array is a key device in the 5G and future 6G applications. But distance between array elements is limited because of the space size constraint, therefore, the coupling of the massive MIMO array is inevitable. Here, the coupling of the array will bring some negative effect on antenna performance in certain, such as power amplifier efficiency, active VSWR, channel capacity, radiation efficiency, impedance match, signal-to-noise ratio, and so on. To increase the throughput and transmission cavity, the features of wideband and dual-polarization for massive MIMO arrays are needed. Correspondingly, the coupling of the massive MIMO array has to be suppressed.

For the massive MIMO array, the mutual couplings between array elements exist not only in orthogonal directions but also in diagonal directions. Furthermore, the mutual coupling between adjacent and non-adjacent elements has to be considered at the same time, because the coupling between non-adjacent elements has a relatively high value, which can not be neglected. According to this requirement, four decoupling methods are proposed in my thesis.

### 3.2.1 Paper A

#### **Decoupling of Dual-Polarized Antenna Arrays Using Non-Resonant Metasurface**

Shengyuan Luo, Peng Mei, Yiming Zhang, Gert Frølund Pedersen, and Shuai Zhang

Published at the *Sensors*, DOI: 10.3390/s23010152

#### **Paper content**

By etching the square air cavities on the metasurface a non-resonant metasurface (NRMS) is carried out, that performs negative dielectric constant in and positive permittivity in the parallel direction to suppress the propagation of the space wave coupling component in tangential direction. To analyze the decoupling principle of the NRMS, the NRMS unit is investigated when the incidence waves propagate along the normal and tangential directions under TE mode and TM mode at different incident angles of  $\theta$  offset the normal direction, and a dual-element array model is utilized to illustrates the development for the NRMS. To verify the proposed decoupling concept, an actual example of a  $4 \times 4$  array with NRMS is simulated, fabricated, and measured.

#### **Main results**

According to the simulation of NRMS unit cell, when the incident wave propagates in the normal direction, the NRMS unit cell performs a high transmission characteristic, and the extracted permittivity and permeability are positive. However, when the incident wave spreads in the tangential direction, the NRMS unit cell has a negative permeability and positive permittivity. When the NRMS is placed on the front of a  $4 \times 4$  array, the mutual couplings between array elements are lower than  $-24$  dB with a working band of 4.36 GHz – 4.94 GHz. The measured realized gain and total efficiency are more than 6 dBi and 74% from 4.36 to 4.94 GHz, respectively. In addition, the radiation characteristics of array elements basically keep unchanged.



### 3.2.2 Paper B

#### **Mutual Decoupling for Massive MIMO Antenna Arrays by Using Triple-Layer Meta-Surface**

Shengyuan Luo, Yiming Zhang, Gert Frølund Pedersen, and Shuai Zhang

Published at the *IEEE Open Journal of Antennas and Propagation*, vol. 3, pp. 1079-1089, 2022.

#### **Paper content**

This paper introduces a decoupling method of Triple-Layer Meta-Surface (TMS) for massive MIMO arrays. The waves come from the bottom MS and top two-layer MS have the approaching same amplitudes and opposite phases, which enables perfect cancellation between these two kinds of space waves. To demonstrate the decoupling principle, a single-layer and dual-layer metasurface unit cell with different incident angles  $\theta$  are simulated. To verify the feasibility of the proposed decoupling method, a  $4 \times 4$  array with TMS is simulated, fabricated, and measured.

#### **Main results**

The calculated amplitude differences between the two kinds of reflected waves range from -0.1 to 0.02 when the incident angle of  $\theta$  varies from  $0^\circ$  to  $60^\circ$  with the step of  $20^\circ$ . The corresponding phase differences approach  $180^\circ$ . The simulation and measurement for the real example of a  $4 \times 4$  array with TMS show that the TMS can help reduce the coupling among the array elements to less than -24 dB within 4.23-4.82 GHz. The measured realized gain and total efficiency have a slight drop because of the power loss in feeding cables. The total efficiency of the  $4 \times 4$  array with TMS is more than 76%.

### 3.2.3 Paper C

#### **Massive MIMO Array Design with High Isolation by Using Decoupling Cavity.**

Shengyuan Luo, Gert Frølund Pedersen, and Shuai Zhang

Published at the *Published in:*

*IEEE Transactions on Circuits and Systems II: Express Briefs*.

#### **Paper content**

The pure superstrate is a promising means for reducing the coupling of massive MIMO arrays. This paper proposes a decoupling cavity (DC) with a period of an inner-element distance of arrays. The DC includes two-layer pure substrates with different thicknesses. Two cavities with different sizes are engraved on the two-layer substrate so that the DC will not affect the normal spread of the space wave in the normal direction. While the ramparts of DC unit cells with different sizes will introduce a low transmission in the parallel direction of the arrays. An actual  $4 \times 4$  array with DCs is designed. To enforce the decoupling performance, three-layer stacked DCs are loaded above the  $4 \times 4$  array. Finally, the corresponding prototype is fabricated, and measured.

### **Main results**

It is found that the coupling of the proposed array was decreased lower than -24 dB within the bandwidth of 4.21-4.79 GHz. Moreover, the radiation characteristics of the arrays with and without DC are almost unchanged. Owing to the inhibit for the spread of the space wave coupling component in the parallel direction, the realized gain and total efficiency of the prototype have significant increments. Comparing the E-field of the array with and without DCs, it illustrates that the E-field in the ramparts of DCs is extremely weaker than that without DCs.

## **3.2.4 Paper D**

### **Decoupling for Millimeter-Wave Array Antennas Using Near-Field Shrinking Dielectric Superstrate**

Shengyuan Luo, Yiming Zhang, Peng Mei, Gert Frølund Pedersen, and Shuai Zhang

Submitted at *IEEE Open Journal of Antennas and Propagation*.

### **Paper content**

This paper introduces a decoupling concept of near-field shrinking dielectric superstrate (NFSDS) for wideband, dual-polarized, and massive MIMO mm-wave arrays. When an NFSDS is seamlessly mounted above the array, the near-field electric field can be significantly shrunk, thereby reducing space wave coupling, while the surface wave coupling has a slight increment. By optimizing the permittivity and thickness of NFSDS, a trade-off scheme for the NFSDS is obtained by using a dual-element verification array. To verify the decoupling concept for the actual mm-arrays, an  $8 \times 8$  mm-wave array with NFSDS is simulated, fabricated, and measured.

## Main results

The E-fields of the actual array with different permittivities show that when the permittivity is selected as 1.6, it has a significant reduction for space wave coupling and a slight increment for surface wave coupling that can be neglected. By optimizing the thickness and permittivity the largest coupling reduction is carried, and the optimized thickness and permittivity of the NFSDS is 4 mm and 1.6, respectively. By loading the NFSDS, the total coupling of the  $8 \times 8$  mm-wave array could have a decrement of 6.2 dB (from -17 dB to -23.2 dB) from 24 – 29.5 GHz and 7 dB (from -17 dB to -24dB) from 26.8 – 29.5 GHz. Additionally, the realized gain and total efficiency of the array elements are effectively improved by loading the NFSDS above the original array. Furthermore, It can be found that the 3dB gain drop beam scanning capability of the original array in the x-direction and y-direction is  $-47^\circ$ – $47^\circ$  and  $-33^\circ$ – $33^\circ$ , respectively, while the decoupled array has a 3dB gain drop beam scanning capability of  $-56^\circ$ – $57^\circ$  and  $-38^\circ$ – $38^\circ$  in x-direction and y-direction, respectively.

## 4. Conclusion

The basic array element used in my thesis is the dual-layer stacked microstrip antenna that performs wideband and dual-polarization features. These are fed by coaxial cables, and the distance between array elements is half-wavelength so that the dominant coupling type is space wave coupling. To decrease the coupling of the wideband and dual-polarization massive MIMO array four decoupling methods are proposed in my thesis, compasses single-layer non-resonant metasurface (NRMS), triple-layer metasurface (TMS), decoupling cavity (DC), near-field shrinking dielectric superstrate (NFSDS).

Because of the engraved square air cavity, the NRMS performs a negative dielectric and positive permittivity so that the propagation of the space wave coupling component in tangential will be suppressed, while the space wave can normally propagate in the normal direction. Because of the feature of non-resonant, the proposed metasurface unit cell has a stable permittivity and permeability over a wide working band, which can satisfy the fundamental requirement of a massive MIMO array. By loading the proposed NRMS, the couplings between neighbor and non-neighbor array elements in orthogonal and diagonal directions can be reduced to lower than -24 dB simultaneously. While the radiation patterns of the array element almost have no change.

Different from the first decoupling method of NRMS, the second decoupling method of triple-layer metasurface (TMS) divides the space wave coupling of a massive MIMO array into two parts. The triple-layer metasurface introduce two paths of reflection wave, respectively. The reflection wave from the bottom layer metasurface and top two-layer metasurface has the approaching same amplitudes and opposite phases so that the two reflected space wave coupling components will be cancelled with each other. By adjusting the distance and the sizes of the metasurface unit cell, a phase difference of  $180^\circ$  between two reflected space wave coupling components will be obtained. By loading the TMS above the massive MIMO array, the coupling of array can be reduced to less than -24 dB within 4.23-4.82 GHz, and the radiation patterns of array elements is almost not affected.

The decoupling cavity (DC) is a promising candidate for isolation enhancement for massive MIMO arrays because of its unique features of cheaply can easily be fabricated. The high insertion loss is generated by the ramparts of DC. However, the spread of space waves in the normal direction is not affected because it has an air cavity above every array element. To enforce the decoupling effect, the three layers of DCs are seamlessly mounted above the massive MIMO array, high isolation of 24 dB of the array can be achieved. Additionally, the array has a wide working band of 4.21-4.79 GHz.

The mm-wave massive MIMO array is an important research area for 5G and 6G. Different from the array with a working band of sub-6 GHz, the actual space between mm-wave array elements is extremely small. Therefore, the previously mentioned decoupling methods are not suitable for the mm-wave application. Inspired by the third decoupling method of DC, a decoupling method of near-field shrinking dielectric superstrate (NFSDS) is proposed. By optimizing the thickness and permittivity of the NFSDS, a trade-off solution between space wave coupling reduction and surface wave coupling increment can be obtained, thereby the largest reduction for total coupling can be obtained. The proposed NFSDS with low permittivity of 1.6 can be got by drilling air holes on pure polypropylene (PP). After loading the NFSD, the coupling of the mm-wave array has a decrement of 6.2 dB (from -17 dB to -23.2 dB) from 24 – 29.5 GHz and 7 dB (from -17 dB to -24dB) from 26.8 – 29.5 GHz. At the same time, the decoupled array has a 3dB gain drop beam scanning capability of  $-56^\circ$ – $57^\circ$  and  $-38^\circ$ – $38^\circ$  in the x-direction and y-direction, respectively. Compared to other existing decoupling methods, the proposed technique of NFSDS overcomes the defects of difficulty fabrication and sensitivity to the distance between a massive MIMO array and its

metasurface. Therefore, less fabrication tolerance will be introduced in my designed massive MIMO mm-wave array.

## References

- [1] X. Wei, Z. Kan, X. S. Shen, "5G mobile communication," *Switzerland: Springer*, 2016, 4-40.
- [2] L. Chettri and R. Bera, "A comprehensive survey on Internet of Things (IoT) toward 5G wireless systems," *IEEE Internet Thing Journal*, Vol. 7, No. 1, PP. 16-32, Jan. 2020.
- [3] C. T. Liao, Z. K. Yang, and H. M. Chen, "Multiple integrated antennas for wearable fifth-generation communication and Internet of Things applications," *IEEE Access*, vol. 9, pp. 120328–120346, 2021.
- [4] A. Moglia, K. Georgiou, B. Marinov, E. Georgiou, R. N. Berchiolli, R. M. Satava, and A. Cuschieri, "5G in healthcare: From COVID-19 to future challenges," *IEEE J. Biomed. Health Informat.*, vol. 26, no. 8, pp. 4187–4196, Aug. 2022.
- [5] C. R. Storck and F. Duarte-Figueiredo, "A survey of 5G technology evolution, standards, and infrastructure associated with vehicle-to-everything communications by Internet of Vehicles," *IEEE Access*, vol. 8, pp. 117593–117614, 2020.
- [6] W. Dias, A. Ferreira, R. Kagami, J. S. Ferreira, D. Silva, and L. Mendes, "5G-RANGE: A transceiver for remote areas based on software-defined radio," *Proc. Eur. Conf. Netw. Commun. (EuCNC)*, Jun. 2020, pp. 100–104.
- [7] P. Saikia, S. Biswas, K. Singh, and C. -P. Li, "Signal Detection in GSM-Based In-Band Full-Duplex Communication Using DNN," *IEEE Trans. on Veh. Technol.*, vol. 72, no. 2, pp. 2661-2666, Feb. 2023.
- [8] Z. Wang, T. Liang, and Y. Dong, "Compact In-Band Full Duplexing Antenna for Sub-6 GHz 5G Applications," *IEEE Antennas Wireless Propag. Lett.* vol. 20, no. 5, pp. 683-687, May 2021.
- [9] F. Haider, C. -X. Wang, H. Haas, E. Hepsaydir, X. Ge and D. Yuan, "Spectral and Energy Efficiency Analysis for Cognitive Radio Networks," *IEEE Trans. on Wireless Commun.*, vol. 14, no. 6, pp. 2969-2980, Jun. 2015.

- [10] B. Feng, J. Lai, K. L. Chung, T. -Y. Chen, Y. Liu, and C. -Y. -D. Sim, "A Compact Wideband Circularly Polarized Magneto-Electric Dipole Antenna Array for 5G Millimeter-Wave Application," *IEEE Trans. Antennas Propag.*, vol. 68, no. 9, pp. 6838-6843, Sep. 2020.
- [11] F. A. Pereira de Figueiredo, "An Overview of Massive MIMO for 5G and 6G," *IEEE Latin America Trans.*, vol. 20, no. 6, pp. 931-940, Jun. 2022.
- [12] L. Zhao, K. Li, K. Zheng, and M. Omair Ahmad, "An Analysis of the Tradeoff Between the Energy and Spectrum Efficiencies in an Uplink Massive MIMO-OFDM System," *IEEE Trans. on Circuits and Systems II: Express Briefs*, vol. 62, no. 3, pp. 291-295, Mar. 2015.
- [13] X. Meng, X. Gao, and X. -G. Xia, "Omnidirectional Precoding Based Transmission in Massive MIMO Systems," *IEEE Trans. on Commun.*, vol. 64, no. 1, pp. 174-186, Jan. 2016.
- [14] Y. Xin, D. Wang, J. Li, H. Zhu, J. Wang, and X. You, "Area Spectral Efficiency and Area Energy Efficiency of Massive MIMO Cellular Systems," *IEEE Trans. on Veh. Technol.*, vol. 65, no. 5, pp. 3243-3254, May 2016.
- [15] T. L. Marzetta, "Noncooperative cellular wireless with unlimited numbers of base station antenna," *IEEE Trans. Wireless Commun.*, vol. 9, no. 11, pp. 3950-3600, Nov. 2010.
- [16] E. G. Larsson, O. Edfors, F. Tufvesson, and T. Marzetta, "Massive MIMO for next generation wireless systems," *IEEE Commun. Mag.*, vol. 52, no. 2, pp. 186-195, Feb. 2014.
- [17] F. Rusek et al., "Scaling up MIMO: Opportunities and challenges with very large arrays," *IEEE Signal Process. Mag.*, vol. 30, no. 1, pp. 40-60, Jan. 2013.
- [18] K. Xu, J. Zhang, X. Yang, S. Ma, and G. Yang, "On the sum-rate of RIS assisted MIMO multiple-access channels over spatially correlated Rician fading," *IEEE Trans. Commun.*, vol. 69, no. 12, pp. 8228-8241, Dec. 2021.
- [19] E. G. Larsson, O. Edfors, F. Tufvesson, and T. L. Marzetta, "Massive MIMO for next generation wireless systems," *IEEE Commun. Mag.*, vol. 52, no. 2, pp. 186-195, Feb. 2014.
- [20] M. Kacar, T. M. Weller, and G. Mumcu, "3D Printed Wideband Multilayered Dual-Polarized Stacked Patch Antenna With Integrated MMIC Switch," *IEEE Open Journal of Antennas and Propag.*, vol. 2, pp. 38-48, 2021.

- [21] K. S. Ryu, and A. A. Kishk, "Wideband Dual-Polarized Microstrip Patch Excited by Hook Shaped Probes," *IEEE Trans. Antennas Propag.*, vol. 56, no. 12, pp. 3645-3649, Dec. 2008.
- [22] B. Li, Y. -Z. Yin, W. Hu, Y. Ding, and Y. Zhao, "Wideband Dual-Polarized Patch Antenna With Low Cross Polarization and High Isolation," *IEEE Antennas Wireless Propag. Lett.*, vol. 11, pp. 427-430, 2012.
- [23] W. Qiu, C. Chen, H. Zhang, and W. Chen, "A Wideband Dual-Polarized L-Probe Antenna Array With Hollow Structure and Modified Ground Plane for Isolation Enhancement," *IEEE Antennas Wireless Propag. Lett.*, vol. 16, pp. 2820-2823, 2017.
- [24] Z. Tang, J. Liu, and Y. Yin, "Enhanced Cross-Polarization Discrimination of Wideband Differentially Fed Dual-Polarized Antenna via a Shorting Loop," *IEEE Antennas Wireless Propag. Lett.*, vol. 17, no. 8, pp. 1454-1458, Aug. 2018.
- [25] J. Zhang, X. Q. Lin, L. Y. Nie, J. W. Yu, and Y. Fan, "Wideband Dual-Polarization Patch Antenna Array With Parallel Strip Line Balun Feeding," *IEEE Antennas Wireless Propag. Lett.*, vol. 15, pp. 1499-1501, 2016
- [26] L. -H. Wen et al., "A Wideband Differentially Fed Dual-Polarized Antenna With Wideband Harmonic Suppression," *IEEE Trans. Antennas Propag.*, vol. 67, no. 9, pp. 6176-6181, Sept. 2019.
- [27] Y. -H. Ren, J. Ding, C. -J. Guo, Y. Qu, and Y. -C. Song, "A Wideband Dual-Polarized Printed Antenna Based on Complementary Split-Ring Resonators," *IEEE Antennas Wireless Propag. Lett.*, vol. 14, pp. 410-413, 2015.
- [28] K. Wang et al., "A Dual-Wideband Dual-Polarized Aperture-Shared Patch Antenna With High Isolation," *IEEE Antennas Wireless Propag. Lett.*, vol. 17, no. 5, pp. 735-738, May 2018.
- [29] P. Mei, Y. -M. Zhang, and S. Zhang, "Decoupling of a Wideband Dual-Polarized Large-Scale Antenna Array With Dielectric Stubs," *IEEE Trans. on Veh. Technol.*, vol. 70, no. 8, pp. 7363-7374, Aug. 2021.
- [30] X. L. Bao, and M. J. Ammann, "Wideband Dual-Frequency Dual-Polarized Dipole-Like Antenna," *IEEE Antennas Wireless Propag. Lett.*, vol. 10, pp. 831-834, 2011.
- [31] W. Yang, and Y. Pan, "A Wideband Dual-Polarized Dipole Antenna With Folded Metallic Plates," *IEEE Antennas Wireless Propag. Lett.*, vol. 17, no. 10, pp. 1797-1801, Oct. 2018.

- [32] Y. Gou, S. Yang, J. Li, and Z. Nie, "A Compact Dual-Polarized Printed Dipole Antenna With High Isolation for Wideband Base Station Applications," *IEEE Trans. Antennas Propag.*, vol. 62, no. 8, pp. 4392-4395, Aug. 2014.
- [33] L. H. Ye, Y. J. Li, and D. -L. Wu, "Dual-Wideband Dual-Polarized Dipole Antenna With T-Shaped Slots and Stable Radiation Pattern," *IEEE Antennas Wireless Propag. Lett.*, vol. 21, no. 3, pp. 610-614, March 2022.
- [34] L. H. Ye, X. Y. Zhang, Y. Gao, and Q. Xue, "Wideband Dual-Polarized Four-Folded-Dipole Antenna Array With Stable Radiation Pattern for Base-Station Applications," *IEEE Trans. Antennas Propag.*, vol. 68, no. 6, pp. 4428-4436, June 2020.
- [35] X. Liu et al., "A Mutual-Coupling-Suppressed Dual-Band Dual-Polarized Base Station Antenna Using Multiple Folded-Dipole Antenna," *IEEE Trans. Antennas Propag.*, vol. 70, no. 12, pp. 11582-11594, Dec. 2022.
- [36] K. Xue, D. Yang, C. Guo, H. Zhai, H. Li, and Y. Zeng, "A Dual-Polarized Filtering Base-Station Antenna With Compact Size for 5G Applications," *IEEE Antennas Wireless Propag. Lett.*, vol. 19, no. 8, pp. 1316-1320, Aug. 2020.
- [37] J. Zhang, K. Yang, E. Eide, S. Yan, and G. A. E. Vandenbosch, "Simple Triple-Mode Dual-Polarized Dipole Antenna With Small Frequency Separation Ratio," *IEEE Antennas Wireless Propag. Lett.*, vol. 19, no. 2, pp. 262-266, Feb. 2020.
- [38] M. Li, Q. L. Li, B. Wang, C. F. Zhou, and S. W. Cheung, "A Low-Profile Dual-Polarized Dipole Antenna Using Wideband AMC Reflector," *IEEE Trans. Antennas Propag.*, vol. 66, no. 5, pp. 2610-2615, May 2018.
- [39] X. Dai, and K. M. Luk, "A Wideband Dual-Polarized Antenna for Millimeter-Wave Applications," *IEEE Trans. Antennas Propag.*, vol. 69, no. 4, pp. 2380-2385, April 2021.
- [40] Y. Gou, S. Yang, J. Li, and Z. Nie, "A Compact Dual-Polarized Printed Dipole Antenna With High Isolation for Wideband Base Station Applications," *IEEE Trans. Antennas Propag.*, vol. 62, no. 8, pp. 4392-4395, Aug. 2014.
- [41] Y. Li, and K. -M. Luk, "60-GHz Dual-Polarized Two-Dimensional Switch-Beam Wideband Antenna Array of Aperture-Coupled Magneto-Electric Dipoles," *IEEE Trans. Antennas Propag.*, vol. 64, no. 2, pp. 554-563, Feb. 2016.



- [42] Y. C. Chang, C. C. Hsu, M. I. Magray, H. Y. Chang, and J. -H. Tarng, "A Novel Dual-Polarized Wideband and Miniaturized Low Profile Magneto-Electric Dipole Antenna Array for mmWave 5G Applications," *IEEE Open Journal of Antennas and Propagation*, vol. 2, pp. 326-334, 2021.
- [43] D. Yang, H. Zhai, C. Guo, and C. Ma, "A Novel Differentially Fed Dual-Polarized Filtering Magneto-Electric Dipole Antenna for 5G Base Station Applications," *IEEE Trans. Antennas Propag.*, vol. 70, no. 7, pp. 5373-5382, July 2022.
- [44] F. Wu, J. Wang, L. Xiang, W. Hong, and K. -M. Luk, "A Wideband Dual-Polarized Magneto-Electric Dipole Transmitarray With Independent Control of Polarizations," *IEEE Trans. Antennas Propag.*, vol. 70, no. 9, pp. 8632-8636, Sept. 2022.
- [45] S. Chen, and K. -M. Luk, "A Dual-Mode Wideband MIMO Cube Antenna With Magneto-Electric Dipoles," *IEEE Trans. Antennas Propag.*, vol. 62, no. 12, pp. 5951-5959, Dec. 2014.
- [46] F. Wu, J. Wang, Y. Zhang, W. Hong, and K. -M. Luk, "A Broadband Circularly Polarized Reflectarray With Magneto-Electric Dipole Elements," *IEEE Trans. Antennas Propag.*, vol. 69, no. 10, pp. 7005-7010, Oct. 2021.
- [47] R. C. Paryani, P. F. Wahid and N. Behdad, "A Wideband, Dual-Polarized, Substrate-Integrated Cavity-Backed Slot Antenna," *IEEE Antennas Wireless Propag. Lett.*, vol. 9, pp. 645-648, 2010.
- [48] X. Jiang, Z. Zhang, Y. Li, and Z. Feng, "A Wideband Dual-Polarized Slot Antenna," *IEEE Antennas Wireless Propag. Lett.*, vol. 12, pp. 1010-1013, 2013.
- [49] B. Peng, S. Li, J. Zhu, L. Deng, and Y. Gao, "A Compact Wideband Dual-Polarized Slot Antenna With Five Resonances," *IEEE Antennas Wireless Propag. Lett.*, vol. 16, pp. 2366-2369, 2017.
- [50] C. Wang, Y. Chen, and S. Yang, "Bandwidth Enhancement of a Dual-Polarized Slot Antenna Using Characteristic Modes," *IEEE Antennas Wireless Propag. Lett.*, vol. 17, no. 6, pp. 988-992, June 2018.
- [51] Q. You, Y. Wang, M. Huang, J. Huang, Z. -W. Zheng, and Y. Lu, "Wideband Dual-Polarized Hollow-Waveguide Slot Array Antenna," *IEEE Trans. Antennas Propag.*, vol. 70, no. 10, pp. 9326-9336, Oct. 2022.
- [52] H. J. Song, A. Bekaryan, J. H. Schaffner, A. Hussain, and P. -S. Kildal, "Effects of Mutual Coupling on LTE MIMO Capacity for Monopole

- Array: Comparing Reverberation Chamber Tests and Drive Tests," *IEEE Antennas Wireless Propag. Lett.*, vol. 14, pp. 454-457, 2015.
- [53] A. H. Song and Y. J. Cheng, "Shared-Aperture Dual-Polarized Ku-Band, and Single-Polarized Ka-Band Phased Array Antenna With Scanning Coverage Enhancement," *IEEE Trans. Antennas Propag.*, vol. 70, no. 11, pp. 10426-10435, Nov. 2022.
- [54] M. A. Azam, A. K. Dutta, and A. Mukherjee, "Performance Analysis of Dipole Antenna Based Planar Arrays With Mutual Coupling and Antenna Position Error in mmWave Hybrid System," *IEEE Trans. on Veh. Technol.*, vol. 70, no. 10, pp. 10209-10221, Oct. 2021.
- [55] Q. Yuan, Q. Chen, and K. Sawaya, "Performance of adaptive array antenna with arbitrary geometry in the presence of mutual coupling," *IEEE Trans. Antennas Propag.*, vol. 54, no. 7, pp. 1991-1996, July 2006.
- [56] C. M. Schmid, S. Schuster, R. Feger, and A. Stelzer, "On the Effects of Calibration Errors and Mutual Coupling on the Beam Pattern of an Antenna Array," *IEEE Trans. Antennas Propag.*, vol. 61, no. 8, pp. 4063-4072, Aug. 2013.
- [57] J. R. James, P. S. Hall, and C. Wood, *Microstrip Antenna: Theory and Design*. Edison, NJ, USA: IET, 1986.
- [58] D. G. Duffy, "Response of a grounded dielectric slab to an impulse line source using leaky modes," *IEEE Trans. Antennas Propag.*, vol. 42, no. 3, pp. 340-346, March 1994.
- [59] C. A. Balanis, *Advanced Engineering Electromagnetics*. Hoboken, NJ, USA: Wiley, 1999.
- [60] R. H. Jordan and D. G. Hall, "Radiation from concentric-circle grating, surface-emitting planar waveguides: The volume current method," *Appl. Phys. Lett.*, vol. 64, no. 23, pp. 3077-3079, Jun. 1994.
- [61] J. R. James, P. S. Hall, and C. Wood, *Microstrip Antenna: Theory and Design*. Edison, NJ, USA: IET, 1986.
- [62] "Micromachined microstrip patch antenna with controlled mutual coupling and surface waves," *IEEE Trans. Antennas Propag.*, vol. 49, no. 9, pp. 1282-1289, Sep. 2001.
- [63] W. C. Chew, *Waves and Fields in Inhomogeneous Media*. Piscataway, NJ, USA: IEEE Press, 1996.
- [64] M. Li, M. Y. Jamal, L. Jiang and K. L. Yeung, "Isolation Enhancement for MIMO Patch Antennas Sharing a Common Thick Substrate: Using a Dielectric Block to Control Space-Wave Coupling

- to Cancel Surface-Wave Coupling," *IEEE Trans. Antennas Propag.*, vol. 69, no. 4, pp. 1853-1863, April 2021.
- [65] R. L. Haupt, "Lowering the Sidelobe Level of a Two-Way Array Factor for an Array With Uniform Transmit and Uniform Receive Arrays," *IEEE Trans. Antennas Propag.*, vol. 67, no. 6, pp. 4253-4256, June 2019.

## Part II Papers



# Paper A

Decoupling of Dual-Polarized Antenna Arrays Using Non-Resonant Metasurface

Shengyuan Luo, Peng Mei, Yiming Zhang, Gert Frølund  
Pedersen, Shuai Zhang

This paper has been published at the  
Published at the Sensors, DOI: 10.3390/s23010152



## Abstract

*Non-resonant metasurface (NRMS) concept is reported in this paper to improve the isolation of dual-polarized and wideband large-scale antenna arrays. By properly designing the NRMS, it can perform stable negative permeability and positive permittivity along the tangential direction of the NRMS within a wide band, which can be fully employed to suppress the mutual couplings of large-scale antenna arrays. At the same time, the proposed NRMS can also result in positive permittivity and permeability along the normal direction of the NRMS, which guarantees the free propagation of electromagnetic waves from antenna arrays along the normal direction. For demonstration, a  $4 \times 4$  dual-polarized antenna array loading with the proposed NRMS is designed to improve the isolations of the antenna array. The simulations demonstrate that the isolations among all ports are over 24 dB from 4.36 to 4.94 GHz, which are experimentally verified by the measured results. Moreover, the radiation patterns of antenna elements are still maintained after leveraging the proposed NRMS. Due to the simple structure of the proposed NRMS, it is very promising to be widely employed for massive MIMO antenna arrays.*

## 1 Introduction

Large-scale antenna arrays, consisting of numerous antenna elements, are promising candidates for the 5G and future 6G applications [1–8]. To maintain the performance of large-scale antenna arrays, mutual couplings among antenna elements should be much considered, as poor couplings will seriously deteriorate the antenna performance, such as power amplifier efficiency, active VSWR, channel capacity, radiation efficiency, impedance match, and signal-to-noise ratio [9–15].

In the past few decades, researchers have made much effort to reduce the interferences between array elements, and different methods have been proposed [16–21]. The first method is directly suppressing the propagation of surface wave coupling and space wave coupling, such as electromagnetic bandgap (EBG) structures [16], defected ground (DGS) [17], and resonators [18]. These methods can effectively reduce the coupling of the array based on the frequency responses of these decoupling structures, yet these decoupling structures usually work in a narrow band. These decoupling structures are also complicated and bulky to achieve the desired frequency responses for mutual coupling reductions and must be inserted between array elements, which need relatively large space. On the other hand, due to the frequency responses of the decoupling structures being polarization-dependent, they are not feasible



for application in dual-polarized antenna arrays. As a result, the decoupling methods mentioned above are difficult for extension to massive MIMO arrays. The second solution is to introduce an extra coupling path to cancel the original coupling, such as neutralization lines [19] and parasitic element structure [20,21], which suffer from a strict requirement for the volume to achieve integration with antenna arrays. Therefore, it is hard to be used in large-scale arrays as well. At the same time, most of these decoupling structures are applied in single-polarized antenna arrays. Some of the literature on the decoupling of dual-polarized and large-scale antenna arrays has been reported [22–26]. The decoupling network [22–24] is an effective method. The decoupling network in [24] can reduce the coupling of the array from  $-15$  dB to  $-28$  dB. Notably, the decoupling network has a completely different working principle from the neutralization line, which introduces transmission lines and parallel reactance to enable the transmission admittance to be zero, thus achieving the purpose of decoupling. However, the decoupling network commonly needs a matching network to make the antenna achieve good impedance matching. It cannot be used in wideband arrays owing to the feature of resonant-based frequency responses of the decoupling network. A decoupling surface (ADS) is proposed in [25,26], which consists of a group of primary and accessorial reflectors to create partial reflective waves to cancel the unwanted coupling waves between array elements. However, constructing proper metal patterns of the ADS to cancel the reflecting waves has a complicated design process. In [26], a  $4 \times 4$  staggered array with diversified phase laggings and coupling level lower than  $-25$  dB is designed by loading the ADS. In [27], the decoupling dielectric stubs (DDS) are proposed to reduce the mutual couplings of a  $4 \times 4$  antenna array below  $-25$  dB from 4.4 to 4.8 GHz. However, it requires a relatively high profile (half wavelength). In [28], a decoupling ground (DG) method is presented. An improvement of about 7 dB isolation has been obtained with the inner-element distance around  $0.62\lambda$ . Nevertheless, it needs a large inter-element distance to enable the space wave coupling and surface wave coupling with the same amplitude and opposite phase to perfectly cancel each other.

Metasurface has been proposed very recently as a promising solution to reduce the mutual coupling of antenna arrays. In [29,30], a metasurface has been introduced to create a region with negative permeability and positive permittivity to suppress the coupling waves of two-element antenna arrays. A permittivity–negative metasurface superstrate was studied to reduce the mutual couplings of large antenna arrays [31]. However, the metasurface is based on resonant structures that cannot be extended for wideband applications. In addition, it is not feasible to be applied to dual-polarized

arrays due to the asymmetric geometry along vertical and horizontal directions simultaneously.

This paper proposes a non-resonant metasurface (NRMS) and places it above a  $4 \times 4$  dual-polarized and large-scale antenna array for isolation enhancements. The NRMS can be equivalent to a medium with a negative permeability and a positive permittivity to suppress the coupling along the tangential direction of arrays. The isolation can be improved from 15 dB to 24 dB within 4.36–4.94 GHz after loading the proposed NRMS. Unlike the previous metasurface decoupling methods, the equivalent permeability and permittivity of the NRMS are extracted from the non-resonant working band. Thus, the NRMS element has an ultra-wide operating band with negative permeability for decoupling. The extracted parameters of the proposed NRMS are almost unchanged with different incident angles. Unlike the traditional metasurface [29–31], the proposed NRMS units in this paper are symmetric in two dimensions besides their wideband and wide angle decoupling performance. Therefore, the proposed decoupling method can be utilized for large planar dual-polarized phased arrays with complex electromagnetic coupling paths. Due to its low profile, low complexity, and wide bandwidth, the proposed NRMS is a good candidate for reducing mutual couplings of dual-polarized and large scale antenna arrays.

This paper is organized as follows. In Section 2, the operating mechanism of the NRMS is explained. Then, a procedure of a dual-element dual-polarized antenna array with NRMS is elaborated on to verify the effectivity of the proposed decoupling method. To verify the feasibility of the proposed decoupling method for large-scale antenna arrays, a  $4 \times 4$  dual-polarized antenna array with NRMS is designed, and its corresponding performance, parametric study, and the comparison between our work and the techniques employed in the latest literature are presented in Section 3 as well. Section 4 provides the conclusions.

## **2 Non-Resonant Metasurface for Decoupling**

The free-space wave coupling mainly causes the mutual coupling between massive antenna array elements with a half-wavelength distance. Therefore, the metasurface employed above the array is mainly used to reduce the free-space coupling path. This section will investigate the scheme of the proposed isolation improvement method in detail. The decoupling principle will be analyzed based on a massive MIMO antenna array sketch with NRMS. The NRMS unit cell is studied under TE and TM modes when the incidence

waves propagate in various directions to analyze the effects on the extracted permittivity and permeability to investigate the design procedure of NRMS. Then, the decoupling principle is studied in detail with an example of dual-element dual-polarized antenna array.

## 2.1 Decoupling Scheme of the NRMS

The sketch of the isolation enhancement principle with NRMS is shown in Figure 1a. The space waves radiated from the element P3 can be broadly represented with  $a_1$  and  $a_2$ , where  $a_1$  and  $a_2$  are responsible for the mutual coupling between adjacent and non-adjacent antenna elements, respectively. When the NRMS is placed above the array with a distance of  $h$ , the NRMS can be equivalent to a negative permeability and positive permittivity medium along the tangential (or  $x$ -axis) direction of the NRMS when the unit cell of the NRMS is properly designed, where the propagation constant is purely imaginary. As a result, the propagation of the  $a_1$  and  $a_2$  at the tangential direction of the array will be prohibited. Unlike the resonant-based MS that only works in a narrow band, this paper proposes a non-resonant and symmetric MS for wideband and dual-polarized large-scale antenna arrays.

The geometry of the proposed NRMS unit cell is shown in Figure 1b, developed from the periodic cross-shaped ring, and an air cavity is engraved on the center of the NRMS. The metal strips with a 0.5 mm width are printed on the RO 4350B substrate with a permittivity of 3.66, a loss tangent of 0.002, and a thickness of 1.524 mm.

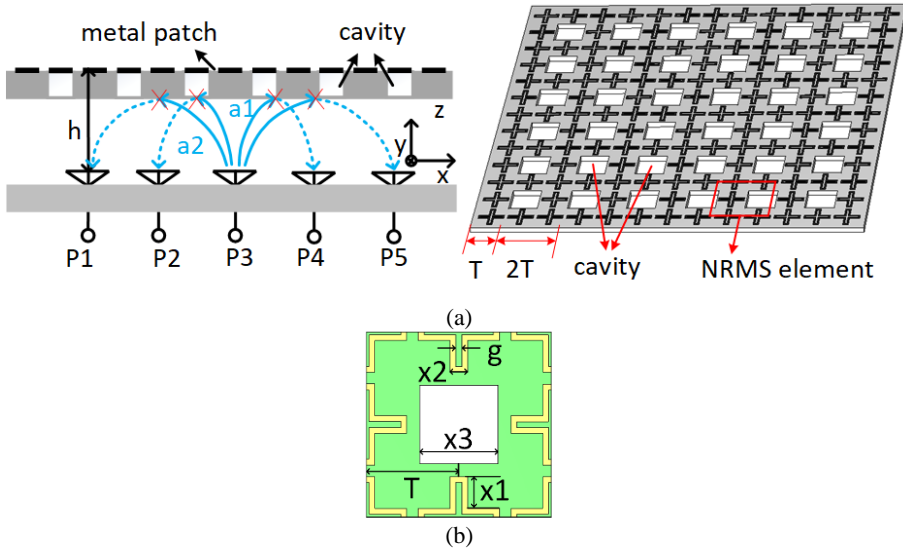
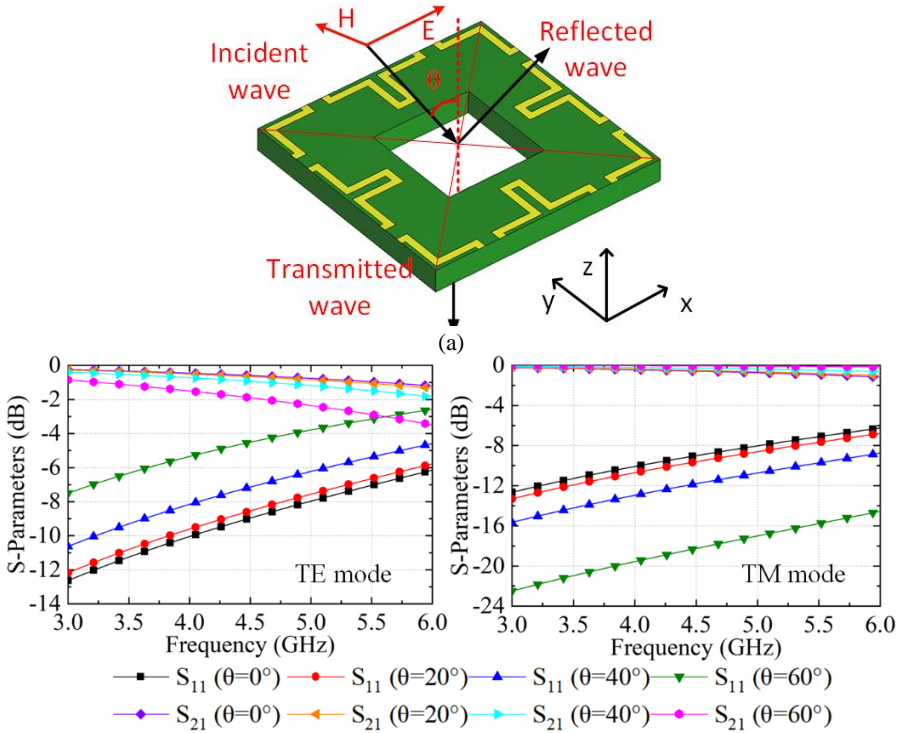


Figure 1. (a) the decoupling principle of the NRMS for the large-scale antenna array, (b) the detailed structure and dimensions of the unit cell to implement the NRMS.

## 2.2 Study for the NRMS Unit Cell

Figure 2a shows the simulation model of the unit cell of the NRMS when the incidence waves impinge on it normally, where the E-field of the incidence waves in the tangential direction of the NRMS and the H-field of the incident waves in the vertical direction of the propagation direction of the incident waves. Wave ports are embedded on the top and bottom surfaces of the unit cell without any air gaps. The simulated S-parameters under TE and TM modes at different incident angles of  $\theta$  offset the normal direction are provided in Figure 2b. The  $S_{11}$  is less than  $-2.5$  dB for TE mode, while it is lower than  $-6$  dB for TM mode within  $60^\circ$  from 3 to 5 GHz. The extracted permittivity and permeability under TE and TM modes with different  $\theta$  are given in Figure 2c,d, respectively. Both the extracted permittivity and permeability of the unit cell under TE and TM incidence waves at different angles of  $\theta$  are positive, which means that the space waves along the normal direction of the NRMS can propagate through the unit cell freely.



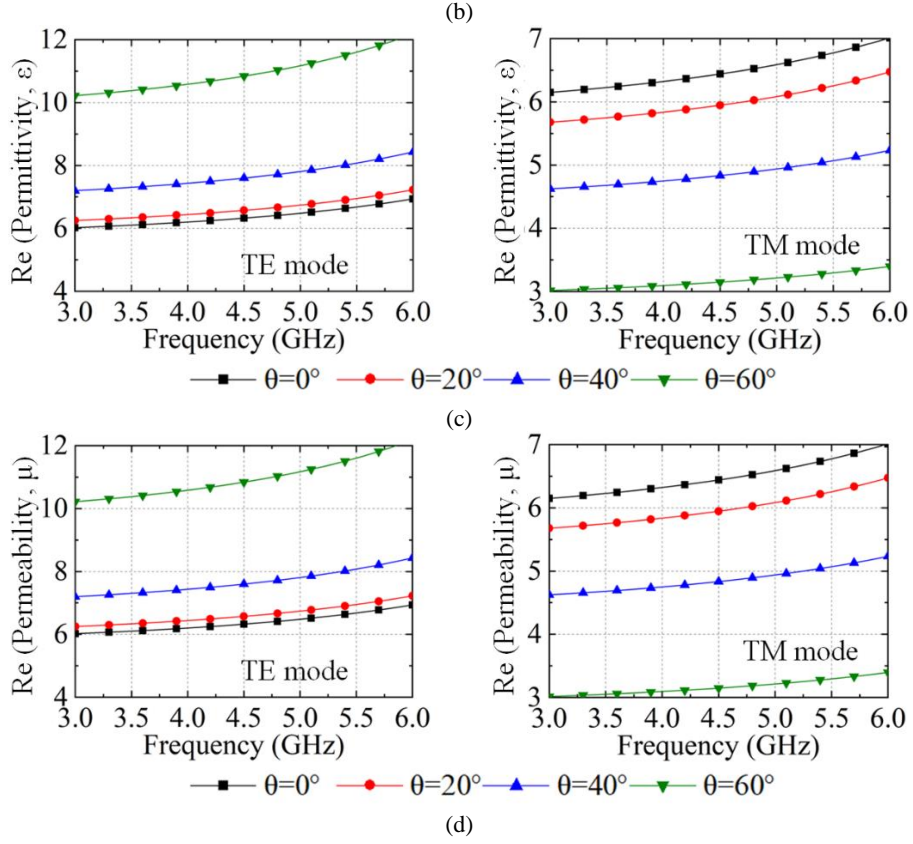


Figure 2. NRMS unit cell with incident angle along the normal direction of the surface: (a) the simulation model, (b) the S-parameters under TE and TM incidence waves at different incident angles, (c) the real part of the permittivity under TE and TM incidence waves at different incident angles, and (d) the real part of the permeability under TE and TM incidence waves at different incident angles.

Figure 3a illustrates the simulation model of the unit cell when the incidence waves propagate along the tangential direction of the unit cell, where the H-field of the incidence waves are in the vertical direction of the unit cell, and the E-field is perpendicular to the direction of the incidence waves. The wave ports are also embedded on the left and right sides of the unit cell. Figure 3b shows the simulated S-parameters under TM mode incidence wave at different incident angles of  $\phi$ , where it shows the  $S_{21}$  is less than  $-9$  dB. The extracted permittivity and permeability under TM incidence wave at different incidence angles can be found in Figure 3c,d. The NRMS unit cell exhibits a negative permeability from 3.0 to 5.1 GHz, while the extracted permittivity is positive within the same band. The S-parameters and the corresponding extracted

equivalent parameters demonstrate that the space waves coupling under TM incidence wave cannot propagate along the tangential direction of the unit cell. It is also found that the extracted permittivity and permeability of the NRMS under TE mode are all positive, indicating that the NRMS cannot suppress the mutual couplings generated by TE modes. This specifies a design idea that an anisotropic NRMS can be properly configured to offer negative permeability and positive permittivity for both TE and TM modes to further reduce the mutual couplings among antenna elements, which is our future work. Owing to the features of wideband and geometry symmetric along the orthogonal directions, the proposed NRMS unit cell is promising to reduce the mutual couplings of wideband and dual-polarized large-scale antenna arrays.

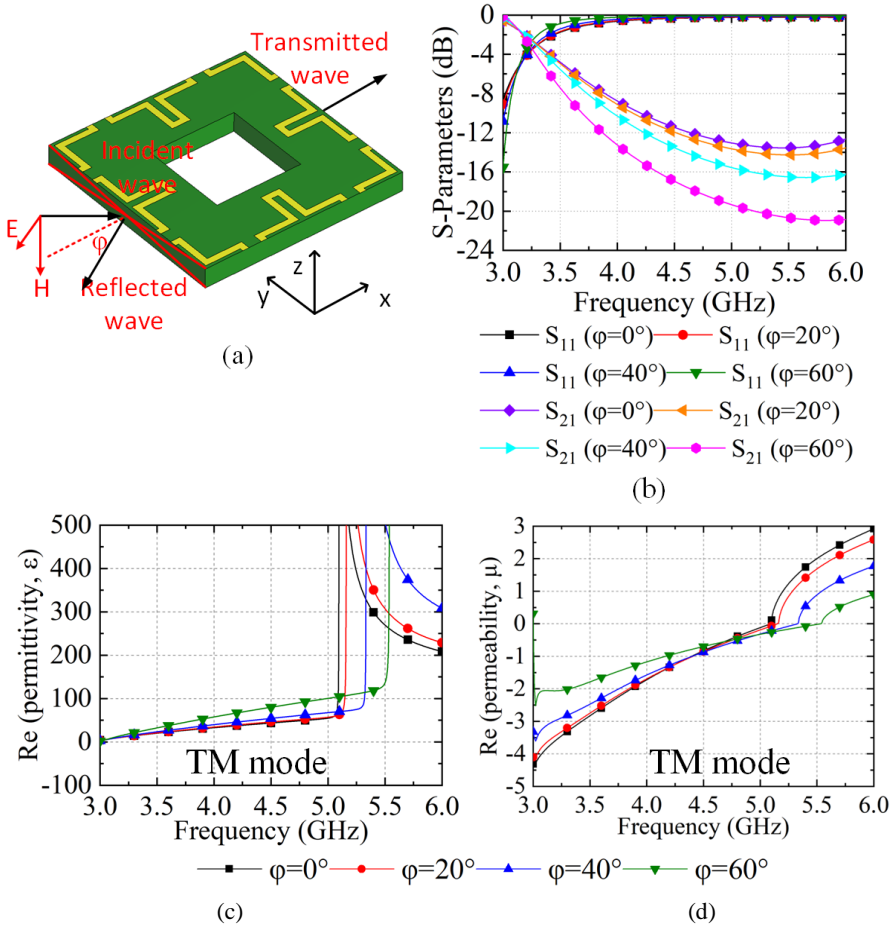
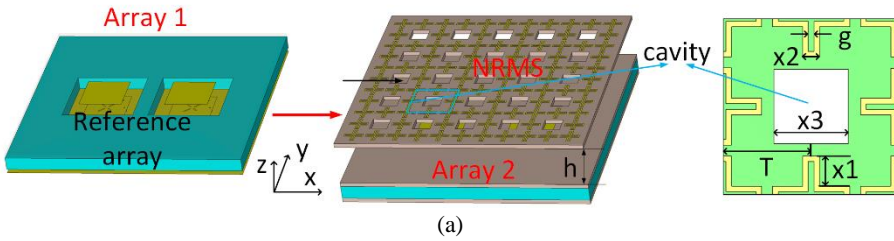


Figure 3. NRMS unit cell with incident angle along the tangent direction of the surface: (a) the simulation model, (b) the S-parameters, (c) the real part of the permittivity in different incident angles, and (d) the real part of the permeability in different incident angles.

### 2.3 Decoupling of A Two-Element Antenna Array with the NRMS

In this section, an example of a dual-element antenna array with a NRMS is given to verify the decoupling performance of the proposed NRMS. The design procedure of the isolation improvement for a dual-element dual-polarized antenna array with NRMS and the configuration of the reference array in the design procedure is given in Figure 4a,b, respectively. This array implements stacked microstrip antenna elements to obtain a broad operating bandwidth. The square metal patch is printed on the top surface of the RO 4350B substrate with a permittivity of 3.66 and a loss tangent of 0.002. The center-to-center distance between the array elements is 16.5 mm ( $0.5\lambda$  at the center frequency). Four orthogonal slots are etched on the bottom square patch to reduce the cross-polarized mutual coupling between two ports of the antenna array element itself. A PP (polypropylene) board with a permittivity of 2.2 is placed above the lower layer substrate to support the upper layer patch antenna. Then two cavities on the corresponding position of the antenna array elements are engraved to provide a space for the PCB board solder. Port1 and Port2 work in x-polarization, while Port3 and Port4 work in y-polarization. Here, the PP board does not have any other impact on the antenna performance besides supporting the two-layer substrates. The reference antenna array shown in Figure 4a is labeled as Array 1. In the next step, Array 2 is shown, where the NRMS is employed above Array 1. Here, the period of  $T$  and the size of  $x1$  of the metal ring is 8 mm and 2.75 mm, respectively. The thickness of the substrate is 1.524 mm. The specific geometry and dimensions of the reference array in the design procedure are depicted in Figure 4b, including the overall structure of the reference array from the front side view and the structure of each layer from the top side view.



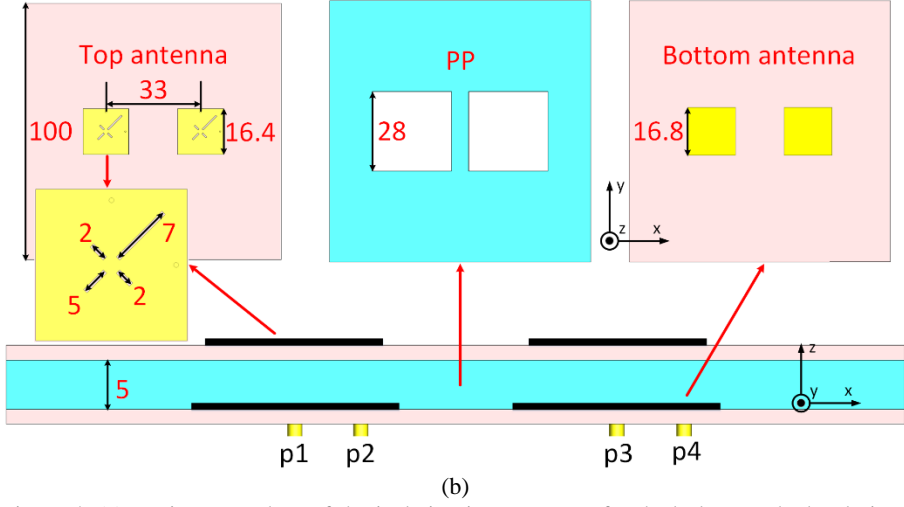
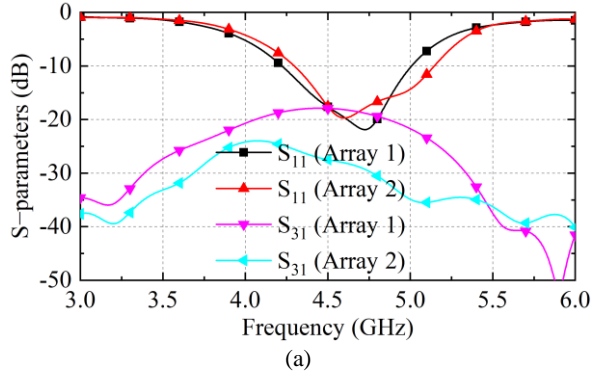


Figure 4. (a) Design procedure of the isolation improvement for dual-element dual-polarized an-tenna array with NRMS. Array 1 is the reference antenna array. In the next step, Array 2 is de-picted, where a metasurface consisting of periodic cross metal rings with a period  $T$  is employed above Array 1, where the air cavities with a period  $2 \times T$  are engraved on the metasurface. (b) The configuration of the reference array in the design procedure. (Unit: mm).

The  $S$  parameters of Array 1 and Array 2 are given in Figure 5. Port 1 and Port 2 work in  $y$ - and  $x$ -polarization, respectively. All  $S_{13}$  and  $S_{42}$  of the arrays with the pro-posed NRMS show low mutual coupling between the ports with the same polarization. Furthermore, Array 2 can provide a wider decoupling bandwidth.  $S_{14}$  and  $S_{23}$  of the array with NRMS present the mutual coupling between the ports with the cross-polarization. The simulated  $S$ -parameters also verify the theoretical analysis for the decoupling with the NRMS mentioned in the previous section. The optimized di-mensions of the NRMS and the high  $h$  are listed in Table 1.





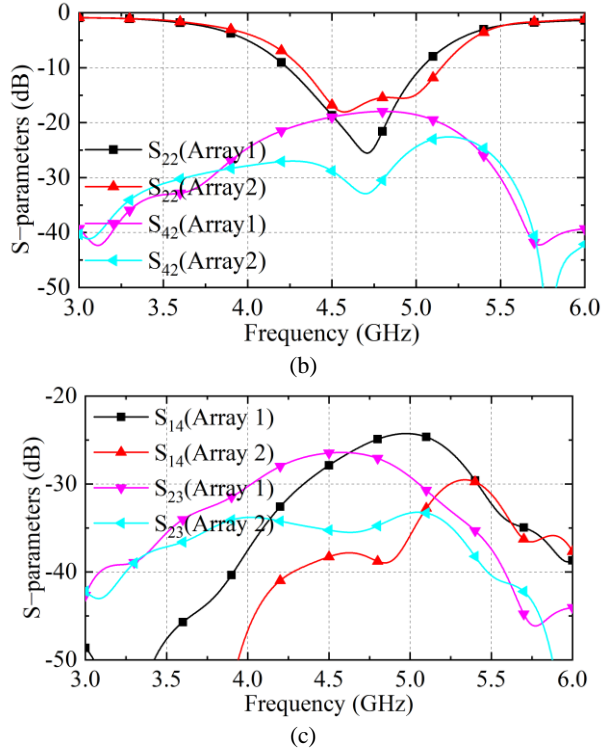


Figure 5. The S parameters of array1 and the one after adding MS and NRMS for array2 and ar-ray3, (a) the S11 and S31, (b) S22 and S42, and (c) S14 and S23.

From the decoupling study of the two-element antenna array with the proposed NRMS, it can be concluded that the proposed NRMS can be equivalent to a negative permeability and positive medium along the tangential direction of the antenna arrays. Therefore, the NRMS will suppress the propagation of the free-space coupling component along the tangential direction. The best decoupling level can be achieved by carefully designing the sizes of the NRMS element and the height of the NRMS above the antenna array.

Table 1. parameters of the NRMS.

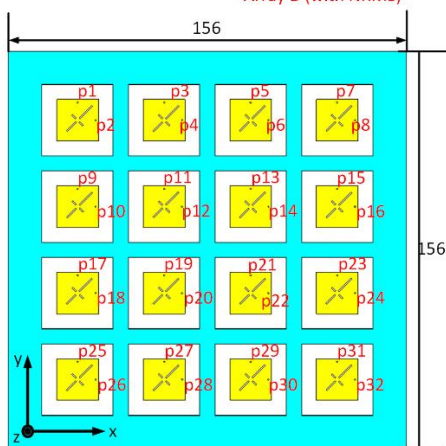
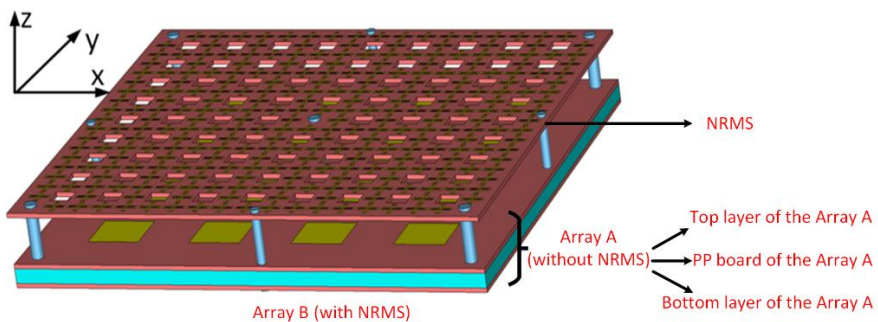
parameters	$x1$	$x2$	$x3$	$g$	$T$	$h$
Value(mm)	2.75	1.5	6.6	0.5	8	15

### III design Example of $4 \times 4$ Array with NRMS

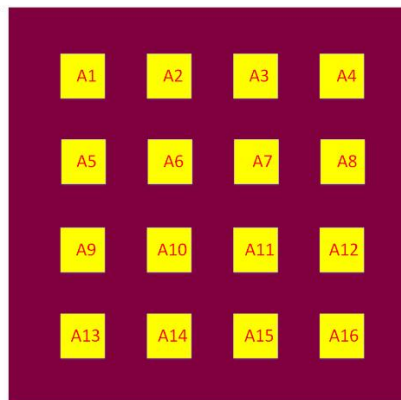
### 3.1 Antenna Configuration

Sometimes, the decoupling method that is effective to the two-element antenna array does not necessarily work for large-scale antenna arrays (e.g.,  $4 \times 4$  antenna array, even larger), where much more complicated coupling paths exist in large-scale antenna array. As a result, the proposed NRMS is also utilized to check its feasibility to improve the isolation of a wideband and large-scale antenna array. For brevity, a wideband and dual-polarized  $4 \times 4$  antenna array is investigated here.

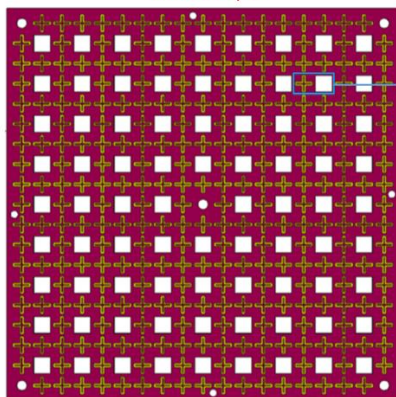
The antenna element and element dimension used in the stacked micro-strip antenna array in Section 2 are also applied to the  $4 \times 4$  arrays in this section. The proposed large-scale antenna array that consists of 16 elements with an inter-element distance  $d$  of 33 mm covers the bandwidth from 4.29 to 5.13 GHz. The micro coaxial cables are adopted to excite the antenna elements of the antenna array. Different from the dual-element antenna array in Figure 4, the mutual couplings of the  $4 \times 4$  phased arrays exist between the adjacent and non-adjacent elements in both co-polarization and cross-polarization. The mutual coupling between the array elements in the diagonal direction cannot be neglected either. The proposed NRMS, loaded above the antenna arrays with a height  $h$  of 15 mm, is expected to simultaneously reduce the mutual coupling of all the paths in a wideband. A design procedure of the NRMS is shown in Figure 6. Here, the original antenna array is labeled as Array A. The original array with the proposed NRMS is marked as Array B, where some non-metalized holes are drilled in both substrates, and a foam board is made with a thickness of 15 mm to support the NRMS. The simulated model of the  $4 \times 4$  antenna array with NRMS is depicted in Figure 6a, where the NRMS is placed above the original antenna array with a distance. The detailed structure of the original antenna array and the NRMS is depicted as well. The prototype is depicted in Figure 6b, where all foam boards and substrates are compressed into one piece and fixed by screws and bolts passing through the non-metalized holes.



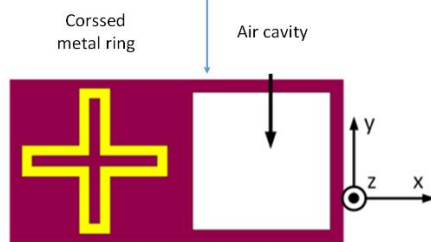
Bottom layer and PP board  
of the Array A



Top layer of the Array A



NRMS



(a)

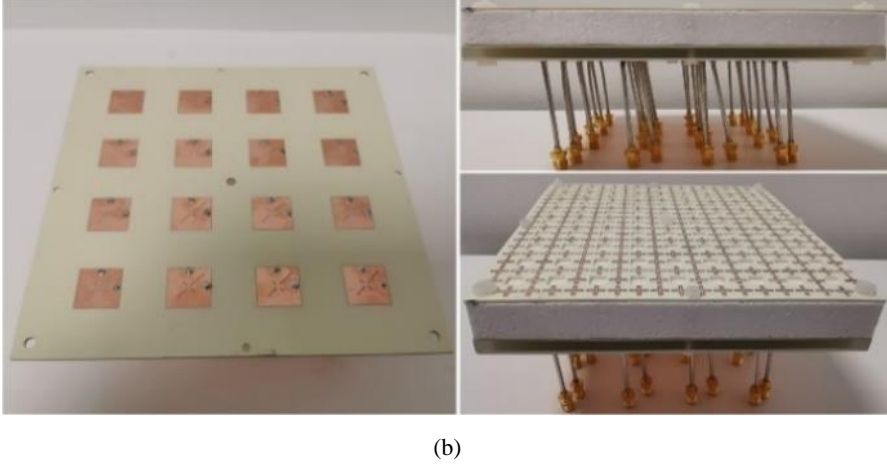


Figure 6. (a) the configuration of the original  $4 \times 4$  phased array with NRMS (Array B), (Unit: mm). (b) the fabricated prototype of the Array B with feeding cables.

### 3.2 Parametric Study

The height of the NRMS is an important parameter to determine the decoupling level of the array. Therefore, a parametric study for the height  $h$  is essential to obtain the optimal decoupling level for the  $4 \times 4$  large-scale antenna array. Figure 7 gives the S-parameters of the antenna array when  $h$  varies from 9 to 21 mm with a step of 3 mm. Here, the couplings between element A6 and the neighboring and non-neighboring elements are selected. It shows that, when  $h$  is 15 mm, the lowest couplings between antenna elements can be obtained, and the mutual couplings of the antenna array are lower than  $-24$  dB. As  $h$  is set as other values, the mutual couplings of the antenna array are higher than  $-24$  dB.

The size  $x_1$  of the metasurface cell (see Figure 1b) also plays an essential role in determining the decoupling level because the cross-shaped pattern of the NRMS unit cell fully determines the S-parameters and the corresponding extracted permittivity and permeability. Theoretically, the  $x_1$  and  $x_3$  determine bandwidth that we can extract negative permeability and positive permittivity. Thus, the parametric study for the size  $x_1$  and  $x_3$  for the decoupling level of the  $4 \times 4$  large-scale antenna array is provided. Figure 8 gives the S-parameters when size  $x_1$  varies from 1.25 to 2.75 mm with a step of 0.5 mm. It depicts that, for the increment of  $x_1$ , the mutual coupling of the  $4 \times 4$  large-scale antenna array decreases. When  $x_1$  is 2.75 mm, the mutual coupling of the  $4 \times 4$  large-scale antenna array reaches the lowest level, where the mutual coupling is lower than  $-24$  dB. When  $x_1$  increases further, the more

reflected waves from the proposed NRMS will be generated, which might enhance the space wave coupling of the array. Besides, the impedance between the proposed NRMS and antenna array will be deteriorated as well.

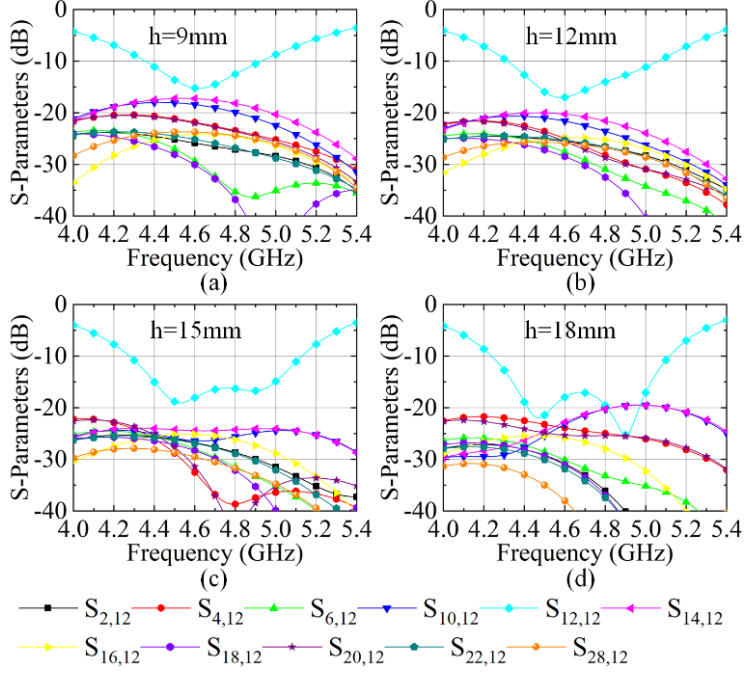


Figure 7. S-parameter of the antenna array loading with the proposed NRMS with different  $h$ , (a)  $h = 9$  mm, (b)  $h = 12$  mm, (c)  $h = 15$  mm, and (d)  $h = 18$  mm.

Figure 9 shows the S-parameters when size  $x_3$  varies from 0.6 to 6.6 mm with a step of 2 mm. It clearly demonstrates that, with the increment of  $x_3$ , the mutual coupling of the  $4 \times 4$  large-scale antenna array reduces slightly. When the air cavity size  $x_3$  of the NRMS unit cell is 6.6 mm, the lowest mutual coupling level of the antenna array can be achieved. When  $x_3$  increases further, the air cavity will destroy the structure of cross-shaped NRMS units. Thus, the S-parameters of the  $4 \times 4$  large-scale antenna array with larger air cavity size  $x_3$  (larger than 6.6 mm) are not given. Finally, the optimized  $x_1$  and  $x_3$  is 2.75 mm and 6.6 mm, respectively. Comparing the parametric study of  $x_1$  and  $x_3$  on the decoupling level of the  $4 \times 4$  large-scale antenna array, it could conclude that the size of the cross-shaped structure plays a determining role, and the size of the air cavity plays a fine-tuning function.

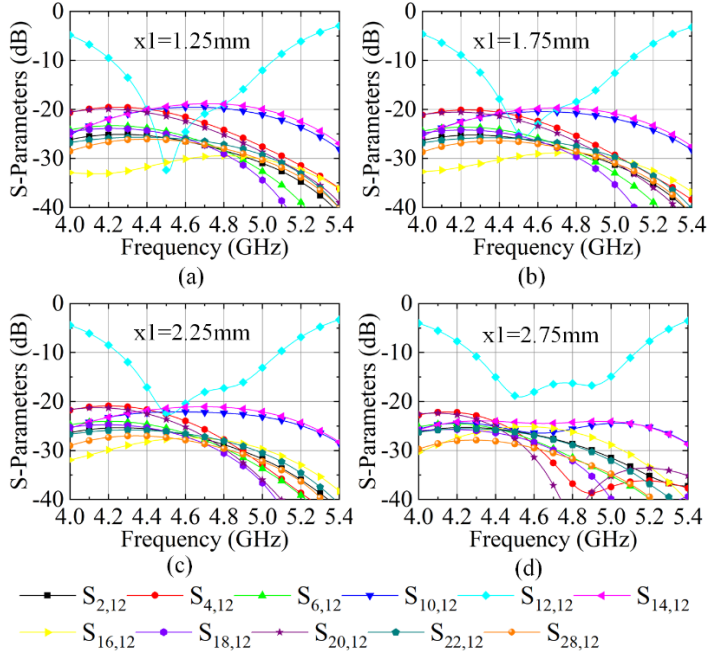


Figure 8. S-parameter of the antenna array loading with the proposed NRMS with different  $x_1$ , (a)  $x_1 = 1.25$  mm, (b)  $x_1 = 1.75$  mm, (c)  $x_1 = 2.25$  mm, (d)  $x_1 = 2.75$  mm.

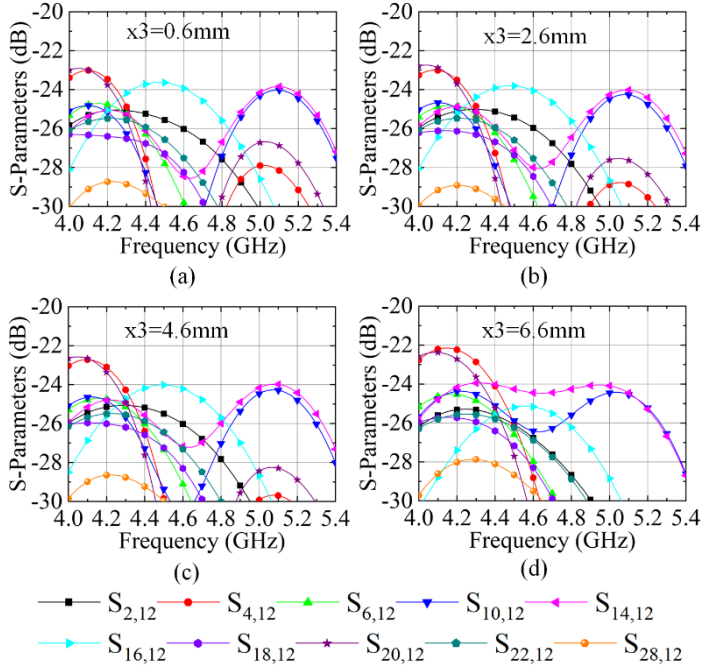
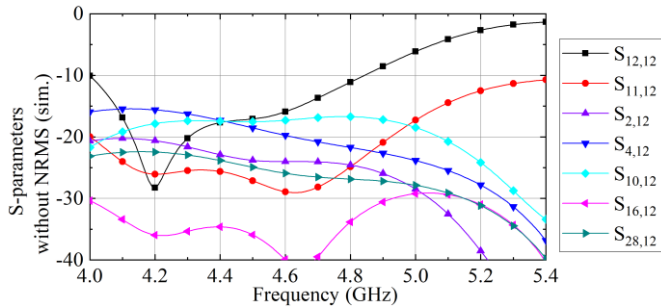


Figure 9. S-parameter of the antenna array loading with the proposed NRMS with different  $x_3$ , (a)  $x_3 = 0.6$  mm, (b)  $x_3 = 2.6$  mm, (c)  $x_3 = 4.6$  mm, (d)  $x_3 = 6.6$  mm.

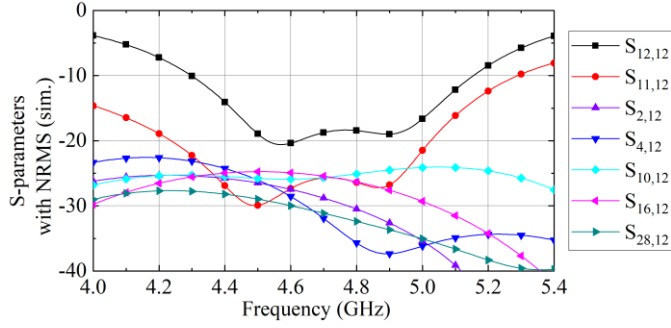
### 3.3 Antenna Array Performance

The  $4 \times 4$  arrays in Figure 6 have the mutual coupling between adjacent and non-adjacent array elements in the x, y, and diagonal directions. Moreover, the arrays are symmetric along the x, y, and diagonal directions. Due to the highly geometry symmetric of the NRMS and dual-polarized antenna array, the mutual coupling between the array element A6 (see Figure 6a) and other elements can represent all coupling types. Here, the S-parameters of A6 are selected and shown.  $S_{11,12}$  represents the mutual coupling level between port11 and port12 of the array element A6. It should be noticed that  $S_{2,12}$  refers to the mutual coupling between neighboring array elements in the diagonal direction.  $S_{4,12}$  and  $S_{10,12}$  represent the mutual couplings between adjacent elements in the y-direction and x-direction, respectively. In addition,  $S_{16,12}$  and  $S_{28,12}$  refer to the mutual coupling between non-neighboring array elements. The S-parameters of port11, similar to that of port12, can also represent the mutual coupling of the proposed  $4 \times 4$  large-scale antenna array.

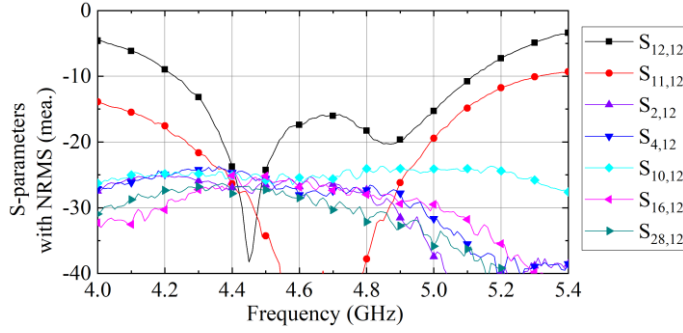
Figure10 gives the simulated and measured S-parameters of the  $4 \times 4$  antenna array with and without the proposed NRMS. In Figure 10a, the reference array covers from 4.05 to 4.91 GHz with an isolation of 16.5 dB. Figure 10b shows that the array with the proposed NRMS covers 4.36 to 4.94 GHz with an isolation of 24 dB. The measured S-parameters of the antenna array with the proposed NRMS in Figure 10c align well with the simulated one in Figure 10b. Therefore, all simulated and measured S-parameters demonstrate that the isolations of the wideband and dual-polarized large-scale antenna array can be improved effectively to over 24 dB by employing the proposed NRMS within 4.36 to 4.94 GHz.



(a)



(b)



(c)

Figure10. (a) S-parameters of arrays with and without NRMS, (a) the simulated S-parameters without NRMS, (b) the simulated S-parameters with NRMS, and (c) the measured S-parameters with NRMS.

The simulated and measured radiation patterns of the array before and after loading the proposed NRMS at 4.5 GHz, 4.7 GHz, and 4.9 GHz are shown in Figure 11 to check the impacts of the proposed NRMS on the radiation performance of the antenna element. The measurements are implemented in the anechoic chamber to avoid electromagnetic interference from the environment. As seen in Figure 11, the radiation patterns of the antenna arrays with and without the proposed NRMS are almost un-changed except for some slight ripples. Moreover, the cross-shaped metal rings convert partial space wave energy from one polarization into orthogonal polarization, which causes the deterioration of the cross-polarization level of the antenna elements. Additionally, the radiation patterns are asymmetric due to the propagation blockage of the space waves radiated from the active antenna by its adjacent antennas.



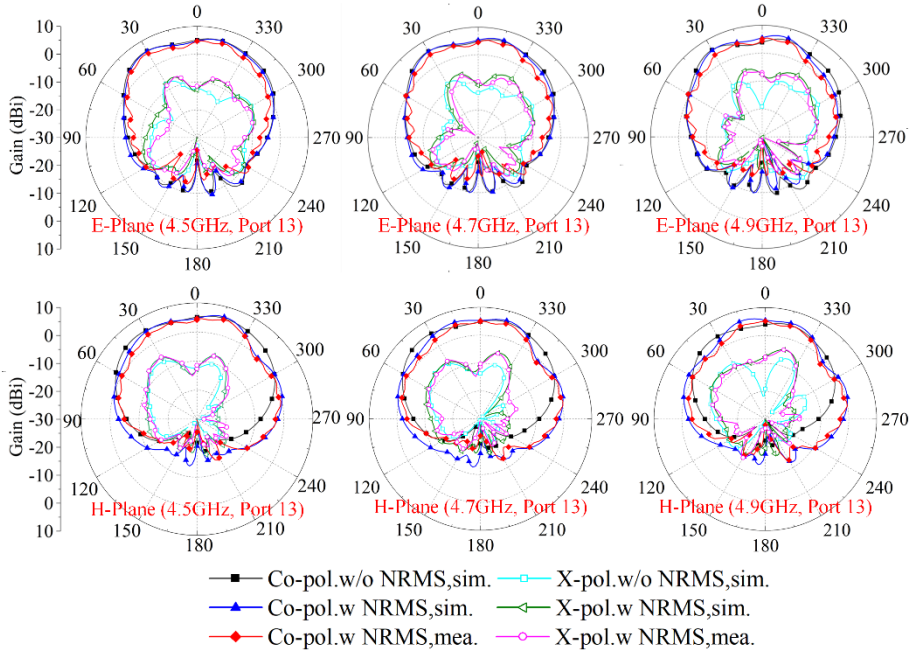


Figure 11. The radiation patterns of the array with and without NRMS at different frequencies.

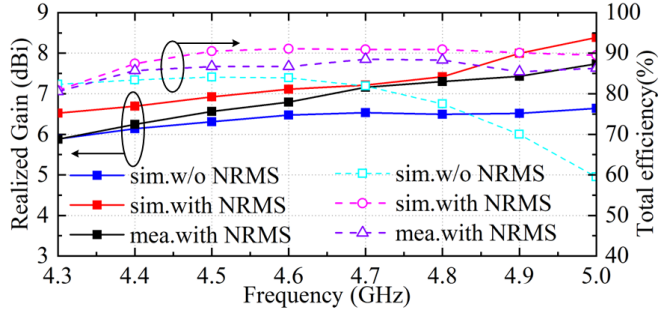


Figure 12. The total efficiency and the realized gain of the proposed antenna array.

Finally, the realized gains and total efficiencies of the antenna array with and without the proposed NRMS are presented in Figure 12. The simulated results illustrate that the proposed NRMS can improve the realized gain and total efficiency of the antenna array within a wide bandwidth, which are attributed to the suppressed propagation of the space waves coupling along the tangential direction. Moreover, the measured realized gain and total efficiency of the array with the proposed NRMS are lower than the simulated results caused by the measurement error. The losses in coaxial cables also

cause the discrepancies between the simulation and the measurement of the antenna arrays. Here, the measured realized gain and total efficiency are more than 6 dBi and 74% from 4.36 to 4.94 GHz, respectively.

### 3.4 Antenna Performance Comparison

Table 2. Performance comparison of the proposed antenna arrays with other state-of-the-art similar works.

Ref.	Decoupling Method	Pol. And Scale	Freq. (GHz)	Worst Iso. (dB)	Gain (dBi)	Total Efficiency	Antenna Distance and Height ( $\lambda_0$ )	Feasib. for Massive MIMO Arrays	Complexity
[24]	Decoupling network	Dual-pol. $4 \times 4$	4.85–4.95 (2.0%)	25	5.3	>70%	$0.50\lambda_0$ , $0.274\lambda_0$	Yes	High
[26]	ADS	Dual-pol. $4 \times 4$	3.3–3.8 (14.1%)	25	6.0	--	$0.64\lambda_0$ , $0.4\lambda_0$	Yes	High
[28]	DG	Dual-pol. $4 \times 4$	4.9–5.2 (6.1%)	25	7.3	>90%	$0.62\lambda_0$ , $0.25\lambda_0$	Yes	High
[29]	Metasurface	Single-pol. $2 \times 1$	5.49–6.0 (8.64%)	27	5.0	>63%	$0.259\lambda_0$ , $0.180\lambda_0$	No	Low
[31]	Metasurface	Single-pol. $4 \times 4$	5.67–5.97 (5.17%)	19	5.0	>70%	$0.43\lambda_0$ , $0.19\lambda_0$	Yes	Low
<b>This work</b>	<b>NRMS</b>	<b>Dual-pol. <math>4 \times 4</math></b>	<b>4.36–4.94 (12.5%)</b>	<b>24</b>	<b>6.0</b>	<b>&gt;74%</b>	<b><math>0.5\lambda_0</math>, <math>0.38\lambda_0</math></b>	<b>Yes</b>	<b>Low</b>

Ref.: reference; Pol.: polarized; Freq.: frequency; Iso.: isolation; Feasib.: feasibility; Compl.: complexity.

The performance of the proposed  $4 \times 4$  large-scale antenna array with the proposed NRMS is compared with the literature reported recently, as listed in Table 2. The decoupling proposed in [24] is an effective method, but it has a fatal defect of a narrow bandwidth caused by the resonant–response property of the decoupling network. Typically, it needs to be deployed on the backside of the antenna array, where the antenna array with the decoupling network

has multiple substrates, which means they are bulky and complicated. Moreover, the decoupling network usually lowers gain and total efficiency of antenna array. The ADS in [26] is a novel decoupling concept, but it has a complicated design process for the pattern of the primary reflectors and second-ary reflectors. Additionally, it needs a relatively larger space to accommodate the re-flectors to reflect enough space waves so that the unwanted coupling waves can be largely eliminated, which is not conducive to antenna miniaturization. Though the gain and total efficiency of the array in [28] are higher than that of our work, it has a larger inter-element distance and a bulky structure. The metasurfaces proposed in [29,31] have a relatively small inter-element distance, but they can only be used in single-polarized arrays because of the magnetic resonant response and the asymmetry along the cross direction. Moreover, the bandwidth, gain, and total efficiency of the arrays in [29,31] are worse than our work. Additionally, the worst isolation of the array in [31] is higher than our work, but it cannot be expanded to a massive MIMO array application owing to the limitation of asymmetrical structure along the orthogonal directions. Compared with the structure in the current literature, on the premise of guaranteeing a wider working bandwidth, higher worst isolation, gain, and efficiency, our work has a simple design and installation process of the decoupling scheme.

## IV Conclusion

A novel decoupling concept of NRMS for wideband and dual-polarized large-scale antenna arrays is proposed. The decoupling mechanism of the NRMS has been analyzed. To justify the feasibility of the proposed NRMS for decoupling of large-scale antenna arrays, a  $4 \times 4$  antenna array loading with the proposed NRMS has been simulated, fabricated, and measured. The simulated and measured results demonstrate that the isolations of the antenna array can be enhanced from 16.5 dB to over 24 dB within the band from 4.36 to 4.94 GHz, almost without introducing any other adverse effect on the performance of the overall antenna array. The comparison between the proposed NRMS and other techniques reported in the latest literature shows a great potential of the proposed NRMS to be applied to massive MIMO antenna arrays with low mutual couplings in the sub-6 GHz band.

**Author Contributions:** Conceptualization, S. L, P. M and S. Z; methodology, S. L and P. M; software, S. L; validation, S. L; formal analysis, S. L and P. M; investigation, G. F. P and S. Z; resources, G. F. P and S. Z; data curation, S. L; writing—original draft preparation, S.L; writing—review and editing, P. M

and Y. M. Z; visualization, S. L; supervision, P. M and S. Z; project administration, G. F. P. and S. Z; funding acquisition, G. F. P and S. Z. All authors have read and agreed to the published version of the manuscript.

**Funding:** This work was partially supported by the Innovationsfonden Project of MARS2.

**Institutional Review Board Statement:** Not Applicable.

**Informed Consent Statement:** Not Applicable.

**Data Availability Statement:** Not Applicable.

**Conflicts of Interest:** The authors declare no conflict of interest.

## Reference

- [1] Face, K.; Lee, J.; Jung, Y. High-Gain millimeter-wave patch array antenna for unmanned aerial vehicle application. *Sensors* 2021, 21, 3914. <https://doi.org/10.3390/s21113914>.
- [2] de Figueiredo, F.A.P.; Dias, C.F.; Lima, E.R.; Fraidenraich, G. Capacity bounds for dense massive MIMO in a line-of-sight propagation environment. *Sensors* 2020, 20, 520. <https://doi.org/10.3390/s20020520>.
- [3] Zou, W.; Qu, S.; Yang, S. Wideband wide-scanning phased array in triangular lattice with electromagnetic bandgap structures. *IEEE Antennas Wirel. Propag. Lett.* 2019, 18, 422–426.
- [4] Wang, B.; Lin, X.; Nie, L.; Yu, D. A broadband wide-scanning planar phased array antenna with equivalent circuit analysis. *IEEE Antennas Wirel. Propag. Lett.* 2020, 19, 2154–2158.
- [5] Cheng, Y.; Feng, J.; Liao, C.; Ding, X. Analysis and design of wideband low-rsc wide-scan phased array with AMC ground. *IEEE Antennas Wirel. Propag. Lett.* 2021, 20, 209–213.
- [6] Zhai, H.; Xi, L.; Zang, Y.; Li, L. A low-profile dual-polarized high-isolation MIMO antenna arrays for wideband base-station applications. *IEEE Trans. Antennas Propag.* 2018, 66, 191–202.
- [7] Mirmozafari, M.; Saeedi, S.; Zhang, G.; Samii, Y.R. A crossed dipole phased array antenna architecture with enhanced polarization and

- p isolation characteristics.
- IEEE Trans. Antennas Propag.*
- 2020, 68, 4469–4478.
- [8] Li, Y.; Sim, C.; Luo, Y.; Yang, G. High-isolation 3.5 GHz eight-antenna MIMO array using balanced open-slot antenna element for 5G smartphones. *IEEE Trans. Antennas Propag.* 2019, 67, 3820–3830.
  - [9] Chen, X.; Zhang, S.; Li, Q. A review of mutual coupling in MIMO systems. *IEEE Access* 2018, 6, 24706–24719.
  - [10] Janaswamy, R. Effect of element mutual coupling on the capacity of fixed length linear arrays. *IEEE Antennas Wireless Propag. Lett.* 2002, 1, 157–160.
  - [11] Schmid, C.M.; Schuster, S.; Feger, R.; Stelzer, A. On the effects of calibration errors and mutual coupling on the beam pattern of an antenna array. *IEEE Trans. Antennas Propag.* 2013, 61, 4063–4072.
  - [12] Wang, B.; Chang, Y.; Sun, Y. Performance of the large-scale adaptive array antennas in the presence of mutual coupling. *IEEE Trans. Antennas Propag.* 2016, 64, 2236–2245.
  - [13] Song, H.J.; Bekaryan, A.; Schaffner, J.H.; Hussain, A.; Kildal, P. Effects of mutual coupling on LTE MIMO capacity for monopole array: Comparing reverberation chamber tests and drive tests. *IEEE Antennas Wirel. Propag. Lett.* 2015, 14, 454–457.
  - [14] Jin, F.; Ding, X.; Cheng, Y.; Wang, B.; Shao, W. A wideband phased array with broad scanning range and wide-angle impedance matching. *IEEE Trans. Antennas Propag.* 2020, 68, 6022–6031.
  - [15] Chen, X.; Zhang, S.; Li, Q. A review of mutual coupling in MIMO systems. *IEEE Access* 2018, 6, 24706–24719.
  - [16] Islam, H.; Das, S.; Ali, T.; Kumar, P. Split ring resonator-based bandstop filter for improving isolation in compact MIMO antenna. *Sensors* 2021, 21, 2256. <https://doi.org/10.3390/s21072256>.
  - [17] Qian, B.; Chen, X.; Kishk, A.A. Decoupling of microstrip antennas with defected ground structure using the common/differential mode theory. *IEEE Antennas Wirel. Propag. Lett.* 2021, 20, 828–832.
  - [18] Abbas, A.; Hussain, N.; Sufian, D.A.; Jung, J.; Park, S.M.; Kim, N. Isolation and gain improvement of a rectangular notch UWB-MIMO antenna. *Sensors* 2022, 22, 1460. <https://doi.org/10.3390/s22041460>.

- [19] Li, M.; Jiang, L.; Yeung, K.L. A general and systematic method to design neutralization lines for isolation enhancement in MIMO antenna arrays. *IEEE Trans. Veh. Tech.* 2020, 69, 6242–6253.
- [20] Lau, B.K.; Andersen, J.B. Simple and efficient decoupling of compact arrays with parasitic scatterers. *IEEE Trans. Antennas Propag.* 2012, 60, 464–472.
- [21] Li, M.; Cheung, S. A novel calculation-based parasitic decoupling technique for increasing isolation in multiple-element MIMO antenna arrays. *IEEE Trans. Veh. Technol.* 2021, 70, 446–458.
- [22] Cheng, Y.-F.; Cheng, K.-K.M. A novel dual-band decoupling and matching technique for asymmetric antenna arrays. *IEEE Trans. Microw. Theory Tech.* 2018, 6, 2080–2089.
- [23] Xia, R.-L.; Qu, S.-W.; Li, P.-F.; Yang, D.-Q.; Yang, S.; Nie, Z.-P. Wide-angle scanning antenna array using an efficient decoupling network. *IEEE Trans. Antennas Prop.* 2015, 63, 5161–5165.
- [24] Zhang, Y.-M.; Zhang, S.; Li, J.-L.; Pedersen, G.F. A transmission-line-based decoupling method for MIMO antenna arrays. *IEEE Trans. Antennas Prop.* 2019, 67, 3117–3131.
- [25] Wu, K.-L.; Wei, C.; Mei, X.; Zhang, Z.-Y. Array-antenna decoupling surface. *IEEE Trans. Antennas Prop.* 2017, 65, 6728–6738.
- [26] Wei, C.; Zhang, Z.; Wu, K. Phase compensation for decoupling of large-scale staggered dual-polarized dipole array antennas. *IEEE Trans. Anten. Prop.* 2020, 68, 2822–2831.
- [27] Mei, P.; Zhang, Y.; Zhang, S. Decoupling of a wideband dual-polarized large-scale antenna array with dielectric stubs. *IEEE Trans. Veh. Tec.* 2021, 70, 7363–7374.
- [28] Zhang, S.; Chen, X.; Pedersen, G.F. Mutual coupling suppression with decoupling ground for massive MIMO antenna arrays. *IEEE Trans. Veh. Technol.* 2019, 68, 7273–7282.
- [29] Wang, Z.; Zhao, L.Y.; Cai, Y.; Zheng, S.; Yin, Y. A meta-surface antenna array decoupling (MAAD) method for mutual coupling reduction in a MIMO antenna system. *Sci. Rep.* 2018, 8, 3152.

- [30] Liu, F.; Guo, J.; Zhao, L.; Shen, X.; Yin, Y. A meta-surface decoupling method for two linear polarized antenna array in sub-6 GHz base station applications. *IEEE Access* 2018, 7, 2759–2768.
- [31] Tang, J.; Faraz, F.; Chen, X.; Zhang, Q.; Li, Q.; Li, Y.; Zhang, S. A metasurface superstrate for mutual coupling reduction of large antenna arrays. *IEEE Access* 2020, 8, 126859–126867.

# Paper B

Mutual Decoupling for Massive MIMO Antenna Arrays by  
Using Triple-Layer Meta-Surface

Shenyuan Luo, Yiming Zhang, Gert Frølund Pedersen, and  
Shuai Zhang

This paper has been published at the  
IEEE Open Journal of Antennas and Propagation, vol. 3, pp. 1079-1089,  
2022.





## Abstract

***Abstract—The high isolation massive antenna arrays are the key devices in the base station of the future wireless communication systems. The challenge for the array application is how to reduce the coupling among the array elements. This paper introduces a new decoupling method for massive MIMO arrays with an inner-element distance of around half wavelength by using a triple-layer metasurface (TMS). The TMS comprises three identical surfaces. The waves reflected from the bottom metasurface (MS) and top two-layer MS have the same amplitudes and the opposite phases, which are canceled with each other. An example of 4×4 dual-polarized wideband microstrip array with a TMS is proposed to verify the decoupling method. The simulation and measurement show that the TMS can help reduce the coupling among the array elements to less than -24 dB in both the co-polarization and cross-polarization directions within 4.23-4.82 GHz. In the meanwhile, the radiation characteristics of the arrays with and without TMS are almost unchanged.***

## I Introduction

The future wireless communication technology boosts the development of wireless communication [1]. The multiple-input multiple-output (MIMO) has attracted much attention in recent years because it can significantly improve the data throughput and transmission distance without increasing its bandwidth or the total transmit power [2-3]. The massive MIMO system, scales up from the MIMO system, has a higher transmission ratio, spectrum efficiency, and channel capacity [4-5]. When a massive MIMO array with an inner-element distance around half wavelength is implemented, the mutual coupling is inevitable[6]. Recently, researchers found that the coupling of the arrays, basically consists of space wave coupling component, seriously deteriorate the antenna performance [7-17]. Thus, low coupling of the massive MIMO array has become a crucial indicator during the implement.

Numerous decoupling techniques for MIMO arrays have been observed: mutual decoupling network [18], defected ground structure [19], electromagnetic bandgap [20], metamaterial [21], and parasitic decoupling technique [22]. In addition, the metasurface (MS) as an effective decoupling technology for arrays has been studied and reported in [23-24]. In [23], a suspended MS is placed above the array, where the surface is equivalent to a negative permeability medium to reject the propagation of the waves. However, it cannot be applied in dual-polarized antenna arrays because of its

asymmetry. In [24], a novel MS employs a near-field resonator (NFR) above each antenna element. However, it is not available to be scaled up to dual-polarized arrays because it will increase the coupling in the orthogonal modes.

Many decoupling methods for the massive MIMO arrays have been reported [25-30]. A non-resonant metasurface (NMS) with a was proposed in [25] to suppress the propagation of the space waves. Here, a negative permeability and positive permittivity along the tangential direction of the array can be abstracted. A transmission-line-based decoupling method was proposed in [26], which enables well-cancels coupling for the adjacent elements but slightly drops the total efficiencies. Moreover, its relative working band is pretty narrow. [27] introduced a decoupling ground (DG), which changes the ground current path to enable well-cancel with the space wave coupling. Yet, it needs a relatively sizeable inner-element distance to adjust the shape of the ground plane. A concept of array-antenna decoupling surface (ADS) for massive MIMO arrays was proposed [28]. But the arrays with ADS elements have complicated design procedure and relatively larger size. Additionally, a decoupling method of phase compensation based on the concept of ADS for large-scale staggered dual-polarized dipole arrays is further investigated to simultaneously reduce the couplings between adjacent co-polarized array elements with diversified phase laggings [29]. Yet, it has the same problem with the method mentioned in [28]. A new method of decoupling dielectric stubs (DDS) is proposed as perturbations to constrain the electromagnetic fields of the array element [30]. However, dielectric stubs with low permittivity are needed to reduce transmission loss.

In this paper, a triple-layer metasurface (TMS) concept is proposed and experimentally demonstrated. The TMS is composed of three identical MSs and placed above the arrays. Here, the waves reflected from the bottom layer MS and the top two-layer MS have same amplitudes and opposite phases to enable perfect cancellation. Consequently, the coupling of the arrays can be significantly reduced by utilizing the proposed TMS. A factual example of a 4×4 massive array is studied to verify the proposed decoupling method. The proposed TMS for massive MIMO arrays has some novelties as:

1. The coupling of the massive MIMO arrays with the inner-element distance of around half wavelength mainly results from the space waves coupling component. For this, the method TMS develops two paths for the space waves coupling component, which has a phase difference of  $180^\circ$  and an amplitude difference of 0 to obtain well cancellation.

2. The proposed TMS features symmetry in orthogonal directions that can

be utilized in dual-polarized arrays. At the same time, it has a stable radiation performance over the wide working band of the arrays.

3. The arrays with the TMS have a low loss. Moreover, it can be implemented easily by adjusting the radius of the TMS element and the thickness of the air gaps between TMS.

This paper is organized as follows: in Section II, the concept of the TMS method is carefully described, and then a TMS unit is designed and analyzed. The decoupling method TMS for massive MIMO array is applied in section III. First, a dual-polarized and wideband microstrip array is proposed. Then, the TMS is placed above the reference array. Finally, the simulated and measured results are presented to verify the proposed decoupling method. Section IV concludes the paper.

## II Proposed Decoupling Technique

### A. Concept of the proposed TMS mutual decoupling method

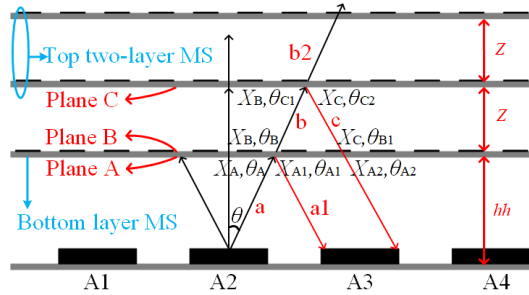


Fig. 1. The decoupling schematics of the TMS.

Fig. 1 gives the theoretical analysis of the decoupling mechanism of the TMS for the massive MIMO arrays. When the TMS is suspended above the array, the waves reflected from the bottom layer MS and the top two-layer MS have the same amplitudes and opposite phase, which can be cancelled by appropriately adjusting the size of the TMS. Therefore, a suppression for the space coupling can be obtained. As shown in Fig. 1, the bottom surface and the top surface of the bottom layer MS are defined as Plane A and Plane B, respectively. The phase of the space coupling component  $a$  on plane A is marked as  $\theta_A$ . In the meanwhile, the phase of the reflection component  $a1$  on plane A can be expressed as:

$$\theta_{A1} = \theta_A + \theta_{\text{refl}} \quad (1)$$

where the  $\theta_{\text{ref1}}$  is the phase of the reflection coefficient of the bottom layer MS. When the waves propagate through the bottom MS, it will introduce a transmitted phase delay  $\theta_{\text{tra1}}$ . The phase of the transmitted wave  $b$  on Plane B can be calculated as:

$$\theta_B = \theta_A + \theta_{\text{tra1}} \quad (2)$$

When the transmitted component  $b$  propagates to plane C, it will have a phase delay that can be expressed as:

$$\theta_{\text{delay}} = (Z / \lambda) \times 360^\circ \quad (3)$$

The phase  $\theta_{C1}$  of the waves on plane C can be calculated as:

$$\theta_{C1} = \theta_A + \theta_{\text{tra1}} + \theta_{\text{delay}} \quad (4)$$

The phase of the reflected waves on plane C can be calculated as:

$$\theta_{C2} = \theta_{C1} + \theta_{\text{ref2}} \quad (5)$$

$$\theta_{C2} = \theta_A + \theta_{\text{tra1}} + \theta_{\text{delay}} + \theta_{\text{ref2}} \quad (6)$$

Here, the  $\theta_{\text{ref2}}$  represents the phase of the simulated  $S_{11}$  of the top two-layer MS. When the waves reflect from Plane C propagate to the bottom layer MS, there will be a phase delay  $\theta_{\text{delay}}$  too. Therefore, the phase of the reflected waves on plane B can be expressed as:

$$\theta_{B1} = \theta_{C2} + \theta_{\text{delay}} \quad (7)$$

$$\theta_{C1} = \theta_A + \theta_{\text{tra1}} + \theta_{\text{delay}} \times 2 + \theta_{\text{ref2}} \quad (8)$$

Furthermore, the phase of the waves on plane A reflected from plane C can be calculated as:

$$\theta_{A2} = \theta_A + \theta_{\text{tra1}} \times 2 + \theta_{\text{delay}} \times 2 + \theta_{\text{ref2}} \quad (9)$$

Since the waves reflected from plane A and plane C have the same amplitudes and the opposite phase. Therefore the  $\theta_{A2}$  can also be expressed as:

$$\theta_{A2} = \theta_{A1} + 180^\circ \quad (10)$$

$$180^\circ = \theta_{\text{tra1}} \times 2 + \theta_{\text{delay}} \times 2 + \theta_{\text{ref2}} \quad (11)$$

$$\theta_{\text{delay}} = (180^\circ - \theta_{\text{tra1}} \times 2 - \theta_{\text{ref2}}) / 2 \quad (12)$$

The thickness of the air gap  $Z$  between the MSs can be calculated as:

$$Z = \left( \left( (180^\circ - \theta_{\text{tra1}} \times 2 - \theta_{\text{ref2}}) / 2 \right) / 360 \right) \times \lambda \quad (13)$$

The phase difference  $\theta_{\text{dif}}$  between  $\theta_{A1}$  and  $\theta_{A2}$  can be expressed as:

$$\theta_{\text{dif}} = \theta_{\text{tra1}} \times 2 + \theta_{\text{delay}} \times 2 + \theta_{\text{ref2}} - \theta_{\text{ref1}} \quad (14)$$

Regarding for the amplitudes, the amplitudes of the reflection coefficient and the transmission coefficient of the bottom layer MS can be defined as:  $R_l$  and  $T_l$ , respectively. Meanwhile, the amplitude of the reflection coefficient of the top two-layer MS can be marked as:  $R_2$ . When the amplitude of the coupling component is  $X_A$ , the amplitude of the waves reflected from the

bottom layer MS is  $X_{A1}$ , and the amplitude of the transmitted waves from the bottom layer MS is  $X_B$ . And then, the amplitude of the waves reflected from the top two-layer MS on plane C is  $X_C$ , while the amplitude of the waves reflected from the top two-layer MS on Plane A is  $X_{A2}$ .

$$X_{A1} = X_A \cdot R_1 \quad (15)$$

$$X_B = X_A \cdot T_1 \quad (16)$$

$$X_C = X_B \cdot R_2 \quad (17)$$

$$X_C = X_A \cdot T_1 \cdot R_2 \quad (18)$$

$$X_{A2} = X_C \cdot T_1 \quad (19)$$

$$X_{A2} = X_A \cdot T_1^2 \cdot R_2 \quad (20)$$

The Amplitude difference between the waves reflected from the bottom layer MS and the one reflected from the top two-layer MS on plane A can be calculated as:

$$X_{\text{dif}} = X_{A1} - X_{A2} \quad (21)$$

$$X_{\text{dif}} = X_A \cdot (R_1 - T_1^2 \cdot R_2) \quad (22)$$

According to the analysis for the decoupling mechanism of TMS, the amplitude calculated difference equal to 0 from the formula (22).

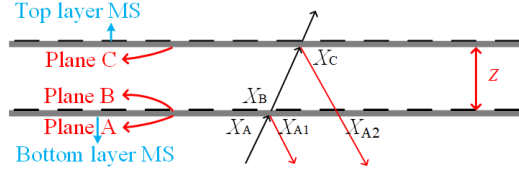


Fig. 2. The phase distribution of the space waves on two-layer MS.

In addition, it is needed to analyze why the two-layer MS cannot be used to reduce the coupling of the arrays, where the two MSs has same dimensions. Resemble to Fig.1, a two-layer MS placed above the reference array with corresponding phase distribution is shown in Fig.2. The amplitude of waves reflected from the top layer MS on plane C can be presented as:

$$X_C = X_A \cdot T_1 \cdot R_2 \quad (23)$$

Furthermore, the wave reflected from the top layer MS on plane A can be expressed as:

$$X_{A2} = X_A \cdot T_1^2 \cdot R_2 \quad (24)$$

Therefore, the amplitude of the two kinds reflected waves can be calculated as:

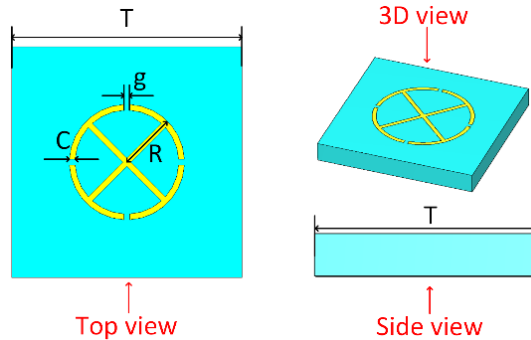
$$X_{\text{dif}} = X_A \cdot (R_1 - T_1^2 \cdot R_2) \quad (25)$$

The calculated results repeats that the amplitude difference does not equal to 0, which demonstrate that the two-layer MS cannot be used to

suppress the coupling of the arrays. Therefore, A TMS is adopted to reduce the mutual coupling of the massive MIMO antenna arrays.

### B. Design of the TMS

The periodic unit with a feature of symmetry along x-axis and y-axis is designed to meet the requirement for the decoupling of the wideband and dual-polarization massive MIMO arrays. A circular and cross-shaped patches are integrated into the same MS unit with four splits in the x-direction and the y-direction. The metal patch of the MS element is printed on a Rogers RO4350B substrate with a thickness of 1.52mm, a relative permittivity of 3.66 and a loss tangent of 0.0037. The bottom layer MS element is depicted in Fig. 3 (a) from the top view, front view, and perspective view, respectively. Here,  $T=8$  mm,  $C=0.2$  mm,  $g=0.2$  mm,  $R=2$  mm. A comprise scheme of a triple-layer metasurface (TMS) is adopted to avoid the problem of high profile of the array. For the factual massive MIMO arrays, the space coupling component is radiated to the MS with an incident angle  $\theta$  along the normal direction of the arrays. Therefore, the transmission coefficient and the phase of the S-parameters with various incident angles of  $\theta$  are studied and shown in Fig. 3. Fig. 3 (b) and Fig. 3 (c) show that when the  $\theta$  varies from  $0^\circ$  to  $60^\circ$  with a step of  $20^\circ$ , the transmission loss of the bottom layer MS increases, yet still show a high transmission performance over the operating band. Fig. 3 (d) and Fig. 3 (e) depict that the phase of the S11 and S21 slightly increases as the  $\theta$  varies from  $0^\circ$  to  $60^\circ$ . Moreover, when the  $\theta$  is  $0^\circ$ , the phase of the S11 and S21 is  $-115^\circ$  and  $-30^\circ$ , respectively. Fig. 3 also repeats that the bottom layer MS exhibits a stable transmission and reflection characteristic within a wide working band.



(a)

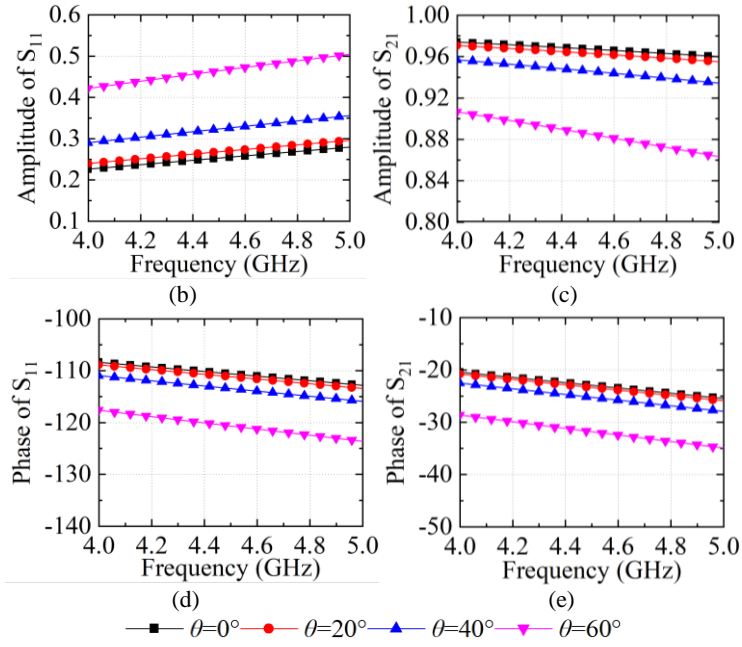


Fig. 3. Detail structure, the amplitudes, and the phases of the S-Parameters of the bottom layer MS with different incident angle  $\theta$ : (a) the bottom-layer MS, (b) the amplitude of the  $S_{11}$ , (c) the amplitude of the  $S_{21}$ , (d) the phase of the  $S_{11}$ , (e) the phase of the  $S_{21}$ .

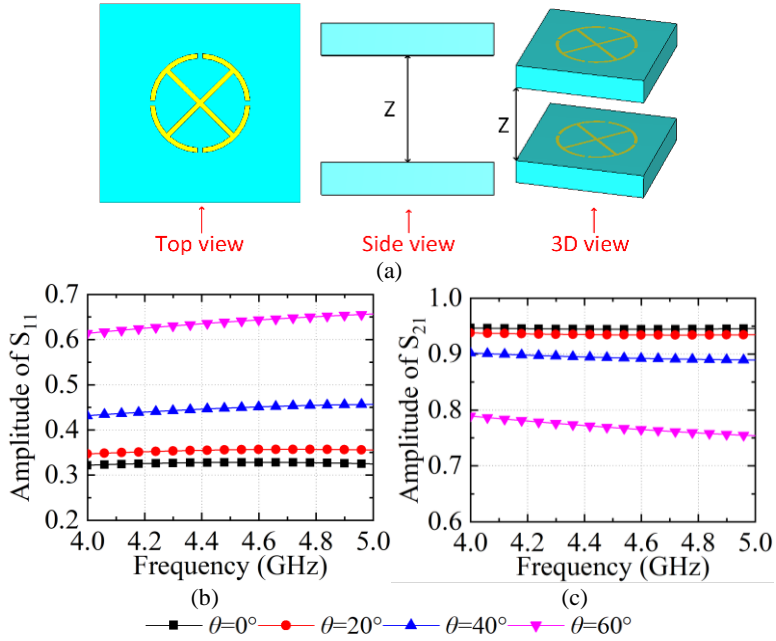




Fig. 4. Detail structure of the top two-layer MS, the amplitudes, and the phases of the S-Parameters of the top two-layer MS with different incident angle  $\theta$ : (a) the top two-layer MS, (b) the amplitude of the  $S_{11}$ , (c) the phase of the  $S_{11}$ .

Fig. 4 shows the two-layer MS structure from front, top, the perspective views, and the corresponding S-parameters. The top two-layer MS has the same sizes as the bottom layer MS. Fig. 4 (a) shows the detailed structure of the two-layer MS. Fig. 4 (b) depicts that with the increase of the  $\theta$ , the reflection increases too, but the transmission decreases. Fig. 4 (c) demonstrates that the phase of the S-parameters of the two-layer MS almost has no change with different  $\theta$ .

Based on the theoretical analysis of the decoupling mechanism of TMS for the massive MIMO arrays (see in Fig.1), the amplitude difference and the phase difference between the waves reflected from the bottom layer MS and top two-layer MS are calculated and given in Fig. 5 by varying the incident angle of  $\theta$  from  $0^\circ$  to  $60^\circ$  with the step of  $20^\circ$ . The calculated results demonstrate that the amplitude and phase differences between the waves reflected from the bottom layer MS and top two-layer MS basically equal to 0 and  $180^\circ$ , respectively. The calculated results justify that these two kinds of waves can be canceled with each other.

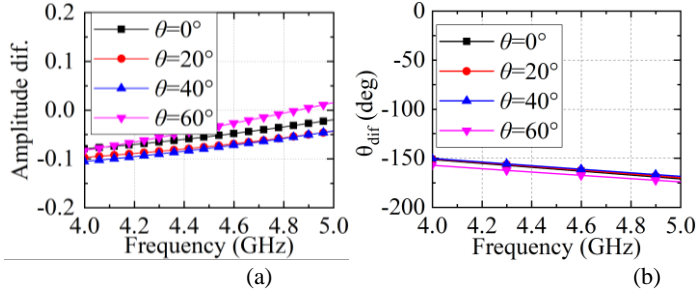


Fig. 5. The calculated amplitude difference  $A_{dif}$  and phase difference  $\theta_{dif}$  between the waves reflected from the bottom-layer MS the top two-layer MS when the incident angle of  $\theta$  varies from  $0^\circ$  to  $60^\circ$  with the step of  $20^\circ$ : (a) amplitude difference, (b) phase difference.

According to the simulated results and the analysis of the decoupling method of the TMS, the waves reflected from the bottom two-layer MS and the top layer MS are out of phase and can be canceled with each other too. The redundant description will not be done due to the limitation of the page.

### C. Simulations for the Verification of the Proposed Decoupling Method

In this subsection, we take a dual-polarization two-element array shown in Fig. 6 as an example to study the decoupling mechanism of the TMS. The detailed dimensions of the array are shown in the figures as well. The

wideband dual-polarization array is composed of two layers of patch antennas. The top antenna is placed above the bottom one and supported by a PP (polypropylene) board with a dielectric constant of 2.2. The two patch antenna elements are printed on a Rogers RO4350B substrate with a relative permittivity of 3.66 and a loss tangent of 0.0037. The bottom patch antenna consists of two substrates with the same thickness of 0.762 mm, and the thickness of the substrate of the top antenna is 1.524 mm. The array is fed with coaxial cables. The feed points of the array element are set in the x-axis and y-axis directions to achieve dual-polarization. The metal stubs are embedded between two bottom substrates and connected with the inner connector of the coaxial cables to obtain an excellent impedance matching among antennas and feed ports. Two cavities are engraved on the PP board directly above the bottom antenna to provide a space for PCB solder. The inner-element distance of the array is half wavelength. TABLE I gives the detailed dimensions of the antenna array with and without TMS.

Fig. 7 (a) and (b) show the S-parameters of the arrays in the x-polarization and y-polarization. It demonstrates that by using the TMS, the couplings of the array in x-polarization and y-polarization are reduced to -25 dB and -26.4 dB over the working band. The operating band of the decoupled array in dual-polarization is 4.2-4.75 GHz. Moreover, the operating band of the array shifts to a higher band slightly. Initially, the distance  $hc$  between the array and TMS determines the decoupling level. The S-parameters of the decoupled array with different  $hc$  are presented in Fig. 7 (c) and Fig. 7 (d). It demonstrates that when the  $hc$  is 10 mm, the envelope of the  $S_{31}$  and  $S_{42}$  in dual-polarization is the lowest. This example perfectly verifies the proposed decoupling method TMS for the MIMO arrays.

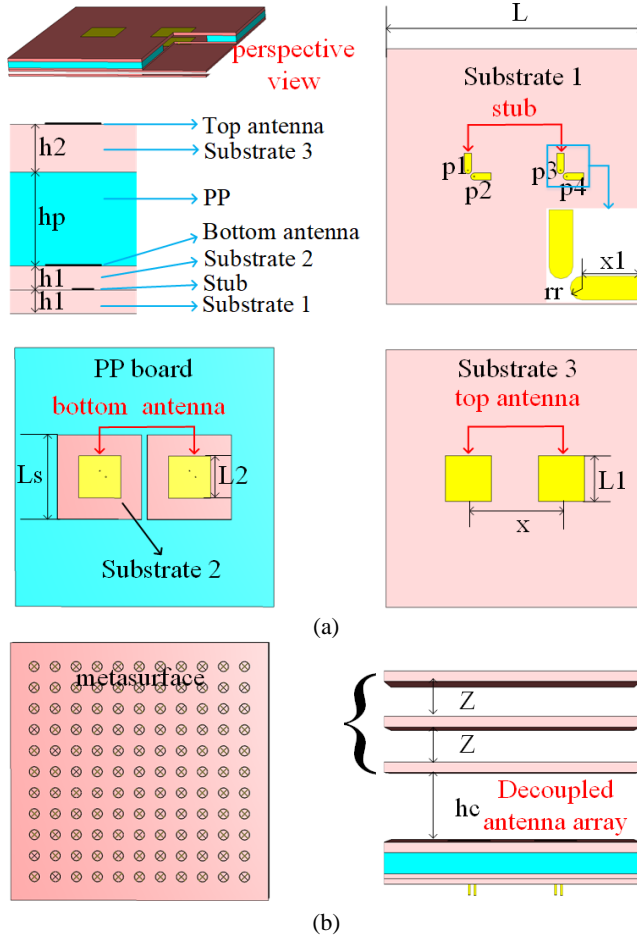
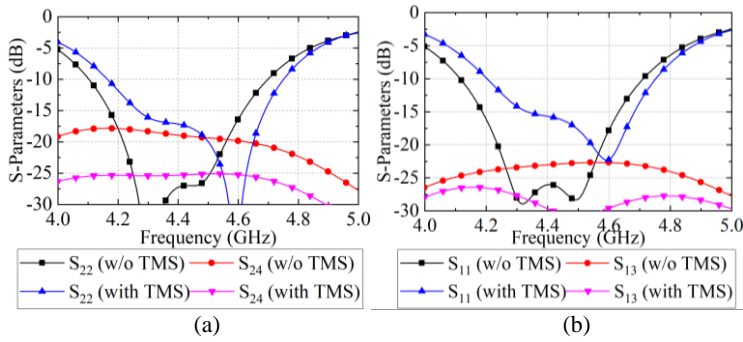


Fig. 6. The structure of the antenna array with and without TMS: (a) the overall structure of the reference array with specific dimensions, (b) the detailed structure of the array with TMS.



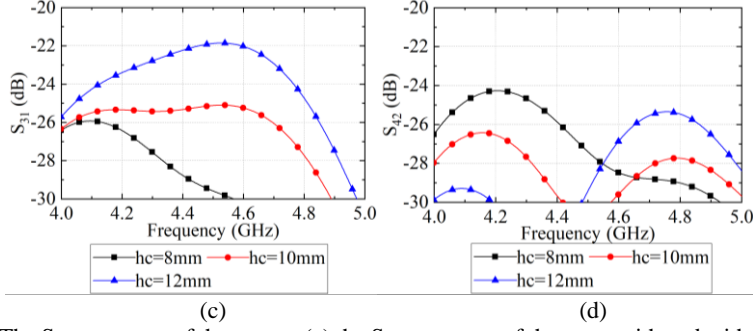


Fig. 7. The S-parameters of the arrays: (a) the S-parameters of the array with and without TMS in x-polarization, (b) the S-parameters of the array with and without TMS in y-polarization, (c) the  $S_{31}$  of the decoupled array with different  $hc$ , (d) the  $S_{42}$  of the decoupled array with different  $hc$ .

TABLE I  
PARAMETERS OF THE TMS

parameters	$L$	$X$	$XI$	$rr$	$L1$	$Ls$	$L2$
Value(mm)	2.75	33	6.2	1.3	16	31	16.8
parameters	$h1$	$hp$	$h2$	$hc$	$Z$	$T$	$g$
Value(mm)	0.762	3	1.524	10	5	8	0.2
parameters	$C$	$R$	$e$				
Value(mm)	0.2	2	2.3				

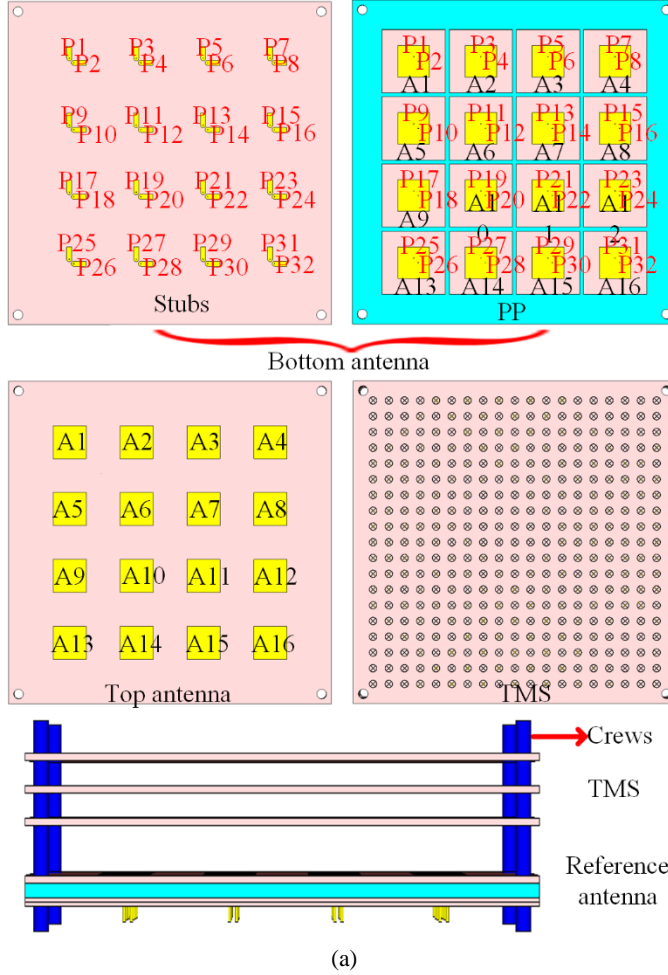
### III. Design example

For the dual-polarized massive MIMO arrays, the paths of the space waves coupling in dual-polarization and diagonal directions are complicated. Thus, the coupling between the adjacent and nonadjacent array elements is hardly reduced to the lowest level simultaneously. Therefore, the envelope of the S-parameters of all the paths should be lower than -24 dB.

#### A. Concept of the proposed TMS mutual decoupling method

A  $4 \times 4$  dual-polarization massive MIMO array with TMS is carried out to verify the proposed decoupling method TMS. Fig. 8 illustrates the configurations of the array with the specific dimensions and the corresponding prototype. The  $4 \times 4$  array adopts the same antenna element mentioned in previous mentioned one. The TMS is mounted above the array, and a prototype has been fabricated and installed. The antennas and TMS are fixed

together with nylon screws. The substrates have non-metalized holes at the corners to provide space for nylon screws to pass through. A foam board is placed directly above the array to support the TMS. The  $4 \times 4$  array with TMS and the corresponding fabricated prototype are shown in Fig. 8 (a) and (b), respectively.



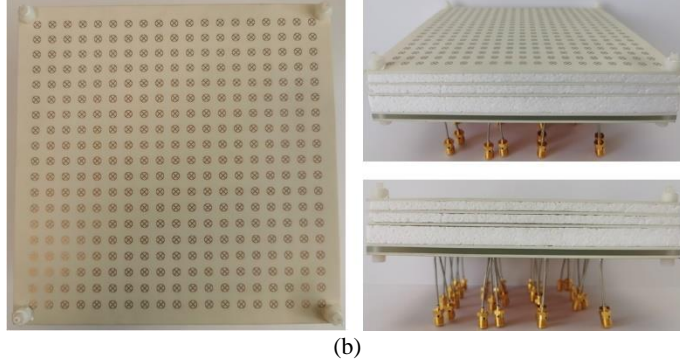


Fig. 8. The structure of the  $4 \times 4$  array with and without TMS: (a) the detailed structure of the array with TMS from top and side views, (b) the fabricated prototype of the array with TMS from top, side and perspective view.

## B. Antenna performance

The S-parameters of the  $4 \times 4$  arrays with and without TMS are simulated. And then, those of the array with TMS are measured. The results are shown in Fig. 9. Since the antenna array is symmetrical along x-direction and y-direction, the S-parameters of port 12 in the second quadrant are chosen and displayed. The couplings mainly exist among neighboring and non-neighboring elements in the x-direction, y-direction, and diagonal directions of the massive MIMO array. The  $S_{2,12}$  refers to the coupling between the adjacent elements in the diagonal direction of the array. The  $S_{4,12}$ ,  $S_{10,12}$ ,  $S_{16,12}$  and  $S_{28,12}$  represent the couplings between the neighboring and non-neighboring elements in y-polarization and x-polarization, respectively. The simulation results show that the proposed array with TMS works from 4.217-4.763 GHz, and all the port-to-port isolation can be improved from 17 dB to over 24 dB within the whole operating band. The impedance matching bandwidth of the array has a slight shift to the higher band. The measured results show that the operating band of the array is 4.23-4.82 GHz. The difference between the simulated and measured working band of the array is caused by the fabrication mistake. Due to the page length limitation, the rest S-parameters are not shown.

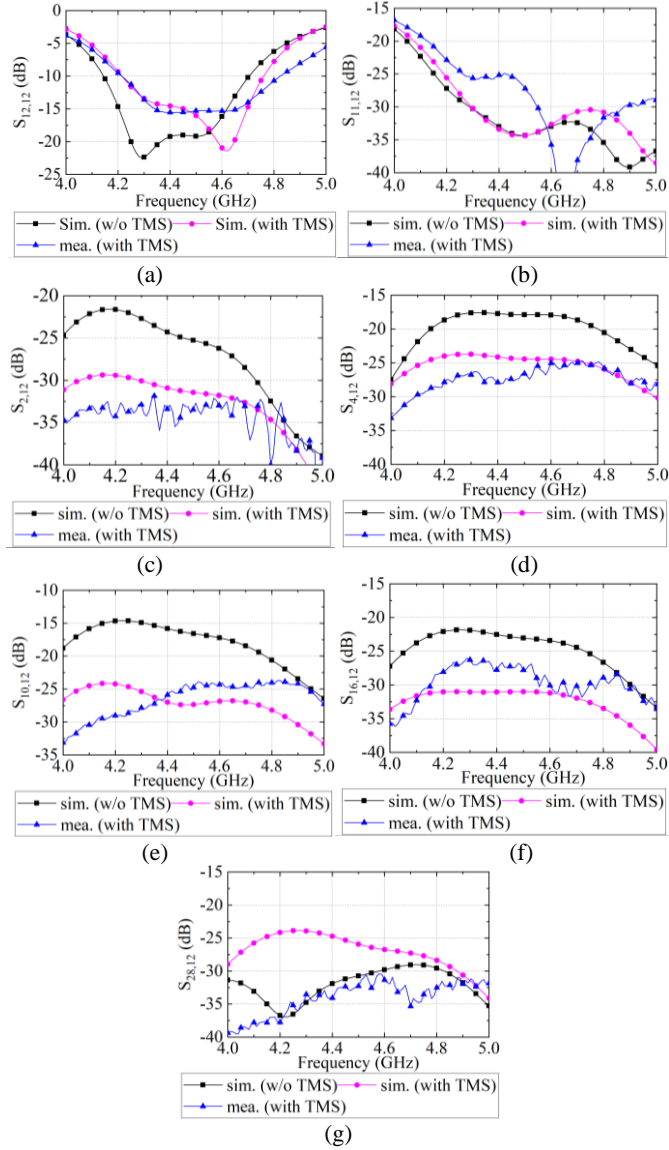
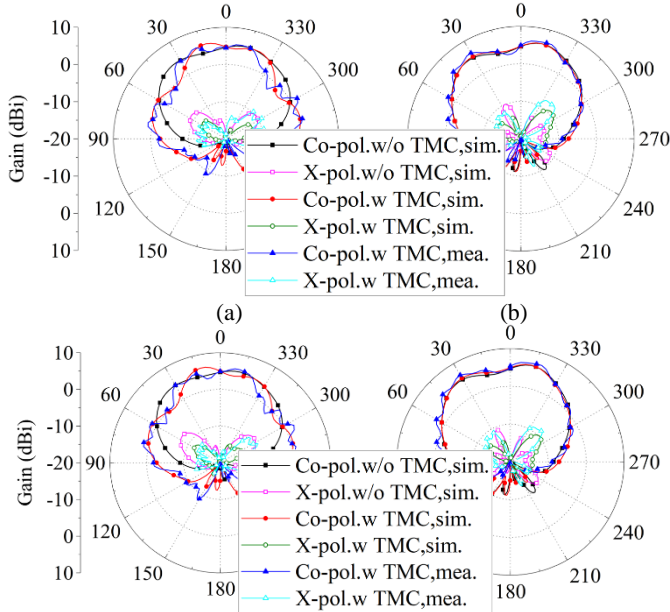


Fig. 9. The simulated and measured S parameters of the  $4 \times 4$  array with/without TMS: (a)  $S_{12,12}$ , (b)  $S_{11,12}$ , (c)  $S_{2,12}$ , (d)  $S_{4,12}$ , (e)  $S_{10,12}$ , (f)  $S_{16,12}$  and (g)  $S_{16,12}$ .

The element A12 have all types of coupling paths because of the features of symmetry, and it has similar radiation patterns with rest elements. The radiation patterns of antenna A12 at 4.5, 4.6, 4.7, and 4.8 GHz are selected. When we measure the radiation patterns of the array, the P12 (see Fig. 7(a)) is feed, and the other ports connect with 50-ohm loads. The microwave

chamber can provide an interference-free environment for the radiation patterns measurement. The radiation patterns of the array without and without the TMS are shown in Fig. 10. Compared with the simulated radiation patterns of the array without TMS, the simulated and measured radiation patterns of the arrays with TMS in the E-plane have some tiny ripples that result from the slight reflection of the TMS, the fabrication, and measurement tolerance. But the contours of the patterns are almost same. The measured patterns of the decoupled array in the H-plane match well with the simulated results before adding TMS. The results show that the radiation patterns of the array with and without loading TMS almost keep consistent. The radiation patterns of other array elements are measured and have similar results with the A12, which are not shown due to the page limitation. It aligned well with the theoretical analysis.

Fig. 7 (a) and (b) show the S-parameters of the arrays in the x-polarization and y-polarization. It demonstrates that by using the TMS, the couplings of the array in x-polarization and y-polarization are reduced to -25 dB and -26.4 dB over the working band. The operating band of the decoupled array in dual-polarization is 4.2-4.75 GHz. Moreover, the operating band of the array shifts to a higher band slightly. Initially, the distance  $hc$  between the array and TMS determines the decoupling level. The S-parameters of the decoupled array with different  $hc$  are presented in Fig. 7 (c) and Fig. 7 (d). It demonstrates that when the  $hc$  is 10 mm, the envelope of the  $S_{31}$  and  $S_{42}$  in dual-polarization is the lowest. This example perfectly verifies the proposed decoupling method TMS for the MIMO arrays.





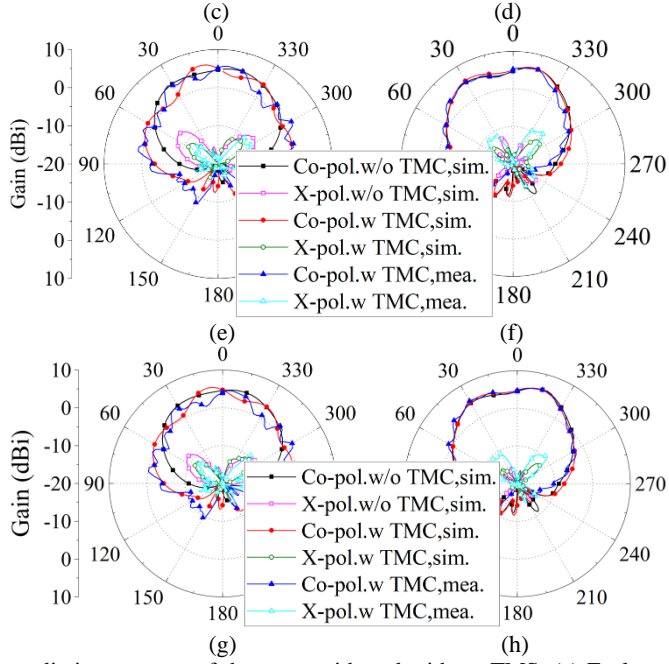


Fig. 10. The radiation patterns of the array with and without TMS, (a) E-plane of port 12 at 4.5GHz, (b) H-plane of port 12 at 4.5GHz, (c) E-plane of port 12 at 4.6GHz, (d) H-plane of port 12 at 4.6GHz, (e) E-plane of port 12 at 4.7GHz, (f) H-plane of port 12 at 4.7GHz, (g) E-plane of port 12 at 4.8GHz, (h) H-plane of port 12 at 4.9GHz.

The realized gain and the total efficiency of the element P12 at different frequencies before and after applying TMS are depicted in Fig. 11 (a) and (b), respectively. The results in Fig. 11 (a) show that the TMS improves the realized gain of the array. Meanwhile, Fig. 11 (b) exhibits the array efficiency is more than 76%. Due to the fabrication accuracy error and the power loss in coaxial cables, the measured real gain and total efficiency drop slightly.

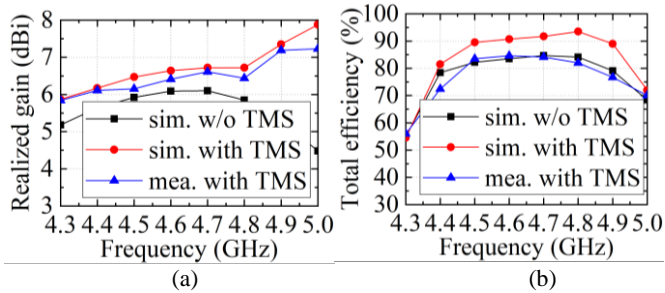


Fig. 11. The Realized gain and efficiency of the array with TMS: (a) realized gain, (b) total efficiency.

## IV. Performance comparison

An overall comparison between the proposed array with TMS and the other relevant techniques reported in recent literature is presented in Table II. The decoupling performance for the massive MIMO array in this work is comparable with the one in the recent work. But this work exhibits superiority over the working band compared with the techniques in [27]. The array with DG in [29] has a working band from 4.9-5.2 GHz (at the center frequency of 4.9 GHz), which is relatively narrow. Meanwhile, the inner-element distance of the array is larger than  $0.5\lambda_0$ . The ADS proposed in [28-29] develops complicated space waves paths to suppress the coupling of the array. Therefore, it increases the design complexity of the ADS. The array with TMS in this work has a lower profile than the array proposed in [30]. In addition, a low dielectric constant of the DDS is needed because a higher dielectric constant negatively deteriorates the impedance match of the antenna element. In contrast, the TMS in our work has no specific requirements on the dielectric constant of the dielectric substrate. It demonstrates that the decoupling method TMS for massive MIMO array offers numerous merits over other mentioned decoupling techniques.

TABLE II  
PARAMETERS COMPARISON

Ref.	[26]	[27]	[28]		[29]		[30]	<b>This work</b>
Decou. method	Transimission line	DG	ADS		ADS		DDS	<b>TMS</b>
Antenna type	Mic. Ant.	Mic. Ant.	Mic. Ant.	Mon.	Sta. Dip.	Sta. Dip.	Mic. Ant.	<b>Mic. Ant.</b>
Polarization	Dua.-pol.	Dua.-pol.	Sin.-pol.	Dua.-pol.	Dua.-pol.	Dua.-pol.	Dua.-pol.	<b>Dua.-pol.</b>
Array configuration	$2 \times 2$	$4 \times 4$	$1 \times 8$	$2 \times 2$	4-4-4-4	2-1-2	$4 \times 4$	<b><math>4 \times 4</math></b>
Freq. (GHz)	2.395-2.52	4.9-5.2	2.4-2.5	3.3-3.8	3.3-3.8	3.3-3.75	4.4-5.0	<b>4.23-4.82</b>
Height ( $\lambda_0$ )	NA	$0.25\lambda_0$	$0.32\lambda_0$	$0.33\lambda_0$	$0.4\lambda_0$	$0.39\lambda_0$	$0.466\lambda_0$	<b><math>0.45\lambda_0</math></b>

Antennas distance ( $\lambda_0$ )	$0.5\lambda_0$	$0.62\lambda_0$	$0.45\lambda_0$	$0.71\lambda_0$	$0.5\lambda_0$	$0.4\lambda_0$	$0.485\lambda_0$	<b><math>0.5\lambda_0</math></b>
Isolation	25	24.5	24	25	25	25	25	<b>24</b>
Compl. of the decoupling structure	complicated	complicated	complicated		complicated		simple	<b>simple</b>
Subs. of decoupling structure	Rogers RO3003 ( $\epsilon_r = 3$ )	Rogers RO4350 B ( $\epsilon_r = 3.66$ )	NA ( $\epsilon_r = 2.6$ )		NA ( $\epsilon_r = 3$ )	Rogers RO4730JXR ( $\epsilon_r = 2.98$ )	Polyimide (PLA) ( $\epsilon_r = 2.65$ )	Rogers RO4350B ( $\epsilon_r = 3.66$ )
Effec. for massive MIMO ant. array	yes	yes	yes	yes	yes	yes	yes	<b>yes</b>

## V. Conclusion

In this paper, a decoupling concept of the TMS was introduced. Then the decoupling mechanism of the TMS has been thoroughly analyzed. A massive MIMO array consists of  $4 \times 4$  elements has been designed, simulated, fabricated. The simulated and measured results show that the coupling of the array has been reduced from -18 dB to -24 dB by using TMS. In contrast, the radiation performance of the array keeps unchanged. The measurements of the practical array by employing the TMS justify the feasibility of the proposed decoupling technique. Since the proposed TMS has simple structure and symmetry characteristics, it can be easily integrated with the massive MIMO array. Finally, the worst isolation of the antenna array can be obtained.

## References

- [1] I. Akyildiz, A. Kak, and S. Nie, "6G and beyond: the future of wireless communications systems," *IEEE Access*, vol. 8, pp. 133995-134030, 2020.
- [2] R. He, B. Ai, G. L. Stüber, G. Wang, and Z. Zhong, "Geometrical based modeling for millimeter wave MIMO mobile-to-mobile channels," *IEEE Trans. Veh. Technol.*, vol. 67, no. 4, pp. 2828–2863, Apr. 2018.
- [3] C. Li , H. Zhu, J. Cai, J. Hu , G. Li , and G. Li, "Capacity analysis of terrestrial antenna array in distributed satellite MIMO communication system," *IEEE Trans. Veh. Technol.*, vol. 70, no. 5, pp. 4435–4450, May. 2018.
- [4] Y. Liu , C. Wang, J. Huang, J. Sun, and W. Zhang, "Novel 3-d nonstationary mm wave massive MIMO channel models for 5g high-speed train wireless communications," *IEEE Trans. Veh. Technol.*, vol. 68, no. 3, pp. 2077–2086, Mar. 2019.
- [5] H. Gao, Y. Su, S. Zhang, Y. Hou, and M. Jo, "Joint antenna selection and power allocation for secure co-time co-frequency full-duplex massive MIMO systems," *IEEE Trans. Veh. Technol.*, vol. 70, no. 1, pp. 655–665, Jun. 2021.
- [6] S. Chae, S. Oh, and S. Park, "Analysis of mutual coupling, correlations, and TARC in WiBro MIMO array antenna," *IEEE Antennas Wireless Propag. Lett.*, vol. 6, pp. 122-125, 2007.
- [7] D. M. Pozar, "A relation between the active input impedance and the active element pattern of a phased array," *IEEE Trans. Antennas Propag.*, vol. 51, no. 9, pp. 2486-2489, Sep. 2003.
- [8] Y. Wu, J. W. M. Bergmans, and S. Attallah, "Effects of antenna correlation and mutual coupling on the carrier frequency offset estimation in MIMO systems," In *Proc. Int. Conf. Wireless Commun. Netw. Mobile Comput. (WiCOM)*, Chengdu, China, Sep. 2010, pp. 1-4.
- [9] H. S. Lui and H. T. Hui, "Mutual coupling compensation for direction of-arrival estimations using the receiving-mutual-impedance method," *Int. J. Antennas Propag.*, vol. 2010, Jan. 2010, Art. no. 373061.
- [10] B. K. Lau, J. B. Andersen, G. Kristensson, and A. F. Molisch, "Impact of matching network on bandwidth of compact antenna arrays," *IEEE*

- Trans. Antennas Propag.*, vol. 54, no. 11, pp.3225-3238, Nov. 2006.
- [11] Z. Ying and D. Zhang, "Study of the mutual coupling, correlations and efficiency of two PIFA antennas on a small ground plane," *IEEE Antennas Propagat. Soc. Int. Symp.*, Washington, DC, Jul. 2005, pp. 305-308.
  - [12] X. Chen, S. Zhang, and A. Zhang, "On MIMO-UFMC in the presence of phase noise and antenna mutual coupling," *Radio Sci.*, vol. 52, no. 11, pp. 1386-1394, 2017.
  - [13] K. H. Chen and J. F. Kiang, "Effect of mutual coupling on the channel capacity of MIMO systems," *IEEE Trans. Veh. Technol.*, vol. 65, no. 1, pp. 398-403, Jan. 2016.
  - [14] R. Janaswamy, "Effect of element mutual coupling on the capacity of fixed length linear arrays," *IEEE Antennas Wireless Propag. Lett.*, vol. 1, pp. 157-160, 2002.
  - [15] L. Savy and M. Lesturgie, "Coupling effects in MIMO phased array," *IEEE Radar Conf. (RadarConf)*, Philadelphia, PA, USA, May 2016, pp. 1-6.
  - [16] M. Afaq Azam, A. Kumar Dutta, and A. Mukherjee, "Performance analysis of dipole antenna based planar arrays with mutual coupling and antenna position error in mm wave hybrid system," *IEEE Trans. Veh. Technol.*, vol. 70, no. 10, pp. 10209–10221, Oct. 2021.
  - [17] C. Fager, X. Bland, K. Hausmair, J. C. Cahuana, and T. Eriksson, "Prediction of smart antenna transmitter characteristics using a new behavioral mode ling approach," *IEEE MTT-SInt. Microw. Symp. Dig.*, Tampa, FL, USA, Jun. 2014, pp. 1-4.
  - [18] X. Zou, G. Wang, Y. Wang, and H. Li, "An efficient decoupling network between feeding points for multielement linear arrays," *IEEE Trans. Antennas Propag.*, vol.67, no. 5, pp. 3101-3108, May. 2019.
  - [19] M. Li, Y. Zhang, D. Wu, K. L. Yeung, L. Jiang, and R. Murch, "Decoupling and matching network for dual-band MIMO antennas," *IEEE Trans. Antennas Propag.*, vol. 70, no. 3, pp. 1764-1775, Mar. 2022
  - [20] D. Gao , Z. Cao , S. Fu , X. Quan and P. Chen, "A novel slot-array defected ground structure for decoupling microstrip antenna array," *IEEE Trans. Antennas Propag.*, vol.68, no. 10, pp. 7027-7038, Oct.

2020.

- [21] X. Yang, Y. Liu, Y. Xu, and S. Gong, "Isolation enhancement in patch antenna array with fractal UC-EBG structure and cross slot," *IEEE Antennas Wireless Propag. Lett.*, vol. 16, pp. 2175-2178, Nov. 2017.
- [22] Z. Qamar, U. Naeem, S. A. Khan, M. Chongcheawchamnan, and M. F. Shafique, "Mutual coupling reduction for high-performance densely packed patch antenna arrays on finite substrate," *IEEE Trans. Antennas Propag.*, vol. 64, no. 5, pp. 1653-1660, May. 2016.
- [23] M. Li, and S. Cheung, "A novel calculation-based parasitic decoupling technique for increasing isolation in multiple-element MIMO antenna arrays," *IEEE Trans. Vehicular Tec.*, vol. 70, no. 1, pp. 446-458, Jan. 2021.
- [24] W. Yang, L. Chen, S. Pan, W. Che, and Quan Xue, "Novel decoupling method based on coupling energy cancellation and its application in 5G dual-polarized high-isolation antenna array," *IEEE Trans. Antennas Propag.*, vol. 70, no. 4, pp. 2686-2697, Apr. 2022.
- [25] Z. Wang, L. Zhao, Y. Cai, S. Zheng and Y. Yin, "A meta-surface antenna array decoupling (MAAD) method for mutual coupling reduction in a MIMO antenna system," *Sci. Rep.*, vol. 8, Feb. 2018, Art. no. 3152.
- [26] M. Li, B. Zhong and S. W. Cheung, "Isolation enhancement for MIMO patch antennas using near-field resonators as coupling-mode transducers," *IEEE Trans. Antennas Propag.*, vol. 67, no. 2, pp. 755-764, Feb. 2019.
- [27] S. Luo, Y. Zhang, G. F. Pedersen, and S. Zhang, "Isolation enhancement for large-scale phased arrays using non-resonant metasurface," *IEEE Antennas Wireless Propag. Lett.*, submitted.
- [28] Y. Zhang, S. Zhang, J. Li, and G. F. Pedersen, "A transmission-line-based decoupling method for MIMO antenna arrays," *IEEE Trans. Antennas Propag.*, vol. 67, no. 5, pp. 3117-3131, May. 2019.
- [29] S. Zhang, X. Chen, and G. F. Pedersen, "Mutual coupling suppression with decoupling ground for massive MIMO antenna arrays," *IEEE Trans. Veh. Technol.*, vol. 68, no. 8, pp. 7273-7282, Aug. 2019.
- [30] K. Wu, C. Wei, X. Mei and Z. Zhang, "Array-antenna decoupling surface," *IEEE Trans. Antennas Propag.*, vol. 65, no. 12, pp. 6728-

6738, Dec. 2017.

- [31] C. Wei, Z. Zhang, and K. Wu, "Phase compensation for decoupling of large-scale staggered dual-polarized dipole array antennas," *IEEE Trans. Antennas Propag.*, vol. 68, no. 4, pp. 2822-2831, Apr. 2020.
- [32] P. Mei, Y. Zhang, and S. Zhang, "Decoupling of a wideband dual-polarized large-scale antenna array with dielectric stubs," *IEEE Trans. Vehicular Tec.*, vol. 70, no. 8, pp. 7363-7374, Aug. 2021.

# Paper C

## Massive MIMO Array Design with High Isolation by Using Decoupling Cavity

Shengyuan Luo, Gert Frølund Pedersen, Shuai Zhang

This paper has been published at the  
IEEE Transactions on Circuits and Systems II: Express Briefs, vol. 70, no. 3,  
pp. 974-978, March 2023.





## Abstract

*This letter proposes an isolation enhancement method for massive multiple-input multiple-output arrays using decoupling cavities (DC). The proposed DC is made of a pure Polypropylene (PP) board, and an air cavity is engraved on it. The DC has high transmission in the normal direction and a high insertion loss in the tangential direction of the arrays, respectively. The DC operates with a broadband response due to the low dielectric constant of the substrate. An example of a  $4 \times 4$  array with an inter-element distance around half wavelength is designed to verify the proposed isolation enhancement method. The triple-layers stacked DC are employed seamlessly above the array. The isolation of the array was enhanced to 24 dB within the bandwidth of 4.21-4.79 GHz. At the same time, the radiation characteristics of the arrays before and after loading the DC basically keep consistent.*

## I Introduction

The massive multiple-input multiple-output (MIMO) systems have been widely used in current and future wireless communications [1-3]. During the implementation progress, the mutual coupling of the array seriously degrades the antenna performance, such as signal-to-noise ratio, active voltage standing wave ratio (VSWR), impedance match, and channel capacity [4-6]. Thus, researchers have paid much effort to the isolation enhancement for massive MIMO arrays.

The isolation enhancement in terms of the surface waves coupling suppression includes electromagnetic bandgap structure (EBG), defected ground structure, parasitic structures, metamaterial, and so on [7-11]. Typically, the mentioned technologies need a relatively larger space to employ the decoupling structure between the array elements. Therefore, it is inapplicable for massive MIMO arrays with a compact layout. Regarding reducing the space waves coupling, a metasurface and a dielectric block for two-element were proposed in [12] and [13], respectively. However, they face some difficulties for massive MIMO arrays with more intricate coupling paths.

For the massive MIMO arrays, a phase compensation method-based array decoupling surface (ADS) was developed in [14] to simultaneously reduce the couplings between adjacent co-polarized antenna elements with diversified phase legging, but the issue of high design complexity cannot be avoided. Transmission-line-based decoupling technology was proposed in [15], yet it

worked with a narrow bandwidth response. Reference [16] presented a decoupling method of a near-field resonator for large-scale arrays, but it is difficult to be extended to dual-polarized arrays due to the feature of asymmetry. Reference [17] introduced a decoupling ground to make the mutual coupling between the free space and the ground out of phase. However, the distance between the array elements is around  $0.62\lambda$ . Reference [18] proposed an embeddable structure for reducing mutual coupling in a  $3 \times 3$  MIMO array, but the worst co-polarized mutual isolation is only 20 dB. Reference [19] proposed a decoupling method of dielectric superstrate. But it can only be used in dual-element and single polarized array.

This letter proposes a scheme for implementing a massive MIMO array with high isolation by utilizing DC. The distance between the array elements is around half wavelength. The proposed DC has high transmission in the normal direction and high insertion loss in the tangential direction of the array. So that the space waves can normally propagate in the normal direction, and the propagation of the space waves along the parallel direction of the arrays can be suppressed. Three-layer stacked DC are mounted seamlessly above the reference array to enforce the decoupling effect. The proposed decoupling mechanism, an example of a  $4 \times 4$  array, and antenna performance is described.

## **II The example of $4 \times 4$ array with DC**

### **A. Decoupling scheme of the DC**

The space wave coupling dominates for the array with an inter-element distance of around half wavelength. For any array element of the massive MIMO array, the space waves are radiated in all directions in space. Therefore, the massive MIMO array has complicated coupling paths. But most coupling energy is radiated to the adjacent and non-adjacent elements in linear and diagonal directions, where the space coupling in E-Plane and H-plane play a decisive role. Correspondingly, the total decoupling performance can be carried out by reducing the space coupling in the E-plane or E-plane of the array with an inter-element distance of half-wavelength. Fig. 1 presents the decoupling schematic diagrams of the DC for massive MIMO arrays. Our goal is to design a decoupling structure that can suppress the propagation of the space waves along the tangential direction of arrays. In this paper, a DC is designed and loaded on the top surface of the original array. Here, the DC performs high transmission in the normal direction and high insertion loss in the tangential direction of the array. Consequently, the space coupling component attenuates when it propagates along the x-direction, which leads

to strong energy insertion loss. Finally, the space waves coupling can be suppressed. Meanwhile, the DC has a perfect impedance matching with the arrays due to high transmission in the normal direction.

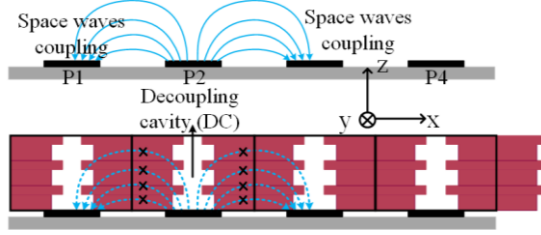


Fig. 1. Decoupling schematic of the massive MIMO arrays with the DCs.

## B. The of $4 \times 4$ array antenna design

Fig. 2 depicts the geometries and specific dimensions of the  $4 \times 4$  dual-polarized and wideband massive MIMO array with the proposed DC. Fig. 2 (a) and (b) present the decoupled  $4 \times 4$  array and the detailed structure of the DC, respectively. Fig. 2 (b) shows the reference array and the prototype.

Each DC unit consists of two layers of pure PP (polypropylene) boards, where the permittivity of PP is around 2.2. Two air cavities are etched on the PP boards to adjust the insertion loss. The first layer has a thickness of 3 mm with a smaller square air cavity, while the second layer has a thickness of 6 mm with a larger square air cavity. Here, the period of the DC is set as the inter-element distance between the array elements. The extra weight of the adding material is 600 g in total. In the applications, it is also easy to find some other light materials with the permittivity of around 2.2, so the weight can be much further reduced.

Based on the decoupling concept of DC, an actual example of a  $4 \times 4$  dual-polarized and wideband massive MIMO array with the proposed DC is carried out. The array element comprises two-layer stacked microstrip antennas to broaden the bandwidth. The metal patches are printed on the RO 4350B substrates with a permittivity of 3.66 and a loss tangent of 0.002. Four slots are etched on the metal patches of the bottom and top microstrip antenna to reduce the coupling level between two feed ports of the array elements themselves. In addition, the slots on the bottom and top antennas have the same size. The antennas are fed by the coaxial cables, where the inner conductors and the outer conductors of the cables connect with metal patches and the common ground of the bottom antennas, respectively. A PP board with air cavities above the feed point is inserted between the bottom and top

substrates. Then, the DC is mounted on the top surface of the array to reduce the coupling. The optimized dimensions of the decoupled array are listed in TABLE I.

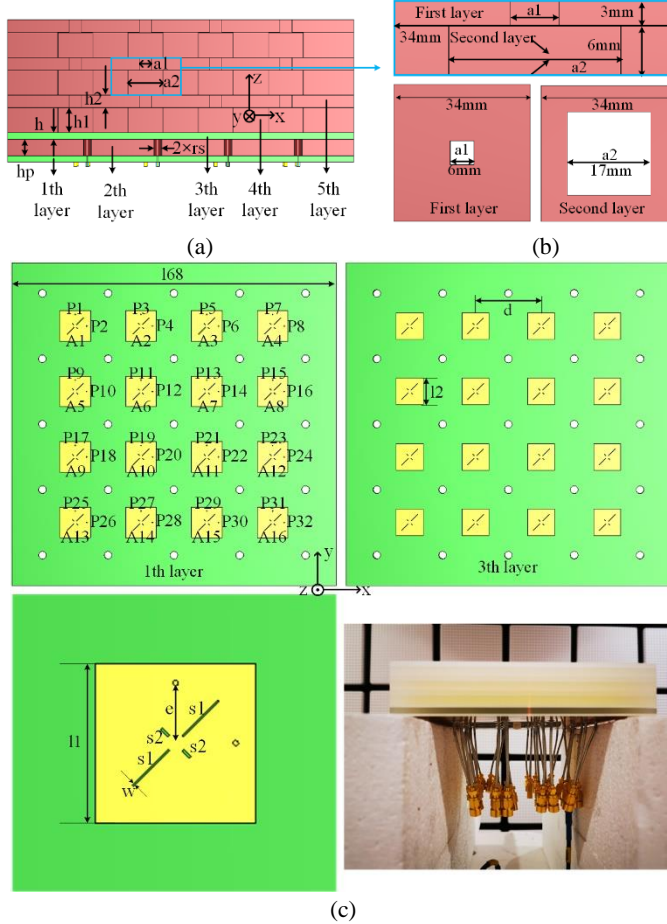


Fig. 2. Geometry and specific dimensions of the array with the proposed DC and the prototype: (a) the decoupled  $4 \times 4$  array, (b) the detailed structure and specific dimensions of the DC, (c) the reference array and the prototype.

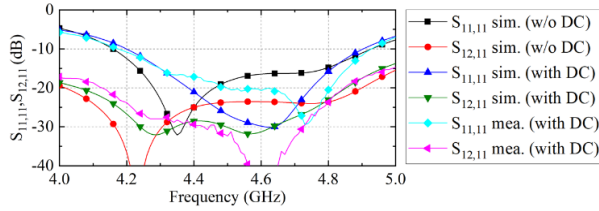
TABLE I  
DIMENSIONS OF THE DECOUPLED ARRAY

Parameters	$l$	$l1$	$l2$	$d$	$e$
Values(mm)	168	8	7	34	6.8
parameters	$rs$	$a1$	$a2$	$h$	$hp$
Values(mm)	2	6	17	1.524	4

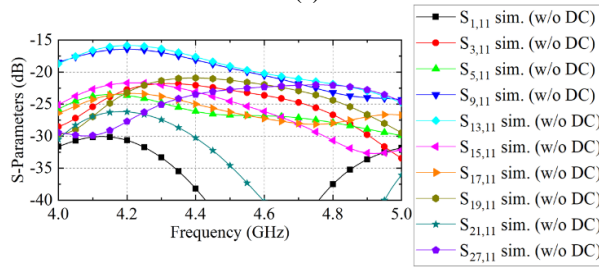
parameters	<i>s1</i>	<i>s1</i>	<i>h1</i>	<i>h2</i>
Values(mm)	5	2	6	3

### C. The antenna performance

For the  $4 \times 4$  arrays, the inner loop array elements have a more comprehensive coupling type with the other array elements. Additionally, since the symmetry feature of the arrays, element A6 has similar coupling paths with the other inner loop elements. Therefore, the mutual coupling between A6 and other elements can represent all the coupling types. The mutual coupling in this paper refers to the port-to-port mutual coupling. Here, we select the S-parameter of feed port P11 of the arrays before and after employing the DC and give it in Fig. 3. Notably, the  $S_{11,11}$  and  $S_{12,11}$  represent the reflection coefficient and the orthogonal polarized coupling level of the array elements themselves. The  $S_{1,11}$ ,  $S_{5,11}$ ,  $S_{17,11}$ , and  $S_{21,11}$  represent the mutual coupling between the adjacent elements in the diagonal directions. The  $S_{3,11}$ ,  $S_{19,11}$ , and  $S_{27,11}$  denote the mutual coupling between the adjacent and non-adjacent elements in y-polarization, respectively. Meanwhile, the  $S_{9,11}$ ,  $S_{13,11}$ , and  $S_{25,11}$  are the mutual couplings between the adjacent and non-adjacent elements in x-polarization, respectively. The configures of  $S_{11,11}$ ,  $S_{12,11}$ , and the rest S-parameters illustrate that the -24 dB decoupling bandwidth of the arrays is 4.21-4.79 GHz.



(a)



(b)

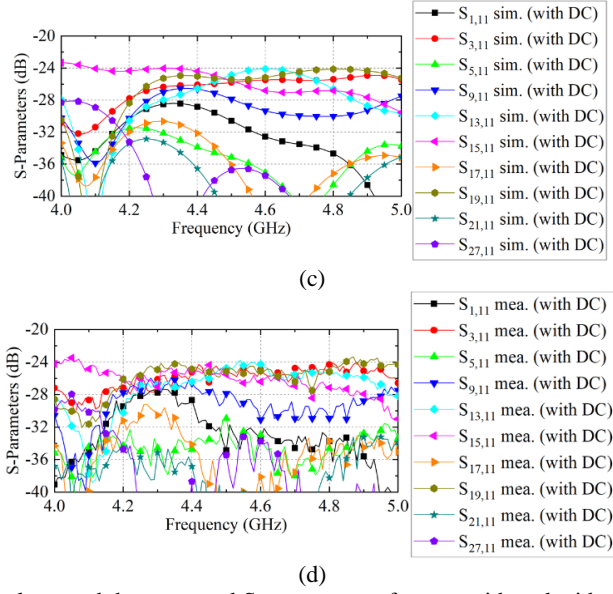


Fig. 3. The simulates and the measured S-parameters of arrays with and without DC: (a)  $S_{11,11}$  and  $S_{12,11}$ , (b) Simulated S-parameters of the array without DC, (c) Simulated S-parameters of the array with DC, (d) Measured S-parameters of the array with DC.

The simulated and measured radiation patterns of the array elements in the E-plane and H-plane at 4.3 GHz, 4.5 GHz, and 4.7 GHz are selected and shown in Fig. 4. It shows that the radiation patterns with decoupling in the E plane have amelioration to a certain degree. But the slightly deterioration occurs in the H plane at  $60^\circ$  and  $315^\circ$ . There is a trade-off between the patterns in the E-plane and H-plane. Besides, the radiation patterns in the H plane are also broader than those without decoupling, which will enhance the large angle scanning property of the array. In addition, the cross-polarized level of the array in the E-plane and H-plane is relatively high, which is caused by the engraved slot along  $\pm 45^\circ$  on the patches, thereby a current distribution along  $\pm 45^\circ$  is generated that contributes to the deterioration of the x-pol level. Due to the radiation patterns cannot be cut with a plane in every direction. Thus, the radiation patterns are usually cut in E-plane and H-plane for the convenience of observation. Although the x-polarization level observed in E-plane and H-plane is higher than -20 dB, the x-polarization level can reach an ideal level in other cutting planes according to the energy conservation law.

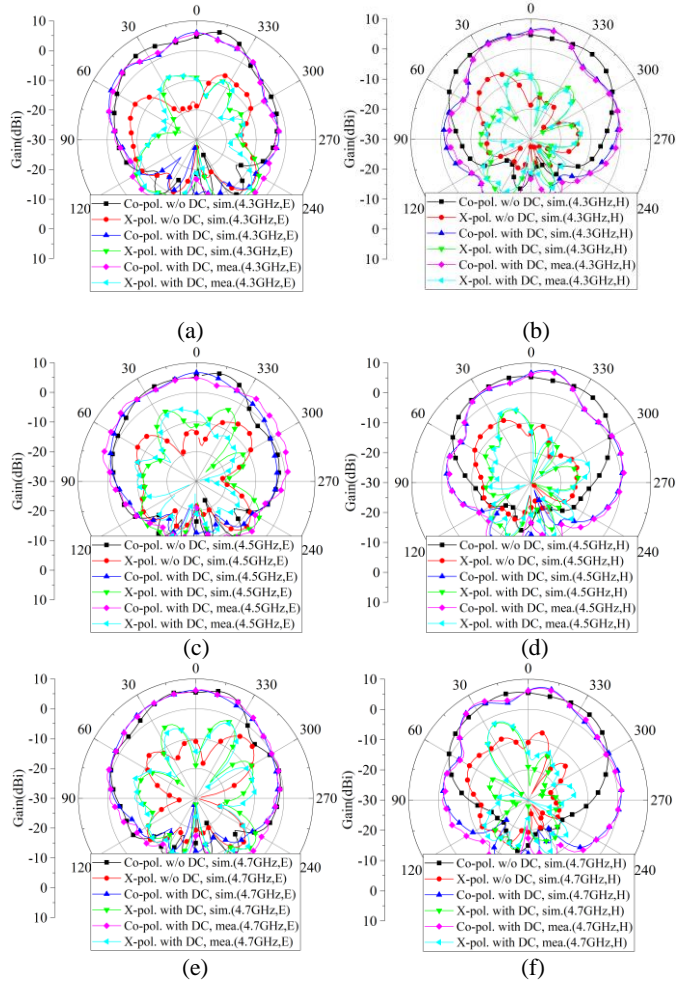


Fig. 4. The radiation patterns of the arrays with and without DC: (a) E-plane of port 1 at 4.3GHz, (b) H-plane of port 1 at 4.3GHz, (c) E-plane of port 1 at 4.5GHz, (d) H-plane of port 1 at 4.5GHz, (e) E-plane of port 1 at 4.7GHz, (f) H-plane of port 1 at 4.7GHz.

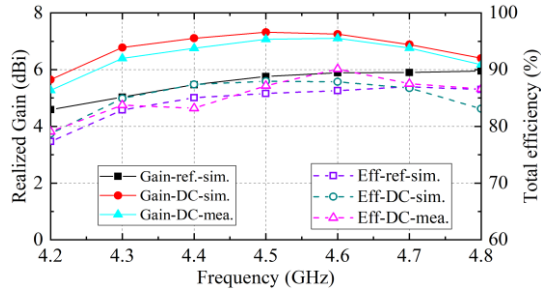


Fig.5 The realized gain and total efficiency of the array with and without DC.



Fig. 5 presents the realized gain and the total efficiency of the arrays with and without DC, respectively. When the DC is placed on the top surface of the array, the effective radiation area of the microstrip antenna is enlarged to all the cross-section of the DC unit. Therefore, the microstrip antenna with DC has a larger radiation aperture. The antenna gain is improved by mounting the DC. Consequently, both the realized gain and total efficiency have significant increments by using DC. During the progress of designing a MIMO transmission system, the mutual coupling effect must be alleviated to avoid high active VSWR at transmitter ports. The ECC is another indicator to measure the decoupling performance of the array as well. Here, the simulation results of ECC with and without decoupling are lower than 0.003. Thus, the ECC between the excitation ports is not the main issue, which is not shown in this paper due to the length limitation.

### **III Analysis of parameters study and decoupling mechanism**

#### **A. Parametric study**

The sizes  $a_1$  and  $a_2$  of the air cavity determine the decoupling performance of the  $4 \times 4$  arrays. Parametric studies for the overall array with DC have been carried out to illustrate the effect of the  $a_1$  and  $a_2$  on the decoupling level. Fig. 6 (a) and Fig. 6 (b) give the S-parameters with different  $a_1$  and  $a_2$ , respectively. The same S-parameters are selected as the above-mentioned ones in the last section. It can be found that when  $a_1$  is 6 mm and  $a_2$  is 17 mm, the lowest coupling is obtained within the working band (lower than -24 dB), which means the highest insertion loss is got in the tangential direction of the DC. But when  $a_1$  and  $a_2$  are set as other values, the S-parameters is higher than -24 dB. The simulated results also illustrate that  $a_1$  and  $a_2$  play the fine-tuning and decisive roles during the progress of decoupling for the  $4 \times 4$  arrays, respectively.

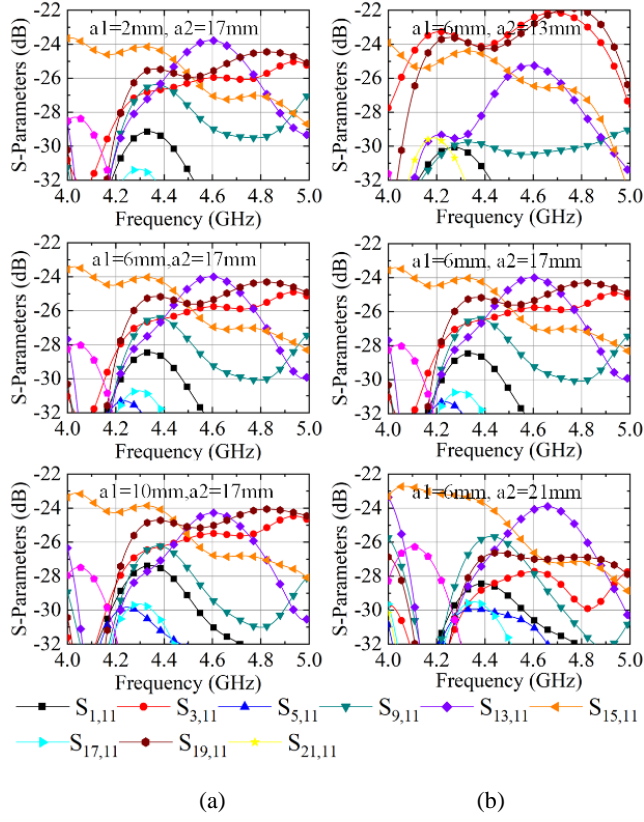


Fig.6 The S-parameters of the array with DC, (a) different  $a_1$  as  $a_2$  is 17mm, (b) different  $a_2$  as  $a_1$  is 6mm.

## B. E-fields

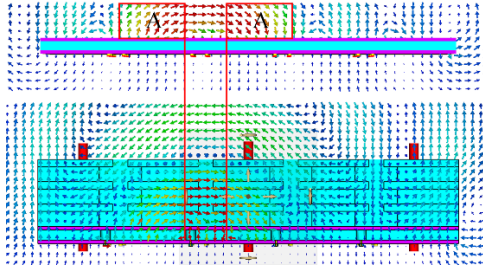


Fig.7 The E-fields of the  $4 \times 4$  arrays with and without DC.

To better understand the decoupling mechanism of the proposed DC, the E-field distributions of the  $4 \times 4$  arrays with and without DC in H-plane are presented in Fig. 7. By comparing the E-fields of the array with and without

DC, it shows that when there is no DC on the top surface of the array, the E-field in the region A is very strong, which means the strong space waves coupling component propagates to the neighboring elements. While the DC is loaded, the E-field in the same position is extremely weak and constrained in the DC, where fewer space waves coupling component can propagate through the DC. The E-field in E-plane has a similar result with that in H-plane. All the results provide a vision proof that the proposed DC can effectively suppress the propagation of the main coupling component.

According to the parametric study and E-field of the array with and without DC prementioned above, the design criterion of the DC can be concluded as here. The DC unit consists of two layers of pure PP boards stacked together. Two air cavities are etched on the pp boards to form a DC. First, the cavities on the bottom and top layers of PP boards have the same dimensions. Then, the envelope of the S-parameter, lower than -24 dB, can be carried by varying the cavity sizes of the  $a_2$  and  $a_1$  in order. It should be noted that the air cavity in the bottom substrate should have a larger size than the radiation patches so that the propagation of the space waves coupling along the tangential direction of the array can be effectively suppressed.

## IV Comparison

A comprehensive comparison between the proposed decoupling technology of DC and the current literature for massive MIMO arrays is made and listed in TABLE II. It is observed that the inter-element distance of the arrays in [14] and [17] are relatively large. Furthermore, the isolation of these arrays does not have a prominent increment. In addition, though the decoupling structure proposed in [14] and [18] has a rather wide bandwidth, they have high design and fabrication complexity. The near-field resonator is a novel decoupling concept, but it has a narrow working band, and its isolation can only be enhanced to 20 dB. The antenna height is not the most important index in the actual application. Therefore, although the array in our work has the highest profile, its effect can be neglected. In addition, on the basis of ensuring the requirements of the wideband operating band, the array in our work has relatively high total efficiency. The gain of our work is comparable with that in [14] and higher than in [16], [17], and [18]. The cross-polarization level in our work is higher than the rest arrays, but it is caused by the inherent defects of the antenna unit itself. An array with a low cross-polarization level and wider bandwidth can be got by replacing the original array element with one that has improved performance. The complexity and the cost of the fabrication

for the industrial application is important. The DC proposed in this paper only needs to be mounted on the top surface of the array without any air gap, which almost does not introduce deformation. PP and other low-permittivity materials are common in the market and easy to obtain. Obviously, the proposed decoupling concept has the best fabrication tolerance, complexity, and cost. In conclusion, the array with DC has an overall high performance and industrial application value compared with the others in current literature. Besides, it is worth noting that the proposed DC is mainly used to suppress the space waves coupling component. This method is general and can be used for the planar array antennas with other kinds of elements, such as monopole and dipole antennas, making it as a promising candidate for the wireless communication systems.

TABLE II  
PERFORMANCES COMPARISON

Ref.	[14]	[16]		[17]	[18]	This work
Method	ADS	Near-field resonator		DG	Embed. structure	DC
Frequency (GHz)	3.2-3.9 (19.7%)	2.38-2.53 GHz (6.1%)	2.38-2.49 GHz (4.5%)	4.9-5.2 (5.9%)	3.3-4.5 (30.8%)	<b>4.21-4.79 (12.9%)</b>
Height ( $\lambda_0$ )	0.40 $\lambda_0$	0.05 $\lambda_0$		0.25 $\lambda_0$	0.31 $\lambda_0$	<b>0.45<math>\lambda_0</math></b>
Inter-element distance ( $\lambda_0$ )	0.65 $\lambda_0$ , 0.40 $\lambda_0$	0.47 $\lambda_0$		0.62 $\lambda_0$	0.56 $\lambda_0$	<b>0.5<math>\lambda_0</math></b>
Total efficiency	NG	NG		>90%	80%	<b>&gt;80%</b>
X-polarization	>10	>9		>10	>10	<b>&gt;7</b>
Gain (dBi)	8.0	4.45		7.3	6.5	<b>7.9</b>
Isolation	25	20		24.5	20	<b>24</b>
Pot. for wider-b. and low x-pol.	no	no		no	no	<b>yes</b>
Toler., cost, and	high	high		high	high	<b>low</b>

complex. of fab.					
Embed.: Embeddable	Pot.: Potential	x-pol.: x-polarization	Toler.: Tolerance		
Complex.: Complexity	fab.: fabrication				

## V Conclusion

This letter developed a concept of DC for massive MIMO arrays. The decoupling mechanism was analyzed in detail. A DC element was proposed with an air cavity engraved on it to raise the transmission in the normal direction and the insertion loss characteristics in the tangential direction of the DC. The  $4 \times 4$  massive MIMO array was simulated, fabricated, and measured. The results illustrate that the DC can effectively enhance the isolation of the array to more than 24 dB within the bandwidth of 4.21-4.79 GHz. In addition, the realized gain and the total efficiency of the array with DC have a significant increment. The parametric study and E-field of the array before and after decoupling are given to provide a basic design criterion. Furthermore, the proposed decoupling method has the potential of being applied in other array types, such as monopole and dipole arrays.

## References

- [1] À. O. Martínez, J. Ø. Nielsen, E. D. Carvalho, and P. Popovski, "An experimental study of massive MIMO properties in 5g scenarios," *IEEE Trans. Antennas Propag.*, vol. 66, no. 12, pp. 7206-7215, Dec. 2018.
- [2] G. R. Nikandish, G. R. Nikandish, A. Zhu, "A fully integrated gan dual-channel power amplifier with crosstalk suppression for 5G massive MIMO transmitters," *IEEE Trans. on circ. and syst. II: expr. brie.*, vol. 68, no. 1, pp. 246-250, Jun. 2021
- [3] X. Chen, S. Zhang, and Q. Li, "A review of mutual coupling in MIMO systems," *IEEE Access*, vol. 6, pp. 24706-24719, 2018.
- [4] O. Saatlou, M. O. Ahmad, and M. N. S. Swamy, "Spectral efficiency maximization of multiuser massive MIMO systems with finite-dimensional channel via control of users' power," *IEEE Trans. on circ. and syst. II: expr. brie.*, vol. 65, no. 7, pp. 883-887, Jul. 2018.
- [5] O. Castañeda, S. Jacobsson, G. Durisi, T. Goldstein, and C. Studer, "High-bandwidth spatial equalization for mm wave massive MU-

- MIMO with processing-in-memory,” *IEEE Trans. on circ. and syst. II: expr. brie.*, vol. 67, no. 5, pp. 891-895, May. 2020.
- [6] A. Zhang, W. Cao, P. Liu, J. Sun, and J. Li “Channel Estimation for MmWave Massive MIMO With Hybrid Precoding Based on Log-Sum Sparse Constraints,” *IEEE Trans. on circ. and syst. II: expr. brie.*, vol. 68, no. 6, pp. 1882- 1886, Jun. 2021.
  - [7] X. Tan, W. Wang, Y. Wu, Y. Liu, and A. A. Kishk, “Enhancing isolation in dual-band meander-line multiple antenna by employing split EBG structure,” *IEEE Trans. Antennas Propag.*, vol. 67, no. 4, pp. 2769-2774, Apr. 2019.
  - [8] W. Wang, Y. Wu, W. Wang, and Y. Yang, “Isolation enhancement in dual-band monopole antenna for 5G applications,” *IEEE Trans. on circ. and syst. II: expr. brie.*, vol. 68, no. 6, pp. 1867- 1871, Jun. 2021.
  - [9] C. Tang, X. Chen, T. Shi, H. Tu, Z. Wu, and R. W. Ziolkowski, “A compact, low-profile, broadside radiating two-element huygens dipole array facilitated by a custom-designed decoupling element,” *IEEE Trans. Antennas Propag.*, vol. 69, no. 8, pp. 4546- 4557, Aug. 2021.
  - [10] Z. Qamar, U. Naeem, S. A. Khan, M. Chongcheawchamnan, and M. F. Shafique, “Mutual coupling reduction for high-performance densely packed patch antenna arrays on finite substrate,” *IEEE Trans. Antennas Propag.*, vol. 64, no. 5, pp. 1653- 1660, May. 2016.
  - [11] Y. Zhu, Y. Chen, and S. Yang, “Helical Torsion Coaxial Cable for Dual-Band Shared-Aperture Antenna Array Decoupling,” *IEEE Trans. Antennas Propag.*, vol. 68, no. 8, pp. 6128-6135, Aug. 2020.
  - [12] F. Liu, J. Guo, L. Zhao, G. Huang, Y. Li, and Y. Yin, “Dual-band metasurface-based decoupling method for two closely packed dual-band antennas,” *IEEE Trans. Antennas Propag.*, vol. 68, no. 1, pp. 552-557, Jan. 2020.
  - [13] M. Li, M. Y. Jamal, L. Jiang, and K. L. Yeung, “Isolation Enhancement for MIMO Patch Antennas Sharing a Common Thick Substrate: Using a Dielectric Block to Control Space-Wave Coupling to Cancel Surface-Wave Coupling,” *IEEE Trans. Antennas Propag.*, vol. 69, no. 4, pp. 1853-1863, Apr. 2021.
  - [14] K. Wu, C. Wei, X. Mei and Z. Zhang, “Array-antenna decoupling

- surface,” *IEEE Trans. Antennas Propag.*, vol. 65, no. 12, pp. 6728–6738, Dec. 2017.
- [15] Y. Zhang, S. Zhang, J. Li, and G. F. Pedersen, “A Transmission-Line-Based Decoupling Method for MIMO Antenna,” *IEEE Trans. Antennas Propag.*, vol. 67, no. 5, pp. 3117–3131, May. 2019.
  - [16] M. Li, B. G. Zhong, and S. W. Cheung, “Isolation enhancement for MIMO patch antennas using near-field resonators as coupling-mode transducers,” *IEEE Trans. Antennas Propag.*, vol. 67, no. 2, pp. 755–764, Feb. 2019.
  - [17] S. Zhang, X. Chen, and G. F. Pedersen, “Mutual coupling suppression with decoupling ground for massive MIMO antenna arrays,” *IEEE Trans. Veh. Technol.*, vol. 68, no. 8, pp. 7273–7282, Aug. 2019.
  - [18] Y. Qin, R. Li, and Y. Cui, “Embeddable structure for reducing mutual coupling in massive MIMO antennas,” *IEEE Trans. Access*, vol. 8, pp. 195102–195112, Oct. 2020.
  - [19] M. Li and S. Cheung, “Isolation Enhancement for MIMO Dielectric Resonator Antennas Using Dielectric Superstrate,” *IEEE Trans. Antennas Propag.*, vol. 69, no. 7, pp. 4154–4159, Jul. 2021.

# Paper D

Decoupling for Millimeter-Wave Array Antennas Using  
Near-Field Shrinking Dielectric Superstrate

Shenyuan Luo, Yiming Zhang, Peng Mei, Gert Frølund  
Pedersen, Shuai Zhang

This paper has been submitted at the  
IEEE Open Journal of Antennas and Propagation.





## Abstract

*A decoupling concept of near-field shrinking dielectric superstrate (NFSDS) is proposed for large-scale, wideband, and dual-polarized mm-wave arrays. An NFSDS with a thickness of 4 mm ( $0.32 \lambda_0$  at 24 GHz) is mounted seamlessly above the array, which shrinks the near field of the array elements to reduce the space wave coupling while slightly increasing the surface wave coupling of the arrays. By loading a superstrate with a certain thickness and low permittivity, the total coupling of the mm-wave arrays is reduced significantly. Periodic air holes are drilled through the superstrate to lower the NFSDS permittivity. An  $8 \times 8$  mm-wave array is simulated, fabricated, and measured to verify the proposed decoupling concept. The simulated and measured coupling of the mm-wave array is reduced from -17 dB to lower than -23.2 dB from 24 – 29.5 GHz and lower than -25 dB in most of the band, respectively. The radiation patterns of the array before and after decoupling almost keep unchanged. Moreover, the NFSDS can efficiently improve the array beam scanning capability. The measured results align well with the simulated.*

## I Introduction

The large-scale mm-wave arrays is an important research topic that has attracted tremendous attention over the past few years [1]. Since the mutual coupling between array elements seriously deteriorates the performance of the arrays, such as active VSWR, bandwidth, active reflection coefficient, efficiency, signal-to-interference noise ratio, and channel capacity [2]-[7], therefore, it is demanding to suppress the coupling of large-scale arrays.

Recent years have witnessed the efforts devoted to reducing the coupling of the arrays in the low-frequency bands, such as electromagnetic bandgap (EBG) [8], defected ground (DGS) [9], resonator [10], neutralization line [11] and parasitic element structure [12], which are commonly arranged between array elements. Thus, the inner-element distance needs to be large enough to accommodate the decoupling structure. The decoupling network is an effective method for mutual coupling suppression [13], which commonly operates within a narrow bandwidth. The metasurface is another effective decoupling method, which is typically loaded above the arrays with a distance [14]-[15]. However, the mm-wave arrays are very sensitive to the distance between the metasurface and the array. Therefore, such a distance would affect the decoupling performance. A decoupling method of orthogonal feeding structure was proposed in [16]. However, it cannot be used in large-scale phased arrays either. A sub-6 GHz massive MIMO array with high isolation was proposed at the interface between medium and air in [17], yet

the decoupling was led by the perturbation at the interface between medium and air, which introduces an air gap between medium and destroy the integrity of the medium. [18] proposed a method of dielectric loading and covering in rectangular waveguide phased arrays. It investigated the effect of dielectric geometry, constant, and sheath thickness on the wide scanning angle property of a rectangular waveguide phase array. In [18], the decoupling performance of the rectangular waveguide phase array was just simply studied and compared for the cases with different loaded dielectric parameters. However, the decoupling principle was not investigated in detail, especially the feasibility of decoupling for dual-polarization millimeter-wave arrays.

This paper firstly presents a decoupling concept of near-field shrinking dielectric superstrate (NFSDS) to reduce the coupling of large-scale, wideband, and dual-polarized mm-wave arrays, where the space wave coupling plays a decisive role. By employing the NFSDS, the space wave coupling of the mm-wave coupling could be significantly suppressed while the surface wave coupling slightly increases. But the total coupling of the array could have a decrement of 6.2 dB (from -17 dB to -23.2 dB) from 24 – 29.5 GHz and 7 dB (from -17 dB to -24dB) from 26.8 – 29.5 GHz. Compared to the currently existing literature, the novelty of the proposed decoupling method of NFSDS is summarized as follows:

1. The decoupling concept of near field shrinking is first proposed. The electromagnetic waves continuously propagate in NFSDS without perturbation, while the near field distribution is just shrunk to reduce the total coupling of the array.
2. Because the superstrate has a stable permittivity of 1.6 in a wide band, which is an intrinsic property of the superstrate itself. Hence, it can shrink the near field of the antenna itself without considering the coupling paths. Therefore, it can generally be applied in other massive MIMO array types.
3. The NFSDS is easy to integrate with mm-wave arrays, where the NFSDS has very simple structure and is mounted seamlessly above the mm-wave arrays. No air gap is introduced in actual applications to avoid fabrication errors.

This paper is organized as follows: Section II describes the decoupling principle in detail using a simple example of a dual-element array. The  $8 \times 8$  decoupled mm-wave array was designed by applying the proposed decoupling concept of NFSDS. Section III presents antenna performance, including S-parameters, radiation patterns, beam scanning capability, realized gain, and total efficiency. Section IV concludes the paper.

## II Proposed decoupling concept of NFSDS

### A. Decoupling scheme of the NFSDS

The sketch of the decoupling concept of NFSDS for mm-wave arrays is presented in Fig.1. The coupling of array is composed of surface wave coupling component  $x_1$  and space wave coupling component  $x_2$ , where the space wave coupling dominates with the inter-element distance close to half wavelength. It clearly demonstrates that the near fields of the array elements largely overlap with each other, which causes space wave coupling between array elements. When an NFSDS is seamlessly mounted above the array, the near-field electric field can be significantly shrunk, thereby reducing space wave coupling. The decrement of the space wave coupling is much larger than the increment of the surface wave coupling component  $x_1'$ . Consequently, the total coupling of the array is still reduced significantly.

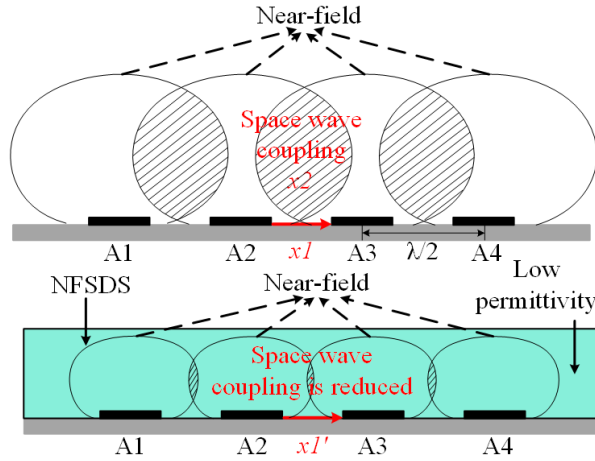


Fig. 1 The decoupling sketch of the NFSDS.

### B. Verification of the proposed decoupling concept

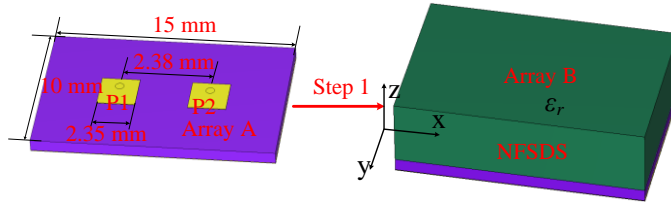


Fig. 2 The analysis for the verification of the proposed decoupling concept.

An analysis of the proposed decoupling concept is depicted in Fig. 2. A dual-element H-coupled patch antenna array working at 27 GHz is adopted as a reference, named Array A. The metal patches are printed on the top surface of the Rogers RO4350B substrate with a thickness of 1.52mm, a relative permittivity of 3.66 and a loss tangent of 0.0037. The center-to-center distance between array elements is around half-wavelength, and the patch size is 2.35 mm. Then, a pure superstrate with different permittivity and a thickness of 4 mm is mounted seamlessly above array A. The array with NFSDS is labeled as Array B.

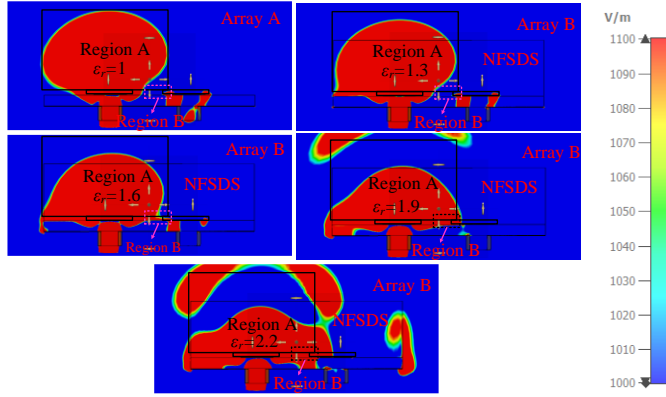


Fig.3 The E-field of the Array B with different  $\epsilon_r$  varying from 1.2 to 2.1 at a step of 0.3 at 27 GHz.

Intuitively, the permittivity and the thickness of the NFSDS affect the amount of reduction in space wave coupling and increment in surface wave coupling of the mm-wave arrays. To better understand the effect of the permittivity  $\epsilon_r$  and the thickness  $h_s$  of the NFSDS on the decoupling level, the parametric study of the permittivity  $\epsilon_r$  and the thickness  $h_s$  has been carried out. As the permittivity  $\epsilon_r$  varies from 1.3 to 2.2 at a step of 0.3, the E-fields of Array B at 27 GHz (mentioned in Fig. 2) are shown in Fig. 3, respectively. For the E-field distribution of Array A, the stronger electric field is tangential with a black rectangular line, which is an artificially marked E-field range. However, in the same area of Array B, the edge of the stronger E-field is far from the black rectangular line. It presents that the near field E-field in region A of Array B is smaller than that of Array A in the same area, demonstrating that the NFSDS can suppress the coupling of the array. The E-field distributions of Array B with different permittivity also show that when the permittivity  $\epsilon_r$  increases gradually, the near field E-field distribution in Region A shrinks correspondingly, yet the surface wave coupling in region B

increases. When a compromise value of the permittivity  $\epsilon_r$  is set as 1.6, the difference between the decrement in space wave coupling and the increment in surface coupling is the largest. Finally, the radiation distribution does not have obvious deformation.

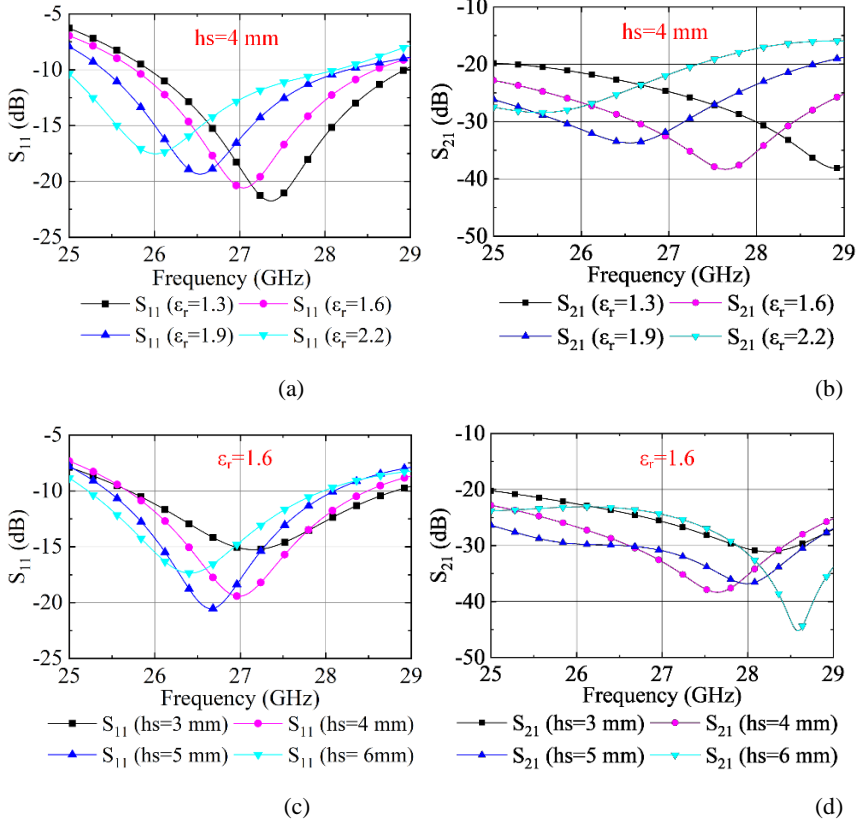


Fig.4 The S-parameters of the Array B with different  $\epsilon_r$  varying from 1.2 to 2.1 at a step of 0.3, and  $hs$  varying from 3 mm to 6 mm at a step of 1 mm: (a)  $S_{11}$  of the Array B with different  $\epsilon_r$  when  $hs$  is 4 mm, (b)  $S_{21}$  of the Array B with different  $\epsilon_r$  when  $hs$  is 4 mm, (c)  $S_{11}$  of the Array B with different  $hs$  when  $\epsilon_r$  is 1.6, (d)  $S_{21}$  of the Array B with different  $hs$  when  $\epsilon_r$  is 1.6.

The S-parameters of Array B with different permittivity  $\epsilon_r$  are presented in Fig. 4 (a) and Fig. 4 (b), which have the same step as that in the procedure of the parametric study for E-fields. Fig. 4 (a) shows that the operating band of Array B shifts to a lower band as the increment of  $\epsilon_r$ , which is caused by the change of the quality factor (Q value). Fig. 4 (b) demonstrates that as the permittivity  $\epsilon_r$  is 1.6, the coupling of the Array B reaches the lowest level and less than -38.3 dB within the working band. The parametric study results

provide direct evidence that as  $\epsilon_r$  is 1.6, A compromise between the reduction of space wave coupling and increment of surface wave coupling is taken. Thereby, the lowest total coupling of the Array B can be obtained. Fig. 4(c) and Fig. 4(d) give the S11 and S21 of the Array B with different thicknesses of  $h_s$  that vary from 3 mm to 6 at a step of 1mm, respectively. Fig. 4 (c) depicts that the working band of array B shifts to a lower band when  $h_s$  increases, which also results from the quality factor (Q value) change. In addition, when the thickness  $h_s$  is set as 4 mm (around half wavelength in the dielectric substrate), the coupling of the Array B is lower than 38.3 dB. Though the coupling of Array B with a thickness of 5mm is lower than that with a thickness of 4mm, its working band shifts toward a lower band than the required band. In the end, the permittivity and thickness of the NFSDS are optimized and set as 1.6 and 4 mm, respectively. Though the thickness of the NFSDS is relatively large, it is acceptable in mm-wave band application.

### III Example of $8 \times 8$ mm-wave array with NFSDS

#### A. Decoupling scheme of the NFSDS

An  $8 \times 8$  mm-wave array with NFSDS is designed to verify the decoupling concept of NFSDS for large-scale, wideband, and dual-polarized mm-wave arrays. Fig. 5 presents the explosion structure and dimensions of the  $8 \times 8$  mm-wave array element with NFSDS. The proposed array consists of dual layers of circle patches to generate two closed resonant frequencies to broaden the antenna working band. The array elements are fed by the differential feed structure. In the end, a dual-polarized array element with high port-to-port isolation can be obtained. Here, the inverting power divider of the differential feed structure has two arms (arm1 and arm2) with a length difference of half-wavelength at the center frequency to generate differential signals. In addition, practical base stations require a beam scanning capability more than  $50^\circ$  in x-direction, and a relatively small beam scanning capability more than  $30^\circ$ . Therefore, the array element distance in x-direction and y-direction are set as 5.2 mm ( $0.448\lambda_0$ ) and 6.8 mm ( $0.612\lambda_0$ ), respectively.

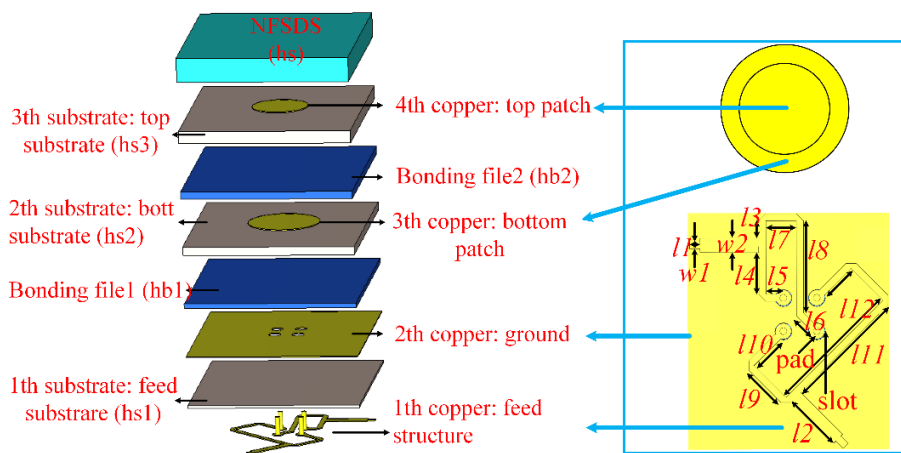
The detailed explosion diagram of the  $8 \times 8$  mm-wave array element with NFSDS and the dimensions of the differential feed structures are depicted in Fig. 5 (a). The NFSDS is made of pure polypropylene (PP) with a dielectric constant of 2.2. Periodic air holes with a radius of  $rc$ , and a period of  $tp$  are drilled on it to get a lower effective permittivity. The thickness of the substrates, bonding files, and NFSDS are also given in Fig. 5 (a). The four

metal probes pass through the circle slot on the ground and connect the differential feed structures with the bottom patch. The pad of the metal probes and the circle slot on the ground have a radius of  $r_p$  and  $r_s$ , respectively. TABLE I gives the dimensions mentioned above. The specific geometry of the array without NFSDS is shown in Fig. 5 (b) from top and bottom view. The four fixing arms are connected to the corners of the substrate for installation. Here, the metal vias are drilled on the fixing arms to avoid the effect of fixing arms on antenna performance. Fig. 5 (c) shows the arrangement of the mm-wave array and the feeding ports in  $-45^\circ$  polarization. Fig. 5 (d) gives the fabricated prototype of the array with NFSDS, where the NFSDS and the original array are seamlessly pressed together by four screws. The MMPX connectors feed the array. The common ground, bottom and top circle patches are printed on the Rogers RO4350B substrate, which are attached together by the bonding files to avoid air gaps. The bonding films used here are Rogers 4450F with a dielectric constant of 3.52 and a loss tangent of 0.004. Finally, the NFSDS covers the original array to shrink the near fields of the array elements. Even though the NFSDS and original array are not stucked together, there are no air gap between NFSDS and original array because pp board and Ro4350 are not easily deformed when they are screwed together. Additionally, the sizes of pp board and Ro4350 are very small, when the four corners of pp board and Ro4350 are pressured, their shape is basically kept unchanged. From Fig.5 (d), we can know that due to the space limitation, only a row of MMPXs is connected to the array to activate the array elements in one polarization. Then, the array elements of the other rows are connected to the MMPX connector in turn so that the test can be smoothly implemented.

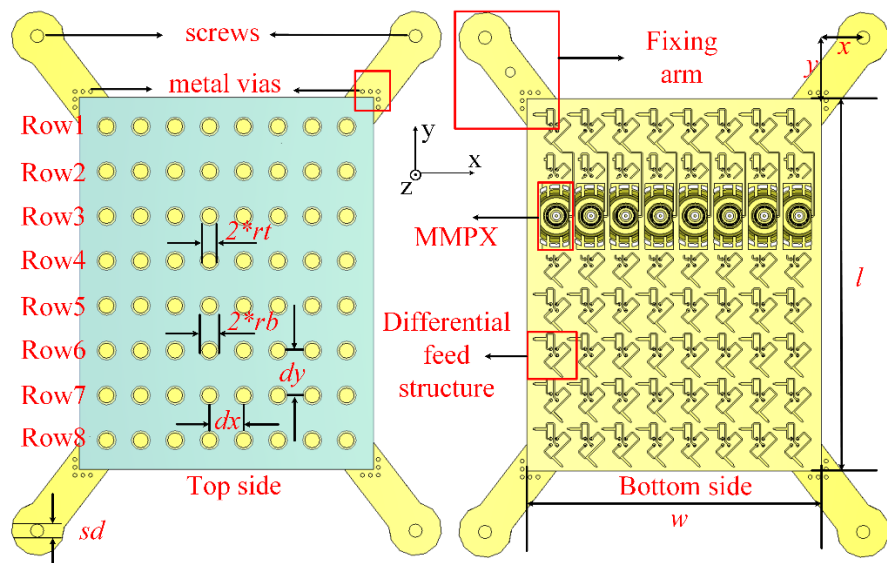
Here, two reasons cause the size of NFSDS to be larger than the size of the antenna:

1. The fixing arm is located outside the antenna array, and the hole, the screw passes through, is far away from the antenna array. Therefore, NFSDS should cover the fixing hole to facilitate installation and fixing.
2. To enable the NFSDS to cover the near field of the edge elements of the antenna array, the size of the NFSDS should also be larger than the size of the antenna array.

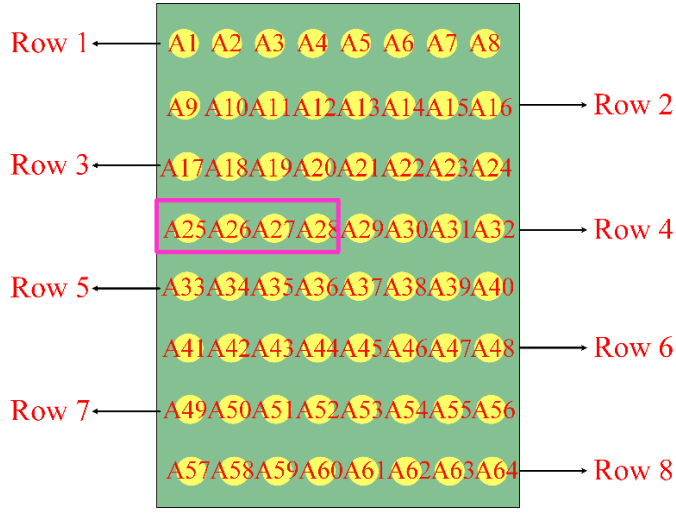




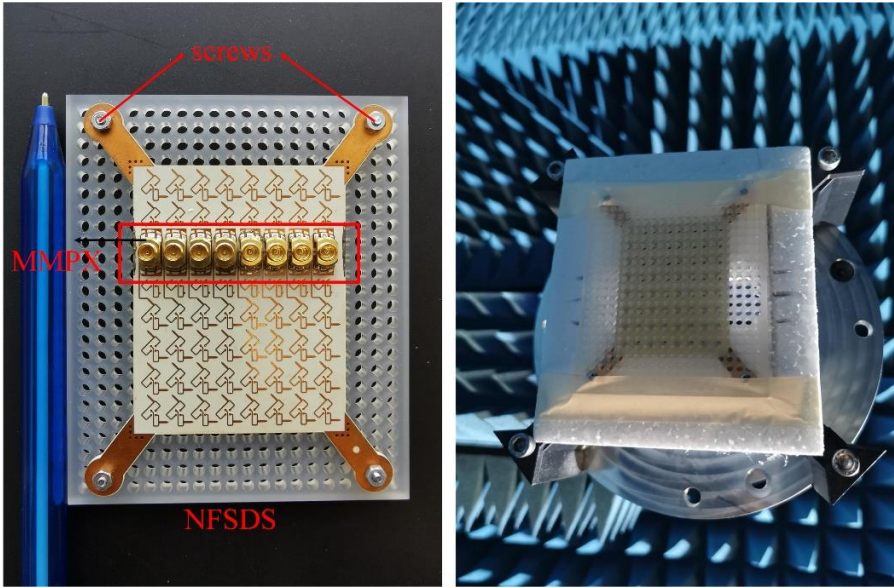
(a)



(b)



(c)



(d)

Fig.5 Configuration of the example: (a) the explosion structure of the  $8 \times 8$  mm-wave array element with NFSDS and the detailed structure and dimensions of the array element, (b) the specific geometry of the array without NFSDS from the top and bottom views, (c) the arrangement of the mm-wave array and the feeding ports in  $-45^\circ$  polarization, (d) the fabricated prototype of the Array with NFSDS.

TABLE I

PARAMETERS OF THE ARRAY WITH NFSDS

parameters	<i>dx</i>	<i>dy</i>	<i>hs</i>	<i>hs1</i>	<i>hs2</i>	<i>hs3</i>	<i>hb1</i>
value(mm)	5.2	6.8	4	0.101	0.338	0.508	0.202
parameters	<i>hb2</i>	<i>l</i>	<i>l1</i>	<i>l2</i>	<i>l3</i>	<i>l4</i>	<i>l5</i>
value(mm)	0.303	56.4	0.3	1.7	0.5	1.22	0.5
parameters	<i>l6</i>	<i>l7</i>	<i>l8</i>	<i>l9</i>	<i>l10</i>	<i>l11</i>	<i>l12</i>
value(mm)	0.72	0.88	2.74	1.3	1.1	3.55	3.96
parameters	<i>rb</i>	<i>rc</i>	<i>rp</i>	<i>rs</i>	<i>rt</i>	<i>sd</i>	<i>tp</i>
value(mm)	1.46	1.1	0.2	0.25	1.14	2	3
parameters	<i>w</i>	<i>w1</i>	<i>w2</i>	<i>x</i>	<i>y</i>		
value(mm)	43.6	0.2	0.4	6.8	9.2		

## B. Antenna array performance

The S-parameters of the  $8 \times 8$  mm-wave arrays before and after decoupling are simulated, and measured. The reflection coefficient and the envelopes of the couplings of the array elements are depicted in Fig. 6, where the envelope of the coupling is extracted from the maximum values of all the coupling paths varying different frequencies. Notably, the coupling paths of this array includes coupling in x-direction, y-direction, diagonal direction between neighbor, non-neighbor array elements, and cross polarization ports of array element itself. The elements in the left part of the inner loop are selected because of the symmetry along the y-axis, including Row 4 (A25, A26, A27, A28). It demonstrates that the mm-wave array with NFSDS has a -23.2 dB and -24 dB decoupling bandwidth of 24 – 29.5 GHz and 26.8 – 29.5 GHz, respectively. The simulations and measurements illustrate that the NFSDS can effectively reduce the total coupling of the mm-wave arrays.

The radiation patterns of the array element A27 at 25 GHz, 27 GHz, and 29 GHz are presented in Fig. 7. The measurement for the radiation patterns is implemented in a chamber. It illustrates that the contour of the radiation patterns of the mm-wave arrays before and after decoupling are unchanged within around  $-60^\circ$  to  $60^\circ$  besides some sharp distortions, so it largely does not affect the antenna performance in the effective radiation direction.

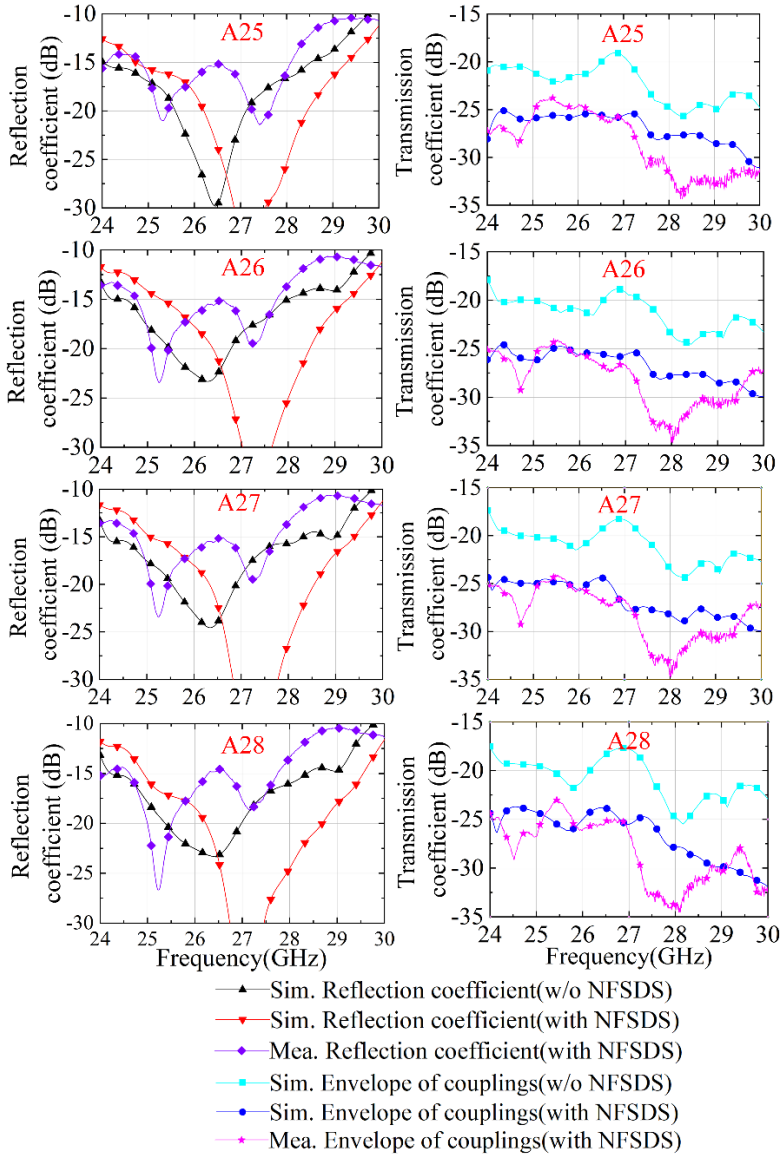


Fig.6 The reflection coefficient and transmission coefficient of the mm-waves array with and without NFSDS.

Fig. 8 presents the realized gain and total efficiency of the selected element A27 at different frequencies. Here, the proposed decoupling method is applied for massive MIMO arrays, therefore the total efficiency of the array element is given rather than the total efficiency of the array. Since the total coupling has a significant reduction, it means the electromagnetic wave radiated to

other elements in the horizontal direction is reduced. Thus, the power radiated to the space is promoted. Consequently, the realized gain and total efficiency of the array elements are effectively improved by loading the NFSDS above the original array. Notably, according to the radiation patterns in Fig. 7, though the counter of the radiation patterns of the array with and without are basically same, some sharp distortion occurred after loading the NFSDS, which contributes to realized gain improvement. Here, the pink point of the realized gain appears at the sharp distortion. As a result, even though the counter of the radiation patterns before and after loading NFSDS are keep same, the peak realized gain has an increment by loading NFSDS. The results in Fig. 8 conform to the theoretical analysis from Fig. 8.

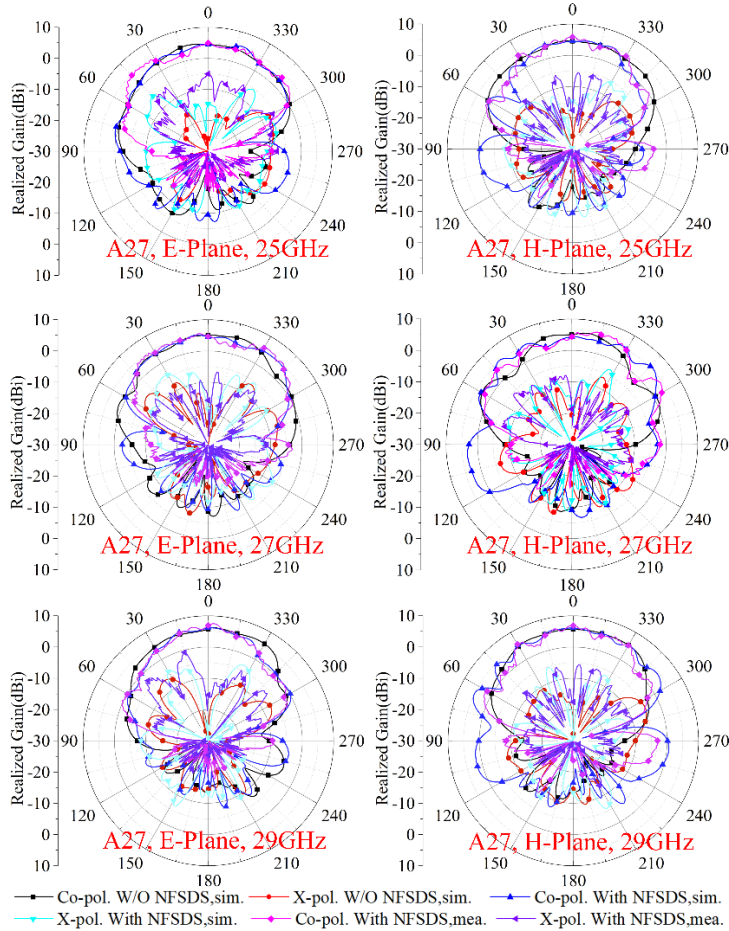


Fig.7 The radiation patterns of the mm-waves array element A27 before and after deploying NFSDS at 25GHz, 27GHz, and 29GHz.

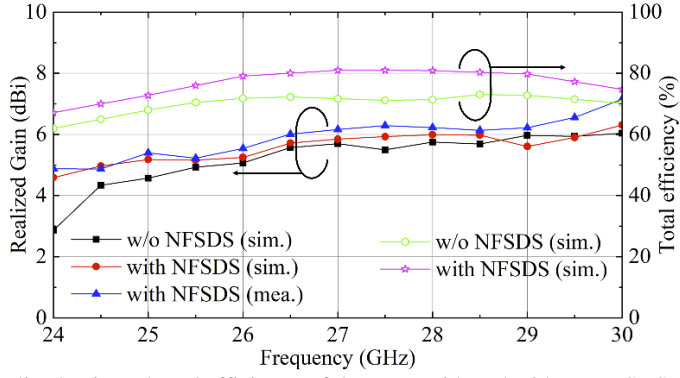
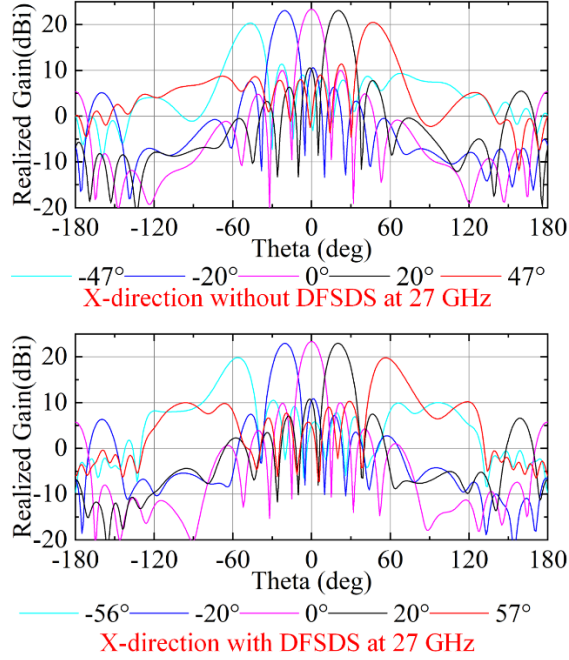


Fig.8 The realized gain and total efficiency of the array with and without NFSDS.

### C. Beam scanning capability



(a)

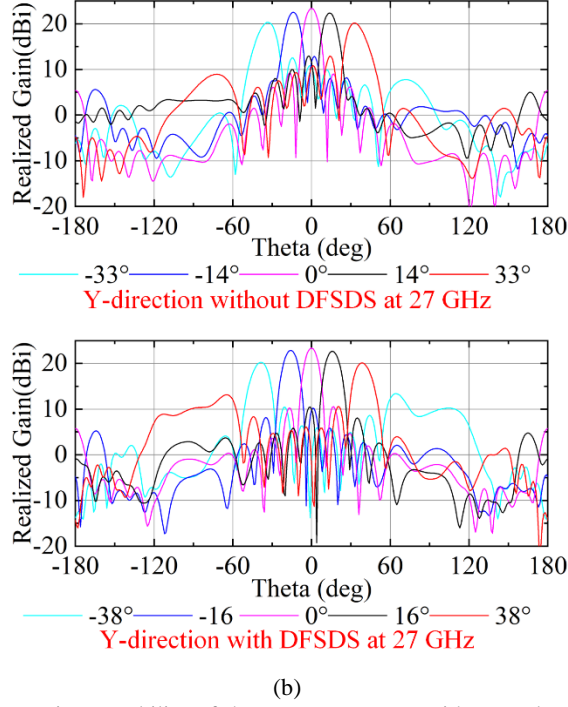


Fig.9 The beam scanning capability of the mm-wave array without and with NFSDS, (a) x-direction, (b) y-direction.

The beam scanning capability is an important metric for large-scale phased arrays. Fig. 9 presents the simulated beam scanning of the mm-wave array with and without NFSDS in x-polarization and y-polarization, respectively. It can be found that the 3dB gain drop beam scanning capability of the original array in the x-direction and y-direction is  $-47^{\circ}$ – $47^{\circ}$  and  $-33^{\circ}$ – $33^{\circ}$ , respectively, while the decoupled array has a 3dB gain drop beam scanning capability of  $-56^{\circ}$ – $57^{\circ}$  and  $-38^{\circ}$ – $38^{\circ}$  in x-direction and y-direction, respectively. It concludes that the NFSDS can facilitate the beam scanning capability of the array. For the base stations, the beam scanning capability in y-direction is normally required no less than  $\pm 30^{\circ}$ , while it requires a stronger beam scanning capability in x-direction than that in y-direction. Therefore, the proposed array in this paper can fully satisfy the industry requirement of the base station design.

#### D. Antenna Performance Comparison

TABLE II

PERFORMANCE COMPARISON OF THE PROPOSED ANTENNA ARRAY WITH OTHER STATE-OF-THE-ART SIMILAR WORK.

Ref.	Decoupling method	Pol. & Scale	Freq. (GHz) and Imp. BW (%)	23 dB Iso. BW (%)	Antennas Distance	Beam scanning (3dB gain drop)	Feasib. for mm-wave massive MIMO arrays
[13]	Decoupling network	Dua.-pol. $4 \times 4$	4.8-5 (4.08%)	2.04%	$0.50\lambda_0$	--	no
[14]	ADS	Dua.-pol. $4 \times 4$	3.2-3.9 (19.72%)	14.29%	$0.65\lambda_0$	--	no
[15]	TMS	Dua.-pol. $4 \times 4$	4.21-4.82 (13.51%)	13.5%	$0.5\lambda_0$	--	no
[16]	Orth. feed network	Dua.-pol. $2 \times 2$	24-40 (50%)	--	--	--	yes
[17]	DDS	Dua.-pol. $4 \times 4$	4.25-5.25 (20%)	10.5%	$0.485\lambda_0 \times$ $0.485 \lambda_0$	--	yes
<b>This work</b>	<b>NFSDS</b>	<b>Dua.-pol.</b> <b><math>8 \times 8</math></b>	<b>24-29.5</b> <b>(20.37%)</b>	<b>20.37%</b>	<b><math>0.448\lambda_0 \times</math></b> <b><math>0.612 \lambda_0</math></b>	$-56^\circ - 57^\circ$ (x) $-38^\circ - 38^\circ$ (y)	<b>yes</b>

Ref.: Reference    Pol.: polarized    Dua.: Dual    Freq.: Frequency    Iso.: Isolation  
Feasib.: Feasibility    imp.: impedance    orth.: orthogonal

The performance of the proposed array with NFSDS is compared with the structures in the current literature. The comparison is listed in TABLE II. The methods of decoupling network and Array decoupling surface (ADS) [13] [14] are two effective decoupling approaches for massive MIMO arrays. However, it cannot be applied to mm-wave antennas. The TMS in [15] divides the space wave coupling into two parts with different propagation paths with the same amplitudes and opposite phases to enable cancellation with each other. Yet, owing to the decoupling performance of mm-wave arrays being sensitive to the distance between the array and metasurface, it is difficult to be used in



mm-waves applications. In addition, the working band of the arrays in [13], [14], and [15] is narrower than the one in our work. The decoupling method in [16] can be used in mm-wave antennas. Although the antenna in [16] has a wider bandwidth than that in our work, its isolation improvement is caused by the orthogonal feed mode, and the best isolation reaches 17.6 dB, which is far lower than 23 dB. The orthogonal feed structure has an apparent superiority for isolation enhancement, yet it cannot be scaled to the massive MIMO arrays. Though the height of this work is around half wavelength, the real thickness of the NFSDS is just 4 mm. In addition, the low permittivity substrate is obtained by simply drilling the periodic air cavities on the pure PP board, and loading above the array without an air gap. Therefore, the proposed array with NFSDS performs a low design and fabrication complexity that almost does not introduce fabrication tolerance. The array in [17] can also be applied in massive MIMO mm-wave arrays, but it has a narrower 23 dB isolation bandwidth than that of our work. For the fabrication of the work in [17], it adopts 3D printing technology, but it might introduce air to the printing material so that leads to fabrication tolerance. Especially for the mm-wave array, the antenna performance and the decoupling are highly sensitive to the stability of the adopted material. It is worth noting that the proposed decoupled array has an excellent beam scanning capacity than other antennas in current literature. In summary, the method proposed in this letter is a promising candidate for mm-wave application.

## IV Conclusion

A novel decoupling concept of NFSDS for wideband and dual-polarized large-scale antenna arrays is proposed. By comparing the E-field distributions of the array covered by the pure substrate with different permittivity, the decoupling principle is analyzed carefully. The optimized permittivity is 1.6 and the thickness of the NFSDS is 4 mm and then a significant space wave coupling is suppressed. Based on the theoretical analysis, a real example of an  $8 \times 8$  array with NFSDS is simulated, fabricated, and measured correspondingly. The measurements keep consistent with the simulated results. The array with NFSDS has a 23.2 dB and 24 dB decoupling bandwidth of 24 – 29.5 GHz and 26.8 – 29.5GHz, respectively. Meanwhile, the array has an excellent beam scanning capability of  $-56^\circ$ – $57^\circ$  in the x-direction and  $-38^\circ$ – $38^\circ$  in the y-direction, respectively which makes the decoupling method of NFSDS a promising solution for the isolation improvement of the dual-polarization and wideband mm-wave arrays in 5G and beyond application.

## Reference

- [1] Y. Wu, Z. Hao, and Z. Miao, "A planar w-band large-scale high-gain substrate-integrated waveguide slot array," *IEEE Trans. Antennas Prop.*, vol. 68, no. 8, pp. 6429-6434, Aug. 2020.
- [2] C. Liang, Y. Lyu, D. Chen, and C. Cheng, "Wideband circularly polarized stacked patch antenna based on TM11 and TM10," *IEEE Trans. Antennas Propag.*, vol. 70, no. 4, pp.2459-2467, Apr. 2022.
- [3] B. K. Lau, J. B. Andersen, G. Kristensson, and A. F. Molisch, "Impact of matching network on bandwidth of compact antenna arrays," *IEEE Trans. Antennas Propag.*, vol. 54, no. 11, pp.3225-3238, Nov. 2006.
- [4] D. M. Pozar, "A relation between the active input impedance and the active element pattern of a phased array," *IEEE Trans. Antennas Propag.*, vol.51, no. 9, pp. 2486-2489, Sep. 2003.
- [5] Z. Ying and D. Zhang, "Study of the mutual coupling, correlations and efficiency of two PIFA antennas on a small ground plane," *IEEE Antennas Propag. Soc. Int. Symp.*, Washington, DC, Jul. 2005, pp. 305-308.
- [6] R. Janaswamy, "Effect of element mutual coupling on the capacity of fixed length linear arrays," *IEEE Antennas Wireless Propag. Lett.*, vol. 1, pp. 157-160, 2002.
- [7] K. H. Chen and J. F. Kiang, "Effect of mutual coupling on the channel capacity of MIMO systems," *IEEE Trans. Veh. Technol.*, vol. 65, no. 1, pp. 398-403, Jan. 2016. (13)
- [8] A. R. Vilenskiy, V. I. Litun, and K. V. Lyulyukin, "Wideband beam steering antenna array of printed cavity-backed elements with integrated EBG structure," *IEEE Antennas Wireless Propag. Lett.*, vol. 18, no. 2, pp. 245-249, 2019.
- [9] D. Gao, Z. Cao, S. Fu, X. Quan, and P. Chen, "A novel slot-Array Befected ground structure for decoupling microstrip antenna array," *IEEE Trans. Antennas Propag.*, vol.68, no. 10, pp. 7027-7038, Oct. 2020.
- [10] M. Li, X. Chen, A. Zhang, Wei Fan, and A. A. Kishk, "Split-ring resonator-loaded baffles for decoupling of dual-polarized base station array," *IEEE Antennas Wireless Propag. Lett.*, vol. 19, no. 10, pp.

1828-1832, 2019.

- [11] R. liu, x. an, h. zheng, m. wang, z. gao, and e. li, "neutralization line decoupling tri-band multiple-input multiple-output antenna design," *IEEE Access*, vol. 8, pp. 27018–27026, 2020.
- [12] Min Li, and S. Cheung, "A Novel calculation-based parasitic decoupling technique for increasing isolation in multiple-element MIMO antenna arrays," *IEEE Trans. Veh. Technol.*, vol. 70, no. 1, pp. 6242–6253, Jan. 2021.
- [13] Y. Zhang, Q. Ye, G. F. Pedersen, S. Zhang, "A Simple decoupling network with filtering response for patch antenna arrays" *IEEE Trans. Antennas Propag.*, vol.69, no. 11, pp. 7427-7439, Nov. 2021.
- [14] C. Wei, Z. Zhang, and K. Wu, "Phase compensation for decoupling of large-scale staggered dual-polarized dipole array antennas," *IEEE Trans. Antennas Propag.*, vol. 68, no. 4, pp. 2822–2831, Apr. 2020.
- [15] S. Luo, Y. Zhang, G. F. Pedesen, and S. Zhang, "Mutual decoupling for massive mimo antenna arrays by using triple-layer meta-surface," *IEEE Trans. Open Journal of Antennas and Propag.*, Published. 2022.
- [16] X. Dai and K. Luk "A wideband dual-polarized antenna for millimeter-wave applications," *IEEE Trans. Antennas Propag.*, vol. 69, no. 4, pp. 2380-2385, Apr. 2021.
- [17] P. Mei, Y. Zhang, S. Zhang, "Decoupling of a wideband dual-polarized large-scale antenna array with dielectric stubs," *IEEE Trans. Veh. Technol.*, vol. 67, no. 4, pp. 2828–2863, Apr. 2018.
- [18] V. Galindo and C. P. Wu, "Dielectric loaded and covered rectangular waveguide phased arrays," in *The Bell System Technical Journal*, vol. 47, no. 1, pp. 93-116, Jan. 1968.

ISSN (online): 2446-1628  
ISBN (online): 978-87-7573-638-6

AALBORG UNIVERSITY PRESS